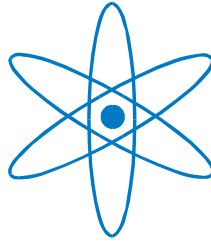


PHYSIK-DEPARTMENT



“Studien zu Topquark-Paarproduktion in
Proton-Proton Kollisionen am Large Hadron
Collider mit dem ATLAS Experiment”

Dissertation
von

Sophio Pataraiia



TECHNISCHE UNIVERSITÄT
MÜNCHEN

TECHNISCHE UNIVERSITÄT MÜNCHEN

MAX-PLANCK-INSTITUT FÜR PHYSIK

Studies on top quark pair production in pp collisions at
the Large Hadron Collider with the ATLAS experiment

SOPHIO PATARAIA

Vollständiger Abdruck der von der Fakultät für Physik der
Technischen Universität München zur Erlangung des
akademischen Grades eines Doktors der Naturwissenschaften
genehmigten Dissertation.

Vorsitzender:

Univ. – Prof. Dr. A. J. Buras

Prüfer der Dissertation:

1. Hon. – Prof. Dr. S. Bethke
2. Univ. – Prof. Dr. St. Paul

Die Dissertation wurde am 09.11.2009 bei der Technischen
Universität München eingereicht und durch die Fakultät für
Physik am 15.12.2009 angenommen.

Abstract

We studied the performance of the track based alignment software of the ATLAS Inner Detector. To improve the final alignment additional vertex and beam constraints on the track reconstruction were investigated.

We also investigated the b-tagging performance at an early stage of the detector operation. The dependence of the performance on the jet reconstruction algorithm, and on the Inner Detector misalignment were studied.

A Top quark pair-production cross section measurement with and without b-tagging using the simulated ATLAS data corresponding to the luminosity of 200pb^{-1} was carried out. We applied a simple and robust cut and count method suitable for the early phase of the detector operation. We investigated the systematic uncertainties on the cross section measurements due to Monte Carlo modeling of the precesses, for various scenarios of the alignment of the inner detector, for several jet reconstruction algorithms and for variations of the absolute jet energy scale. It yields an early cross-section measurement with a systematic error of less than 30%.

Zusammenfassung

Wir haben das Verhalten der spurbasierten Alignmentsoftware für den inneren Detektor von ATLAS mit simulierten Daten studiert. Der Alignmentalgorithmus wurde durch Auswerten der Position der LHC Strahlen und der Ereignisvertizes verbessert. Das Verhalten der Algorithmen für Identifikation von B-Hadronen in Jets (b-tagging) wurde mit simulierten Daten für die Erwartung erster Daten untersucht. Dabei wurden vor allem die Jetrekonstruktion und das Alignment des inneren Detektors variiert. Nach Alignment mit den ersten Daten wird erwartet, dass b-tagging eingesetzt werden kann. Eine Messung des Produktionswirkungsquerschnitts für Produktion von top-antitop Quarkpaaren wurde für 200pb⁻¹ simulierter Daten durchgeführt. Dabei wurden Ereignisse nach verschiedenen Selektionen mit und ohne b-tagging gezählt und mit simulierten Daten der Anteil von Signal- und Untergrundereignissen abgeschätzt. Als wesentliche systematische Unsicherheiten wurden Monte Carlo Modelle, Alignmentsszenarios, Jetalgorithmen und die Energieskala des Kalorimeters variiert. Im Ergebnis wird ein systematischer Fehler von weniger als 30% für die Messungen mit und ohne b-tagging gefunden.

Contents

1	Introduction	1
1.1	Standard Model	3
1.1.1	The Electroweak Model	6
1.1.2	Quantum chromodynamics (QCD)	10
1.1.3	Feynman rules of QCD	12
1.1.4	Hadron collider phenomenology	14
1.1.5	Top quark physics	17
1.2	Physics beyond the Standard Model	21
1.3	The Large Hadron Collider (LHC)	24
1.4	Physics at the LHC	28
1.5	The ATLAS detector	31
1.5.1	Inner Detector	34
1.5.2	Calorimetry	36
1.5.3	Muon system	38
1.5.4	Trigger and Data Acquisition System	39
2	Track based alignment of the Inner Detector	43
2.1	Data sets	45
2.1.1	Multimuon samples	45
2.1.2	The Computing System Commissioning (CSC) Data challenge	46
2.2	Track Reconstruction	47
2.2.1	Error scaling	47
2.3	Vertex Reconstruction	49
2.3.1	Vertex fitting	49

2.3.2	Refit of tracks with vertex	50
2.3.3	Performance Studies	50
2.4	Alignment of the ATLAS Inner Detector	51
2.4.1	Including the vertex information in the local χ^2 alignment	56
2.4.2	Alignment with the CSC data	57
2.4.3	Alignment with reconstructed vertex distributions	60
2.4.4	Track parameters before and after vertex refit	65
2.5	Conclusions	70
3	Heavy flavor tagging with ATLAS	71
3.1	Jet reconstruction algorithms	72
3.1.1	Heavy flavor tagging algorithms	74
3.2	Calibration of the tagging procedure	79
3.3	Performance studies	79
3.4	Data samples and detector geometry	80
3.4.1	Performance with various inner detector misalignment scenarios	80
3.4.2	Performance with different jet reconstruction algorithms	86
3.4.3	Track to jet association studies	90
3.4.4	Performance of different b-tagging calibration scenarios	96
3.5	Summary of systematic performance studies	96
4	Top-Antitop cross section measurement with early data	99
4.1	Theoretical cross section and simulated data sets	100
4.2	Reconstruction	103
4.2.1	Trigger	107
4.2.2	Electron reconstruction	108
4.2.3	Muon reconstruction	108
4.2.4	Jet and missing energy reconstruction	109
4.3	Cut and count method	109
4.4	Event selection	110
4.4.1	Pre-Selection(DPD)	110
4.4.2	Final Selection	111
4.4.3	Selection efficiencies with and without heavy flavour tagging	115

4.4.4	Selection efficiencies for the ACERMC and MC@NLO samples	115
4.4.5	Selection efficiencies for various misalignment scenarios	116
4.4.6	Selection efficiencies for various jet algorithms	120
4.4.7	Selection efficiencies for various jet energy scales	121
4.4.8	Initial and Final State Radiation systematics	122
4.4.9	PDF uncertainties	124
4.4.10	Estimation of the background fraction	125
4.5	Systematic Uncertainties on the cross section measurement	131
4.6	Conclusion	132
5	Conclusions	135
	Bibliography	139

Chapter 1

Introduction

The Standard Model (SM) is a successful framework of the fundamental particles and their interactions [1]. The SM provides powerful predictions and is consistent with experimental measurements. The SM will be challenged vigorously by the next generation of hadron collider experiments located at CERN in Geneva, Switzerland.

The Large Hadron Collider (LHC) is a proton-proton collider built at CERN. The LHC is a 27 km ring which contains 1232 superconducting dipole magnets and will accelerate protons to energies of 7 TeV. It started operation in autumn of 2008 with machine commissioning of about 10 days until a major accident occurred. Subsequently it was switched off until repair of the damage and safety commissioning is finished for the complete accelerating system.

ATLAS (A Toroidal LHC ApparatuS), and CMS (Compact Muon Spectrometer) are general-purpose detectors placed on the collision region in the LHC ring [2], [3]. The experiment is currently in the commissioning and calibration phase. Beginning in Autumn 2008 cosmic data taking has been performed for detector commission-

ing, calibration and alignment purposes. Many detailed simulations have been produced to study the performance of the detector, and to establish and cross-check the performance of the analysis procedures used for a wide range of physics processes of interest. This thesis describes contributions to the inner detector alignment and studies of the performance of the physics analyses with regard to the imperfections of the inner detector alignment and/or heavy flavour tagging procedure.

The ATLAS experiment is a complex system consisting of several particle detectors: silicon and straw tube detectors placed inside a strong solenoid field are used for charged particle track reconstruction. Various calorimeters are used to measure energy deposits of the particles, and drift tube and resistive plate chambers placed in a strong toroid field are used for the muon spectrometer.

The construction of the detector was finished in summer 2008. One of the next steps towards the ultimate physics performance of the detector is to determine the position of the detector elements, known as the alignment of the detector. ATLAS tracking requires that the position of the silicon detector elements is known to a precision better than about 10 micrometers (μm). This precision can only be achieved by track based alignment algorithms. A detailed analysis including the implementation of the alignment software tool in the computing model of the ATLAS experiment, as well as tests of the misaligned detector setups using simulated data will be presented in chapter 2.

The top quark was discovered at the Fermilab Tevatron accelerator (1995) [4], [5]. The properties of the top quark are less well known than those of the other quarks [6]. The LHC colliding protons at a center-of-mass (CMS) energy of $\sqrt{s} = 14$ TeV will produce

about 8 million top antitop ($t\bar{t}$) quark events per year at a luminosity of $10^{33} \text{ cm}^{-2} \text{ s}^{-1}$ and therefore is frequently referred to as a "top factory". ATLAS aims to take advantage of the high statistics in order to perform precise measurements of the top quark sector.

Top quarks decay into a W boson plus a b quark, and therefore identification of jets which originate from a b quark (b-jet tagging) is important for the signal reconstruction, and for the separation of signal from background. The performance of b-tagging procedures is studied, and contributions to the uncertainties to the $t\bar{t}$ production cross section measurements are estimated.

An overview of the Standard Model of particle physics, as well as top quark physics, a brief description of the ATLAS detector and in particular the tracking detectors are part of Chapter 1. Chapter 2 describes studies of the track based alignment procedure for the inner detector. The heavy flavour tagging procedure and performance studies are described in Chapter 3. Estimation of the b-jet tagging uncertainties contributing to the $t\bar{t}$ production cross section measurement is discussed in Chapter 4. Finally conclusions and outlook towards precise measurements of the $t\bar{t}$ production cross section with the ATLAS experiment are discussed in Chapter 5.

1.1 Standard Model

The formation of the Standard Model was a great achievement of the 20th century. At all energies and precisions so far reached in experiments the Standard Model has held up [1]. The Standard Model is a Quantum Field Theory (QFT) combining quantum mechanics and special relativity and it uses perturbation theory to calculate measurable quantities [7]. In order to make predicted physics quan-

tities finite to all orders of perturbation theory the theory has to be renormalized [8].

Until the 1970's the only successful renormalizable quantum field theory was Quantum electrodynamics (QED) - the quantum field theory describing the electromagnetic interactions, which is an example of a gauge theory [7]. A gauge theory is a field theory which is invariant under a set of local transformations, the transformations described by parameters which can vary in space-time. For each generator of a local transformation there is a massless vector boson ("gauge boson") in the theory in order to preserve invariance under this transformation. In the case of QED, with only one phase transformation (group $U_Y(1)$) acting on the fields of the charged particles there is only one massless vector particle known as the photon.

In the 1960's natural extensions of the ideas of gauge field theory as a renormalizable quantum field theory were explored to describe weak interactions, in which particles undergo isospin transformations under the group $SU_L(2)$. Gauge invariance requires massless gauge bosons, and therefore massless intermediate vector bosons for the interaction, which is true for QED. However, this is unsuitable for the weak interaction, as short range interactions require massive exchange particles. One way to solve this problem introduced by Glashow, Weinberg, and Salam was "spontaneous symmetry breaking". In this scenario the masses of the gauge bosons and the masses of the elementary particles are generated without breaking gauge invariance [9, 10, 11]. This model predicted masses of intermediate vector bosons (W^\pm and Z^0), which were successfully verified by the UA1 and UA2 collaborations at Sp \bar{p} S (CERN Geneva) with W^\pm ([12], [13]) and Z^0 ([14], [15]) discovery in 1983. For spontaneous symmetry breaking the model requires the existence of a massive

scalar particle, the Higgs boson [16], [17].

The Higgs boson has not yet been observed experimentally. A lower bound of $114.4 \text{ GeV}/c^2$ for the Higgs boson mass is provided by the LEP experiments [18]. Further theoretical and experimental constraints are derived from fits of precision SM measurements. Figure 1.1 shows current fits derived from the Z-pole measurements from SLD and LEP, the LEP-2 results on the mass and width of the W boson and Tevatron measurements on the Top quark and W boson mass and width [19].

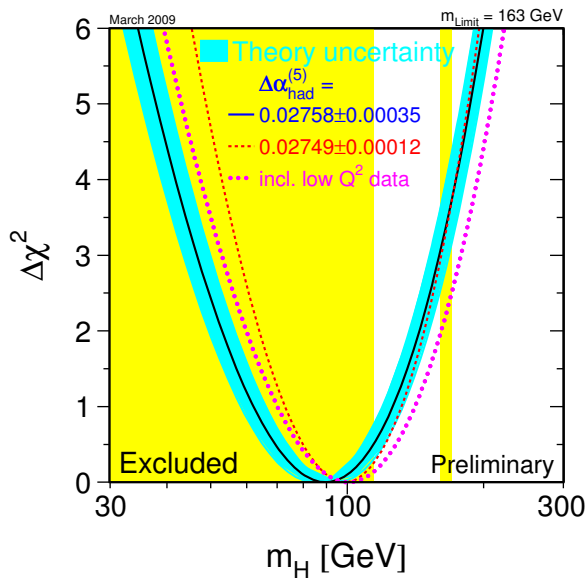


Figure 1.1: The $\Delta\chi^2$ curve derived from high- Q^2 precision electroweak measurements, performed at LEP and by SLD, CDF, and D0, as a function of the Higgs-boson mass.

Quantum Chromodynamics (QCD) was developed in the 1970's by Fritzsch, Gell-Mann, Leutwyler and by Gross and Wilczek and later by Politzer [20], [21]. QCD is a gauge theory which describes

the strong interactions between quarks and gluons. QCD is invariant under colour transformations under the $SU_C(3)$ group, with eight gauge bosons identified as the gluons.

The current Standard Model successfully combines two gauge theories: the Glashow-Weinberg-Salam model (GWS) for electroweak theory and QCD. The Standard Model gauge group is the product group $SU_c(3) \times SU_L(2) \times U_Y(1)$, with the component groups associated with the color (c), weak (charged weak interaction involves coupling only with chiral-left (L) component of the fermions) and hypercharge (Y) symmetries. The Standard Model Lagrangian may be written as follows:

$$\mathcal{L}_{SM} = \mathcal{L}_{GAUGE} + \mathcal{L}_{MATTER} + \mathcal{L}_{YUKAWA} + \mathcal{L}_{Higgs} \quad (1.1)$$

The first component \mathcal{L}_{GAUGE} accounts for the kinetic energy of the gauge fields and their self interactions. The second term \mathcal{L}_{MATTER} represents the kinetic energy of fermions and their interactions with the gauge fields. The third term \mathcal{L}_{YUKAWA} corresponds to the interactions between the Higgs field with the fermions and gives masses to the fermions. The final term \mathcal{L}_{Higgs} combines the kinetic energy of the Higgs field, its gauge interactions, and the Higgs potential.

In table 1.1 the fundamental particles in the SM and some of their properties are shown. There are three lepton and quark generations, every particle has its anti-particle, and quarks come with three different colors.

1.1.1 The Electroweak Model

The electroweak model describes both the weak and electromagnetic interactions. It is a gauge theory based on the $SU_L(2) \times U_Y(1)$ sym-

Fermions (spin=1/2)					
Leptons			Quarks		
Flavour	Charge(e)	Mass	Flavour	Charge(e)	Mass(MeV)
e	-1	$0.510998910 \pm 0.000000013$ (MeV)	up(u)	+2/3	1.5 to 3.0
ν_e	0	$< 2eV$	down(d)	-1/3	3 to 7
μ	-1	105.658367 ± 0.000004 (MeV)	charm(c)	+2/3 (MeV)	$(1.25 \pm 0.09) \times 10^3$
ν_μ	0	$< 2eV$	strange(s)	-1/3	$(95 \pm 25) \times 10^3$
τ	-1	$1776.99^{+0.29}_{-0.26}$	top(t)	+2/3	$(172.6 \pm 1.9) \times 10^3$
ν_τ	0	$< 2eV$	beauty(b)	-1/3	$(4.20 \pm 0.07) \times 10^3$

Bosons (spin=1)		
Flavour	Charge(e)	Mass(MeV)
gluon	0	0
photon	0	0
W^\pm	± 1	$(80.40 \pm 0.03) \times 10^3$
Z^0	0	$(91.188 \pm 0.002) \times 10^3$
Scalar Bosons (spin=0)		
H^0	0	> 114.4 GeV

Table 1.1: Table of the fundamental particles, fermions and bosons, in the Standard Model [22]

metry group, with gauge bosons W_μ^a , B_μ , A_μ and gauge couplings g_w and g'_w for the corresponding SU(2) and U(1) groups. The mass eigenstates W^\pm , Z^0 and the photon can be identified as a linear superposition of the W_μ^a , B_μ and A_μ given by the weak mixing angle, θ_w . The coupling of the electroweak force to fermions is characterized by their "hypercharge" (Y) and "weak isospin" (T and T_3), and the corresponding quantum numbers for the three families of fermions are shown in table 1.2. The electric charge, Q of the particle can be calculated by $Q = T_3 + Y/2$.

Fermions are introduced in left-handed doublets and right-handed singlets, as charged weak interactions are observed to occur only between left-helicity fermions. Helicity is the component of the spin along the direction of motion of the particle and it is conserved for massless fermions in the exact SU(2) limit. The left-handed doublets are

$$\begin{pmatrix} \nu_i \\ l_i \end{pmatrix}_L, \begin{pmatrix} u_j \\ d'_j \end{pmatrix}_L \quad (1.2)$$

for lepton flavors i and for quark flavors j, while the right-handed singlets are

$$l_{iR}, u_{jR}, d'_{jR}. \quad (1.3)$$

In the above expression i runs over all lepton and quark flavours. The primes on the down type quark is due to the Cabbibo-Kobayashi-Maskawa formalism ([23]) which was derived to accomodate CP violation in QCD first observed in neutral K meson decays [24]. CP stands for the Charge conjugation and Parity operation which are the global symmetries of the QCD Lagragian [25]. $d'_i = V_{ij}^{CKM} d_j$ shows the relationship between the weak interaction or flavor eigenstates and the mass eigenstates. Because the quark mass eigenstates

Particle	Y	T	T_3
$\begin{pmatrix} u_L \\ d_L \end{pmatrix}, \begin{pmatrix} c_L \\ s_L \end{pmatrix}, \begin{pmatrix} t_L \\ b_L \end{pmatrix}$	1/6	1/2	$\begin{pmatrix} +1/2 \\ -1/2 \end{pmatrix}$
u_R, c_R, t_R	2/3	0	0
d_R, s_R, b_R	-1/3	0	0
$\begin{pmatrix} \nu_{eL} \\ e_L \end{pmatrix}, \begin{pmatrix} \nu_{\mu L} \\ \mu_L \end{pmatrix}, \begin{pmatrix} \nu_{\tau L} \\ \tau_L \end{pmatrix}$	-1/2	1/2	$\begin{pmatrix} +1/2 \\ -1/2 \end{pmatrix}$
e_R, μ_R, τ_R	-1	0	0
$\nu_{eR}, \nu_{\mu R}, \nu_{\tau R}$	0	0	0

Table 1.2: Hypercharge (Y), weak isospin (T; T3) of fermions.

are different from flavor eigenstates there is a coupling between different quark generations, and in the Cabbibo-Kobayashi-Maskawa (CKM) formalism it is parametrised by three mixing angles and one complex phase angle. The measured values of the magnitudes of the elements of the V^{CKM} matrix are ([22]):

$$\begin{pmatrix} V_{ud} & V_{us} & V_{ub} \\ V_{cd} & V_{cs} & V_{cb} \\ V_{td} & V_{ts} & V_{tb} \end{pmatrix} = \begin{pmatrix} (0.974 - 0.9756) & (0.219 - 0.226) & (0.0025 - 0.0048) \\ (0.219 - 0.226) & (0.9732 - 0.9748) & (0.038 - 0.044) \\ (0.004 - 0.0014) & (0.037 - 0.044) & (0.9990 - 0.9993) \end{pmatrix} \quad (1.4)$$

The elements of the CKM matrix are derived from various experimental measurements and theoretical constraints [22]. For example $|V_{cb}|$ and $|V_{ub}|$ can be found from measurements of B decays via the predominant $b \rightarrow c$ and the secondary $b \rightarrow u$ decay. Direct $|V_{tb}|$ measurements are promising while looking at single top quark decays.

In the late 1990s flavour mixing in the lepton sector was confirmed observing neutrino flavour oscillations by several experiments: SAGE, GALLEX and Kamiokande and later by SuperKamiokande. The

analysis of the data from these experiments can be found elsewhere [26]. SM model neutrinos are massless and there is no coupling between different flavors. The first evidence for a deviation from the SM neutrino assumption was observed by Davis looking at solar neutrino fluxes in the 1960's [27].

1.1.2 Quantum chromodynamics (QCD)

QCD is a quantum field theory which describes the strong interactions between quarks and gluons. It is a gauge theory which is invariant under local $SU(3)$ colour gauge transformations with eight gauge bosons to preserve the invariance under these transformations. The eight gauge bosons are identified with the gluons, which mediate the strong interactions between quarks and gluons.

The strong coupling constant g_s , usually redefined as $\alpha_s = \frac{g_s^2}{4\pi}$, is expected to be large as the interactions are strong and this makes it difficult to perform reliable perturbative calculations. This problem is resolved when the running of the strong coupling constant is observed in non-Abelian gauge theories such as QCD. Any physics measurement R in QCD depends on the strong coupling constant α_s , the interaction energy Q and the scale μ , which is introduced as a second scale during the renormalisation to remove the ultraviolet divergences from the perturbation series. As the Lagrangian of QCD does not include the μ parameter, the choice of μ is arbitrary and physics measurements do not depend on it. Frequently $\mu = M_z$ is chosen and α_s is then calculated for any other large scale. The point where α_s becomes large and perturbation theory breaks down (λ_{QCD} scale) turns out to be comparable with the masses of light hadrons (~ 1 GeV) [28]. The phenomenon of the running coupling constant

is experimentally confirmed by several experiments at LEP (CERN, Geneva), SLD (SLAC, Stanford), PETRA and HERA (DESY, Hamburg) and at Tevatron (Fermilab, Chicago). Figure 1.2 shows experimental measurements of the running coupling constant [29]. The coupling constant value decreases as the energy of the interaction increases and above a few GeV the coupling becomes small enough to use perturbation theory for the calculation of the QCD processes. The behavior of $\alpha_s(Q^2)$ at short distances, equivalent to high inter-

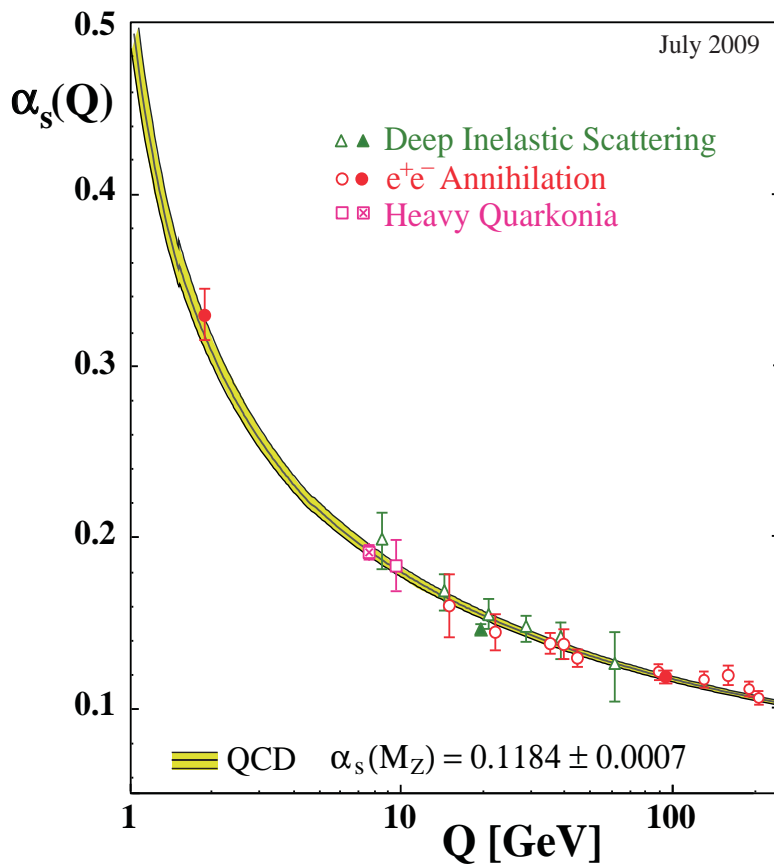


Figure 1.2: The measurements of the strong coupling constant by experiments (various dots) compared to the QCD predictions (yellow band) [29].

action energies, gives rise to the "asymptotic freedom" of quarks and

gluons inside hadrons. As the effective coupling grows for large distances, equivalent to small interaction energies, separating quarks and gluons requires more energy, which leads to the mechanism of "quark confinement". This explains why the bare quarks or gluons have never been seen in a laboratory. The only particles which can be observed are color neutral objects, which are obtained from colored quarks and gluons after hadronisation (see below). During the hadronisation process colored particles are grouped to form colourless objects, the mesons and the hadrons.

1.1.3 Feynman rules of QCD

Feynman developed the graphical representation of the particles and fields of the Standard Model ([30], [31], [32], [33]) to carry out perturbation theory calculations to any finite order. For an example of the application of Feynman rules, the simple two-body scattering process of quarks, antiquarks, and gluons, the basic hard-scattering reaction of QCD is considered in this section. To obtain the scattering cross-section for $(qg \rightarrow qg)$ process using the Feynman rules, one must calculate the amplitude for a gauge boson of momentum p_2 and colour a to scatter off a quark of momentum p_1 and colour i producing a quark of momentum p_3 and colour j and a gauge-boson of momentum p_4 . The following diagrams must be considered in order to account for all processes with the same initial and final states (figure 1.3). Fermions are assumed to be massless and the following Mandelstam variables are introduced:

$$s = (p_1 + p_2)^2 = (p_3 + p_4)^2, \quad (1.5)$$

$$t = (p_1 - p_3)^2 = (p_2 - p_4)^2, \quad (1.6)$$

$$u = (p_1 - p_4)^2 = (p_2 - p_3)^2. \quad (1.7)$$

Each line in the diagram contributes to the scattering amplitude via a corresponding propagator term and each interaction vertex is described by the momentum flow into the vertex.

In the end contributions to the amplitude from all possible graphs (in this case three graphs) must be summed, squared and averaged over external state spin polarization and integrated over the whole phase-space in order to get the scattering cross-section. The result of this evaluation of the cross section is

$$\frac{d\sigma}{dt}(qg \rightarrow qg) = \frac{4\pi\alpha_s^2}{9s^2} \left[-\frac{u}{s} - \frac{s}{u} + \frac{9}{4} \left(\frac{s^2 + u^2}{t^2} \right) \right]. \quad (1.8)$$

The diagrams in figure 1.3 show all possible graphs with the same initial and final states and with the smallest number of vertices, i. e. the leading order (LO) diagrams. However, one can consider diagrams with more vertices which have the same initial and final states. The inclusion of higher-order diagrams will add to the LO amplitude result, supplying higher-order corrections for improved accuracy. The total amplitude is calculated as the linear sum of the contributions from all possible diagrams, at a given order of calculation.

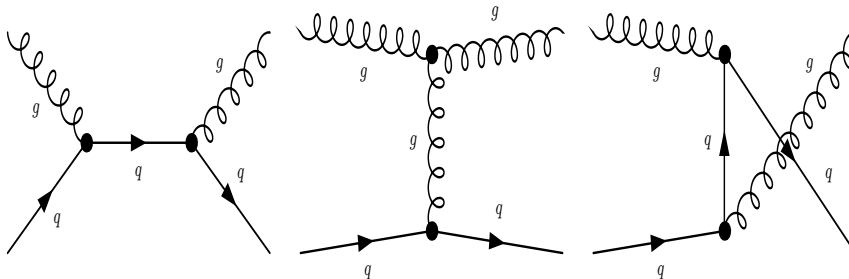


Figure 1.3: Feynman diagrams contributing to $qg \rightarrow qg$.

1.1.4 Hadron collider phenomenology

A hadron collider accelerates and collides hadrons such as protons or antiprotons. The LHC in particular is a proton-proton collider. A pp collision can be divided into two phenomenologically different processes: the long distance and the short distance interactions separated by the factorization scale μ_F^2 . At short distances hard partonic scattering occurs with high momentum transfer and this can be calculated by perturbation theory [34]. At large distances the non-perturbative proton initial state is parametrised by the parton momentum distribution functions (PDFs) which can be interpreted as the probability density to observe a parton of flavour i and longitudinal momentum fraction x_i in the incoming hadron, when probed at a scale μ^2 . PDFs cannot be calculated from QCD theory and instead they are extracted from global QCD fits to deep-inelastic scattering and hadron collider data [35], [36], [37]. In figure 1.4 the parton distribution functions are shown for quark, antiquark and gluon at the scale $Q^2 = \mu^2 = m_t^2$ [38]. It can be seen that the number of gluons grows fast for low x (at high interaction energies) and already at the LHC scale the hard scattering processes are dominated by gluon-initiated production. To demonstrate the factorisation procedure the total cross section of $t\bar{t}$ pair production at hadron colliders is considered. The top quark pairs are produced via strong interactions such as quark-antiquark annihilation or gluon fusion. Feynman digrams of the hard scattering for these processes at leading order are shown in figure 1.5. The total cross section for $t\bar{t}$ pair production with center of mass energy \sqrt{s} can be written in

the following way:

$$\sigma^{\bar{t}\bar{t}}(\sqrt{s}, m_t) = \sum_{i,j=q,\bar{q},g} \int dx_i dx_j f_i(x_i, \mu^2) f_j(x_j, \mu^2) \times \hat{\sigma}^{i,j \rightarrow \bar{t}\bar{t}}(\rho, m_t^2, x_i, x_j, \alpha_s(\mu^2), \mu^2) \quad (1.9)$$

The summation is performed for all $q\bar{q}$, gg , qg , and $\bar{q}g$ pairs. $\rho = 4m_t^2/\sqrt{s}$ and $\sqrt{s} = x_i x_j s$ is the effective center-of-mass energy squared for the partonic process. $f_i(x_i, \mu^2)$ and $f_j(x_j, \mu^2)$ are the parton distribution functions (PDF) for the initial protons. Before and after the hard scattering additional parton radiation can occur, referred to as initial (ISR) and final (FSR) state radiation. The description of ISR and FSR depends crucially on the QCD renormalisation scale discussed in chapter 1.1.2. In event generators these processes are described via initial and final-state parton showering.

Hard scattering remnants of the colliding hadrons can also in-

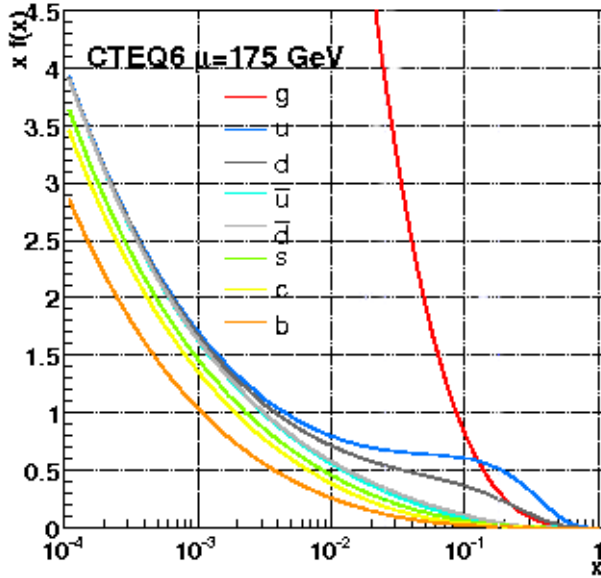


Figure 1.4: Parton distribution functions for quark, antiquark and gluon momentum densities in the proton as a function of the fractional momentum [38].

fluence the final state of the event. The proton remnants are color connected to the hard interaction partons. Multiple hard interactions can occur between the remaining partons, which will also be color connected to the main hard scattering process. This part is referred to as the underlying event and it is difficult to model it in event generators. There can be also contributions coming from the overlap of multiple collisions which are reconstructed as one event. This process is referred to as pile-up.

The final state of the interaction consists of partons originating from hard scattering, from ISR and FSR, from the underlying event and from pile-up. As discussed in chapter 1.1.2 colored particles cannot be observed and only color neutral objects, the mesons and the hadrons formed from partons as described by "hadronisation" models, can be seen experimentally. There are several approaches to model the hadronisation process in the event generators and the

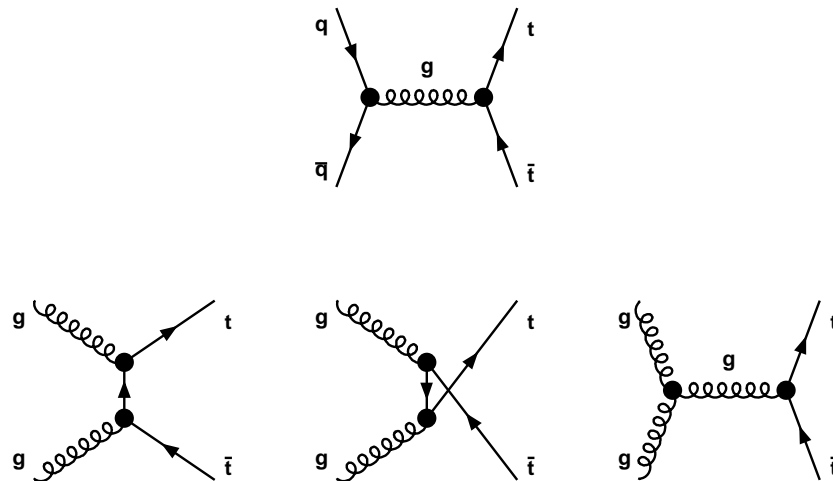


Figure 1.5: Leading order top quark pair production via strong interactions through quark-antiquark annihilation (top row) and gluon fusion (bottom row).

description can be found elsewhere ([39], [40]).

1.1.5 Top quark physics

There are six quarks in the SM shown in table 1.2. Nowadays all of them, namely the up, down, strange, charm, bottom, and the top quark are observed experimentally. They are arranged in three generations forming weak isospin doublets.

The discovery of a third family in the lepton (τ) sector at the SLAC SPEAR e^+e^- ring in 1975 by Perl et al [41] was strong indication that there must be the third family of quarks too. To obtain a renormalisable gauge theory of the weak interactions without anomalies [42] the number of the quark families should be equal to the number of the lepton families. In addition, every quark comes in three colours [43]. The experimentally observed CP violation in Kaon decay explained by the CKM formalism also requires three quark families [23].

In 1977 first the forth, “charm”, quark was discovered at Stanford Positron Electron Asymmetric Ring (SPEAR) and shortly the third generation of the quarks, the bottom (b) quark was observed at the Fermilab proton synchrotron in 1977 [44]. In the following years b quark properties were studied in more detail and flavour changing neutral current decays of the b-quark were not observed. Therefore the b quark is a member of a left-handed weak isospin doublet.

Before the direct discovery of the top quark at Fermilab, there were constraints on the top quark mass obtained from precise electroweak measurements. In the SM the mass of the W boson can be written in the following way [6]:

$$m_W^2 = \frac{\frac{\pi\alpha}{\sqrt{2}G_F}}{\sin^2\theta_W(1 - \Delta r)} \quad (1.10)$$

Here α is the electromagnetic coupling constant, G_F is the Fermi constant and θ_W is electroweak mixing angle defined in the following way: $\sin^2\theta_W = 1 - \frac{m_W^2}{m_Z^2}$. Δr in the denominator contains the one loop corrections to the W mass depending on the top mass and the Higgs mass via the digrams shown in figure 1.6. The one loop corrections from the top quark and Higgs boson can be expressed with the following relations:

$$\begin{aligned}\Delta r_{Top} &\simeq -\frac{3G_F}{8\sqrt{2}\pi^2\tan^2\theta_W}m_t^2 \\ \Delta r_{Higgs} &\simeq \frac{3G_F m_W^2}{8\sqrt{2}\pi^2} \left(\ln \frac{m_H^2}{m_Z^2} - \frac{5}{6} \right)\end{aligned}\tag{1.11}$$

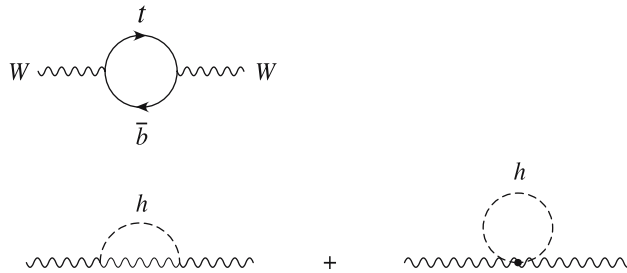


Figure 1.6: Virtual Top quark and Higgs boson loops contributing to the W boson mass.

The most recent indirect top mass constraint from fitting the precision electroweak measurements from LEP, SLD and Tevatron at Fermilab is $m_{top} = 179.4_{-9.2}^{+12.1}$ GeV/ c^2 [45]. It is in good agreement with direct top quark mass measurements. The SM fit of the electroweak precision data for the Higgs and top mass using the W boson and top quark mass direct measurements is shown in figure 1.7.

The first limits on the top mass were set by e^+e^- experiments up to 45.8 GeV/ c^2 . The results from hadron colliders increased this lower limit up to 69 GeV/ c^2 by the Sp \bar{p} S at CERN and up to 131 GeV/ c^2 by the Tevatron at Fermilab. In 1995 top quark

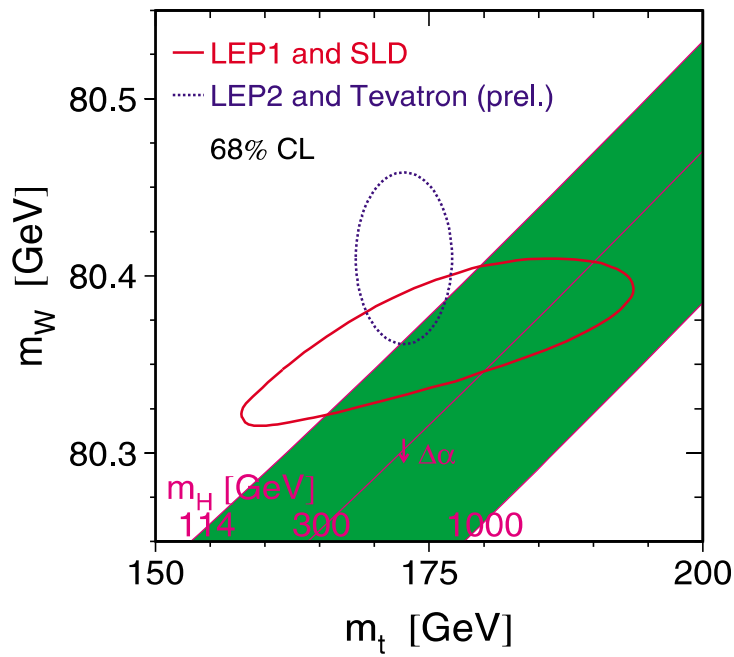


Figure 1.7: SM predictions for m_t and m_W for various Higgs masses on a plot of M_W vs. m_t . The dotted ellipse is the 68% CL direct measurement of M_W and m_t . The solid ellipse is the 68% CL indirect measurement from precision electroweak data.

pair production was discovered at the Tevatron $p\bar{p}$ collider with a center of mass energy $\sqrt{s} = 1.8$ TeV at Fermilab by the CDF and D0 collaborations [4], [5]. In 2009 the discovery of single top production from electroweak interactions was announced by both CDF and D0 collaborations [46], [47]. Recent reviews of top quark physics can be found in [48], [6].

Top quark pairs are produced via strong interactions such as quark-antiquark annihilation or gluon fusion shown in figure 1.5. The next-to-leading order total cross section prediction for the $t\bar{t}$ pair production at LHC is $\sigma = 833(pb) \pm 15\%$ for pp collisions at $\sqrt{s} = 14$ TeV and $m_t = 175$ GeV/ c^2 . The estimated error of 15% considers uncertainties coming from renormalisation scale variations ($\sim 10\%$) from PDFs and from α_s uncertainties ($\sim 6\%$). The large PDF uncertainty is due to the poorly known gluon density at low x values [49] and the dominance of gluon fusion in $t\bar{t}$ production at LHC, where it contributes $\sim 90\%$ of the cross section.

The cross section measurement is sensitive to new physics in top quark production and decay. A new source of top quarks would enhance the cross section, and a new decay mode would suppress the measured cross section value. New $t\bar{t}$ resonance production could also increase the top quark cross section. An accurate estimation of $t\bar{t}$ production is needed for new physics searches as well as for the SM electroweak single-top production measurement as $t\bar{t}$ is an important background for this process. The electroweak single top quark production, like top quark decay, can be used for direct $|V_{tb}|$ measurements.

The top quark decays quickly due to its large mass, and the lifetime is $\sim 5 \times 10^{-25}$ s. With the current knowledge of the CKM matrix (shown in equation 1.4) a top quark decays almost exclusively to a

b quark and a W boson with branching ratio ~ 0.999 . Therefore the decay products of the W boson define the final states of $t\bar{t}$ system. The W boson can decay leptonically ($W^\pm \rightarrow l^\pm \nu_l(\bar{\nu}_l)$, where l^\pm is e^\pm , μ^\pm or τ^\pm) or hadronically ($W^\pm \rightarrow (u, \bar{d})$ or (c, \bar{s})). The branching ratios to the three lepton modes are equal neglecting the lepton masses, totalling one third of the W branching ratio. Two thirds of W decays are hadronic since each quark final state counts threefold due to the colour quantum number of the quarks. The following final states of $t\bar{t}$ systems can be identified: the *all jets* channel when both Ws decay hadronically, the *lepton plus jets* channel when one of the W decays leptonically and the other decays hadronically, and the *di-leptonic* channel when both Ws decay leptonically.

The top quark is the heaviest and best measured quark. The current combined world average top quark mass estimation from the Tevatron is $m_t = 171.4 \pm 2.1 \text{ GeV}/c^2$ [50]. Due to the large value of the top mass close to the electroweak symmetry breaking scale the measurement of the top quark mass is a sensitive probe of new physics.

Although the top quark mass is well known most of the other fundamental properties of the top quark, like electrical charge, spin etc. are not yet known unambiguously. These quantities will be investigated at the LHC or at future e^+e^- annihilation experiments.

1.2 Physics beyond the Standard Model

The good agreement of the SM with experimental observations has been checked only up to few hundred GeV. The most significant experimental deviation from the SM was the observation of neutrino

oscillations. Extension of the current SM is required to accommodate this phenomenon. There are also theoretical concerns and open questions within the current SM: the origin of mass, and why the particle masses are so small (Mass Hierarchy problem). It has not yet been possible to unify the theory to describe all particle interactions including gravity. The SM does not explain the origin of the various particle quantum numbers and the presence of 19 free parameters, and at least 9 additional parameters are needed to model the neutrino oscillation processes [51]. These arguments together with many unexplained phenomena in cosmology require new physics beyond the standard model. The LHC will test the SM and search vigorously for theories beyond the TeV scale. It is believed that most extensions of the SM predict new interactions or new particles at this scale.

Supersymmetry (Susy) is an extension of the SM which was introduced in the 1970s by Wess and Zumino [52]. In this theory a new symmetry between fermionic and bosonic fields is postulated. There are equal numbers of fermions and bosons forming supermultiplets which consist of particles with spins differing by half a unit and with identical couplings. This symmetry doubles the amount of the SM particles requiring a so-called superpartner for each of them. There are several motivations for supersymmetry. It solves the mass hierarchy problem in SM. If the SM were to hold up to Planck scale $m_p \sim 10^{19}$ GeV the loop corrections to the W and H mass would be 36 orders of magnitude higher than the physical values. In Susy the contributions from the fermionic loops are canceled by identical contributions from bosonic loops with opposite sign and left over corrections are of $O(\frac{\alpha}{\pi})(m_B^2 - m_F^2)$. Therefore the masses of the superpartners are expected to be around TeV scale. Susy has

also potential to unify the SM interactions. Another motivation for supersymmetry can be provided by astrophysics. The lightest super partners, if stable, can be good candidates for cold dark matter [51].

1.3 The Large Hadron Collider (LHC)

Probing new areas of high energy physics requires very high energy densities at the interaction points, which poses new challenges to accelerator technologies. Heavy particles produced in a high energy environment will decay to lighter particles and the only way to study interactions which took place at high energies is to reconstruct the decay particles precisely. Therefore sensitive particle detectors are required. In this chapter the LHC accelerator complex and the ATLAS detector are discussed.

The LHC is installed in the 27 km long former LEP tunnel situated at CERN, Geneva, Switzerland. Inside the LHC, bunches of up to 10^{11} protons (p) will collide 40 million times per second to provide a design luminosity of $10^{34} \text{cm}^{-2} \text{s}^{-1}$. An annual integrated luminosity of $\sim 100 \text{fb}^{-1}$ is expected. The center-of-mass (cms) energy of proton-proton collisions is 14 TeV and the total energy stored in each beam is about 360 MJ. The current limit of energy at the interaction point for particle accelerators is set by the Tevatron experiment at Fermilab, which collides proton against anti-proton at a cms energy of 1.9 TeV and has collected about 2fb^{-1} over its ten-year period of operation. In a dedicated operation mode the LHC will also be able to collide heavy lead ions at 5.5 TeV cms energy and at a design luminosity of $10^{27} \text{cm}^{-2} \text{s}^{-1}$ [2]. This is about 10 times higher than the Relativistic Heavy Ion Collider (RHIC) at Brookhaven Laboratory.

The injection complex consists of a 50 MeV linac, the 1.4 GeV PS booster, the 26 GeV PS and the 450 GeV SPS. A schematic view of the LHC and SPS is shown in figure 1.8. The LHC will accelerate equally charged particles and therefore two separate beam-lines are needed to circulate them in opposite directions. 1232 dipole mag-

Parameters	Value
Ring circumference	26658.883 m
Number of particles	1.15×10^{11} per bunch
Number of bunches	2808
Bunch spacing	25 ns
Center of mass energy	14000 GeV
Design luminosity	$10^{34} \text{ cm}^{-2} \text{ s}^{-1}$
Events per bunch crossing	19

Table 1.3: Nominal LHC beam parameters [2].

nets (figure 1.9) are used to bend the 7 TeV proton beams. The superconducting dipole magnets have a length of 14.2 m and are maintained at a low operation temperature of 1.9 K with a design field strength of 8.36 T. The two guiding magnetic fields for both directions are produced by a single structure. A total of 392 superconducting quadrupole magnets, which are 3.1 m long and reach a field strength of 6.9 T, are used in the straight sections of the LHC for beam focusing towards the four collision points where the detectors are located. At each collision point one of the four detectors is built: ATLAS detector (Point 1), ALICE detector (Point 2), CMS detector (Point 5) and LHCb detector (Point 8). The injector complex, the LHC main ring and the 4 collision points are shown in figure 1.8. In table 1.3 some of the parameters of the LHC machine are shown.

The LHC will start operation with 7 TeV cms energy, i. e. 3.5 TeV per beam, at initial low luminosity. Design luminosity will be achieved after a few years of running.

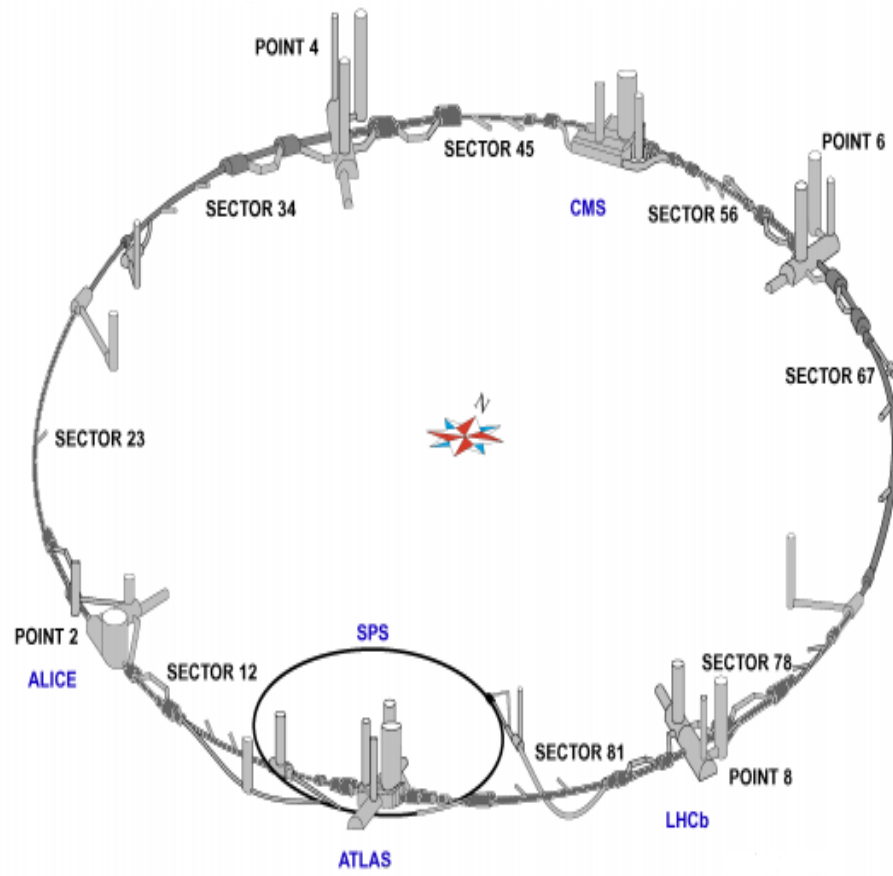


Figure 1.8: Schematic view of the LHC and SPS accelerator rings [2].

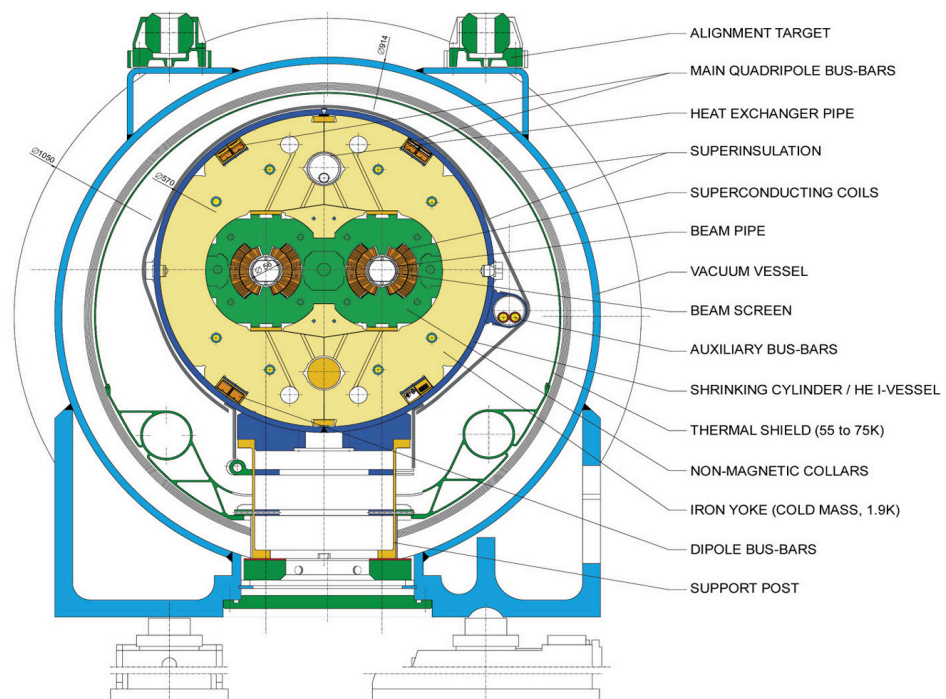


Figure 1.9: Cross section of the LHC beam-pipe with two-in-one dipole magnet and its cryostat [2].

1.4 Physics at the LHC

The LHC will collide protons, which are composite objects containing partons: valence quarks and a sea of virtual quarks and gluons. Each parton carries some part of the momentum from the proton, and therefore the momentum available to the interactions between the partons is much less than the total proton momentum. After the hard scattering of two partons the remaining part of the proton often causes soft scattering processes which go mainly collinear to the beam direction. Events which only contain soft scattering are called minimum-bias events and the total cross section is predicted to be $\sim 70 \text{ mb}^{-1}$ at LHC[2]. The separation time of the proton bunches in the accelerator is 25 ns and there will therefore be an overlap of events from different bunch crossings. Due to the high minimum bias event rates there will be on average ~ 19 events per bunch crossing at design luminosity. This leads to a pile-up of events, i. e. multiple interactions per bunch crossing recorded as one event.

The LHC will provide the opportunity to perform precise measurements of SM parameters and the possibility to extend the searches for evidence of any new physics beyond the SM to the TeV scale [2].

The cross sections of SM processes are shown as a function of \sqrt{s} in figure 1.10. The increase of the rates of SM processes at the LHC with $\sqrt{s} = 14 \text{ TeV}$ cms energy is significant with respect to the ones currently attained by the Tevatron with $\sqrt{s} = 1.9 \text{ TeV}$ cms energy, which will allow high precision measurements of QCD processes and electroweak interactions at the TeV scale. Top quark pairs and single top quarks will be produced frequently at LHC and top quark properties will be studied with more statistics than were

available at the Tevatron experiments.

The search for the SM Higgs boson and its expected decay signatures had a strong influence on the design of the ATLAS detector. Depending on the mass of the Higgs boson (H), corresponding decay channels were studied which involve identification of hadrons or photons as the products of low mass Higgs decays. Associated production of H such as $t\bar{t}H$, WH , and ZH , with subsequent decay $H \rightarrow b\bar{b}$ can be studied using a lepton from the decay of one of the top quarks or the vector boson for triggering and background rejection. SM Higgs bosons with a mass above 130 GeV decay into WW or ZZ pairs resulting in charged leptons in the final states.

New physics at the TeV scale will be tested in many ways. For example, the collaboration will search for new heavy gauge bosons with masses up to a few TeV and possible decays into lepton final states, and also for flavour-changing neutral currents in the lepton sector [51]. For the various supersymmetric models new superpartner particles can be produced at the LHC and their decay chains are predicted to contain leptons, jets and the lightest supersymmetric particle (LSP). If the new SUSY quantum numbers are conserved, the LSP is stable and it will escape the detector and give rise to missing energy in the event [51]. Some theoretical models predict extra dimensions and quantum gravity at the TeV scale. In this scenario gravitons are produced at a high rate. Because gravitons escape the detector these events will have significant missing energy as an experimental signature. In other extra dimensional models Kaluza-Klein excitations of particles are produced as resonances with large invariant masses [51].

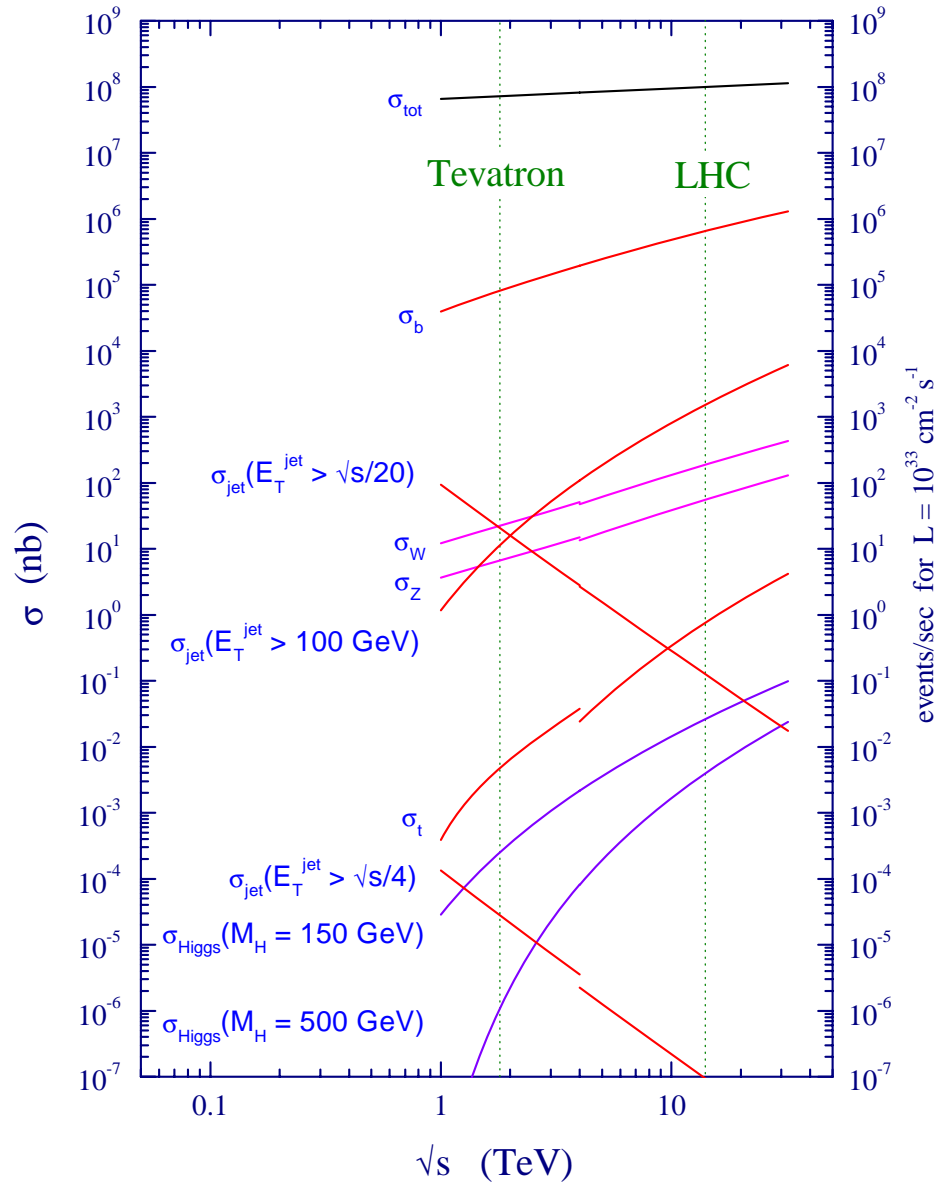


Figure 1.10: The SM proton - (anti)proton cross sections.

1.5 The ATLAS detector

High interactions rates and radiation doses, large particle multiplicities per event and high energies at the interaction points as well as the precision of the measurement which is required for the physics goals pose challenges for the design of the particle detectors. Two general purpose detectors, ATLAS (A Toroidal LHC ApparatuS) and CMS (Compact Muon Solenoid) are located at point 1 and point 5 at the LHC. A brief description of the ATLAS detector is given in this section.

The coordinate system used in the ATLAS experiment is as follows. The ATLAS global coordinate system is defined as a right-handed system with the nominal interaction point as the origin. The beam direction defines the Z axis, the X axis points from the interaction point to the center of the LHC ring and the Y axis points upwards. Side A of the detector defines the positive direction of the Z axis. The azimuthal angle ϕ is the angle around the Z axis and the polar angle θ is the angle with respect to the beam axis. The pseudorapidity frequently used in hadron collider measurements is defined as $\eta = -\ln \tan(\theta/2)$ for objects with negligible mass compared to energy, while for massive objects we have rapidity $\eta = 1/2 \ln[(E + p_z)/(E - p_z)]$ [2].

Other coordinate systems used to describe the ATLAS geometry and the corresponding transformation procedures between the different coordinate systems will be also discussed where necessary.

Detector design overview

The LHC is a hadron collider and cross sections of the interesting processes are considerably smaller than QCD production rates.

Also due to the high interaction rates (table 1.3) at design luminosity every hard interaction event will in average coincide with ~ 19 inelastic events per bunch crossing. Good object identification, reconstruction and selection are therefore crucial for precise physics measurements and new discoveries. For this reason the following set of requirements was identified for the ATLAS detector design:

- fast and radiation hard electronics and sensor elements,
- high detector granularity to cope with the high track density,
- large acceptance to insure that interesting central events are contained in the detector,
- good charged particle momentum resolution and track reconstruction efficiencies,
- good electromagnetic and hadron calorimetry for accurate jet and missing transverse energy measurements,
- good muon reconstruction, momentum resolution and charge identification.

The layout of the ATLAS detector is shown in figure 1.11. A strong magnetic field is used to bend the trajectories of the charged particles and to achieve the high momentum resolution measurements. The experiment is constructed with various subdetectors to meet the conditions listed above.

The magnetic field is generated by a superconducting solenoid with field strength of 2T surrounding the inner detector. The Inner Detector serves to reconstruct the trajectories of charged particles with high precision. The ID consists of the following tracking subdetectors: Pixel detector, SemiConductor Trackers (SCT), and the Transition Radiation Tracker (TRT).

The calorimeter system measures the energy deposits of electromagnetic and hadronic particles employing the high granularity of the various calorimeter systems: electromagnetic (EM), hadronic central and forward calorimeters.

Three large superconducting toroids including a barrel and two end-caps are arranged with an eight-fold azimuthal symmetry around the calorimeters as shown in figure 1.11. The muon spectrometer located inside the toroid field provides the muon identification and track reconstruction with high momentum resolution and consists of three layers of drift tube chambers (MDT) and Resistive Plate Chambers (RPC).

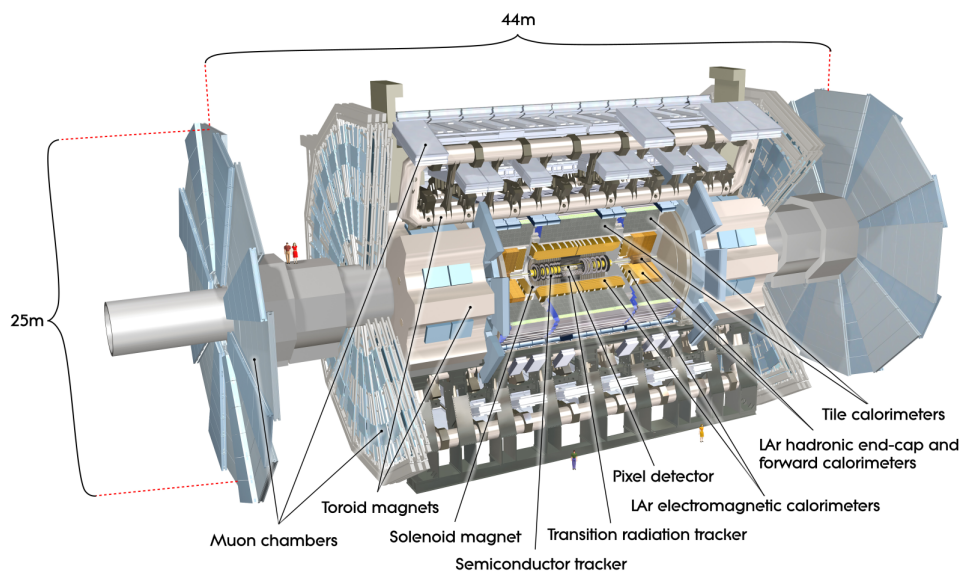


Figure 1.11: The layout of the ATLAS detector. The dimensions of the detector are 25 m in height and 44 m in length. The mass of the detector is ~ 7000 tons.

1.5.1 Inner Detector

The layout of the inner detector is shown in figure 1.12. The ID is located in the central solenoid magnet which has a length of 5.3 m and a diameter of 2.5 m.

In pseudorapidity the Pixel and SCT subdetectors cover the region $|\eta| \leq 2.5$ while the TRT provides measurements within $|\eta| \leq 2.0$. The combination of the three tracking subdetectors provides the desired performance of the ID: three precise Pixel measurements near to the interaction point give good impact parameter measurements and decay vertex reconstruction for heavy-flavour and τ -lepton identification. The lower single hit accuracy of the outer parts of the ID (SCT and TRT) is compensated by the larger number of measurements and the large lever arm. The expected transverse momentum resolution for the ATLAS tracking detector is $\sigma_{p_T}/p_T = 0.05\%p_T \oplus 1\%$ [2].

The pixel detector is made from oxygenated n-type silicon wafers with n^+ pixel implantations. When charged particles pass the active volume they create electron-hole pairs. In the electric field between the sensor surfaces they drift towards the electrodes inducing a signal in the frontend electronics.

The pixel detector is located around the beam line at a radial distance of 5.05 – 12.25 cm from the interaction point. The pixel detector consists of a total of 1744 rectangular modules with 46080 pixel channels each and a pixel pitch of size $50 \times 400 \mu\text{m}^2$ in $(R-\phi) \times z$. The pixel detector in total has ~ 80.4 million readout channels. The high granularity of the pixel modules provides precise spatial information for good momentum resolution and both primary and secondary decay vertex reconstruction. It was designed to provide

3 measurements per track. The pixel modules are arranged on 3 cylindrical layers in the barrel region ($5.05 \text{ cm} < R < 12.25 \text{ cm}$) and on 2×3 disk in the end-cap regions ($49.5 \text{ cm} < |Z| < 65.0 \text{ cm}$). The intrinsic accuracies in the barrel and in the disks regions are $10 \mu\text{m}(R - \phi)$ and $115 \mu\text{m}(z)$.

The SCT consists of silicon strip detector modules. The detector operation is based on the same principle as the Pixel detector.

The SCT detector is located around beam line at a radial distance of 22.4-49.8 cm from the interaction point. The SCT detector consists of a total of 2112 barrel and 988 end-cap double and single-sided modules with 768 readout strips on each silicon sensor. The strip pitch for SCT modules in the barrel region is $80 \mu\text{m}$. In the barrel region the SCT modules have two sides: one side with a set of strips parallel to the beam direction, and on the back side the readout strips rotated by a small stereo angle of 40 mrad with respect to the beam line to increase the resolution along the z coordinate. In the endcap region the SCT modules are either one silicon sensor (short modules) or two silicon sensors (long module). For the long modules as in the SCT barrel on one side the set of strips are running radially and on the other side a set of stereo strips are running at an angle of 40 mrad with respect to the radial strips. The pitch of the strips in the end cap regions starts at $55 \mu\text{m}$ and increases along the radial direction up to $95 \mu\text{m}$. Total number of readout channels in the SCT is ~ 6.3 million. Typically the SCT provides 8 measurements per track with intrinsic accuracies per module in the barrel and in the discs of $17 \mu\text{m}$ in $(R - \phi)$ and $580 \mu\text{m}$ in z . The SCT modules are located in 4 cylindrical layers in the barrel region at radial distances 22.4 - 49.8 cm and on 2×9 disks in the end-cap regions at distance $85.38 < |Z| < 272.02 \text{ cm}$.

The largest part of the ID volume is covered by the TRT sub-detector at radii from 56.3 cm to 106.6 cm. The TRT is constructed of thin polyimide drift straw tubes of 4 mm diameter. The anodes are $31 \mu\text{m}$ diameter tungsten wires plated with gold. For the operation gas a mixture of 70% Xe, 27%CO₂ and 3%O₂ is chosen. In the barrel region 144 cm long straws are arranged parallel to the beam direction on 73 planes. In the endcap regions 37 cm long straws are placed vertical to the beam axis in 160 planes. The total number of TRT readout channels is ~ 351000 . The TRT only measures $R - \phi$ information and provides on average 36 measurements per track with an intrinsic accuracy of $130 \mu\text{m}$ per straw.

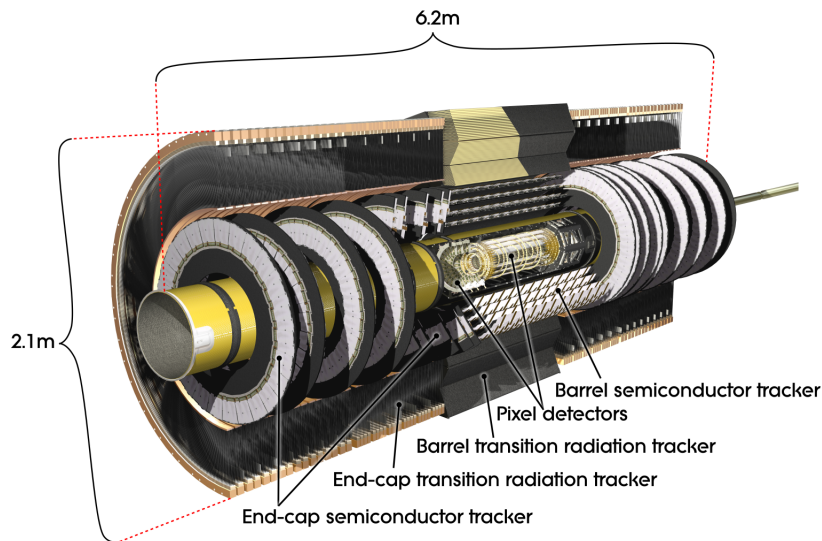


Figure 1.12: The layout of the ATLAS inner detector.

1.5.2 Calorimetry

The ATLAS calorimeter system consists of three parts: electromagnetic (EM), hadronic and forward calorimeters. They cover the pseudorapidity range $|\eta| \leq 4.9$. The wide range of the accep-

tance and the fine granularity of the calorimeter serves to satisfy the physics requirements for jet reconstruction and missing energy (E_T^{miss}) measurements [2].

The EM calorimeter is a liquid Argon (LAr) detector with accordion-shaped kapton electrodes and lead absorber plates. When high-energy photons or electrons traverse the lead they produce electromagnetic showers and electrons and positrons from the shower passing through the liquid argon ionize its atoms. Ionization electrons are drifting in an electric field towards the absorber plates and are measured as a signal. The signal size is proportional to the energy of the primary particle. The EM calorimeter barrel covers angles at $|\eta| \leq 1.4$ and the endcap covers angles at $1.375 \leq |\eta| \leq 3.2$. Fine segmentation is used for the precise electron and photon reconstruction in the central region $|\eta| \leq 2.5$. The cell granularity in this region is $\Delta\eta \times \Delta\phi = 0.025 \times 0.025$. In the range $2.5 < |\eta| < 3.2$ the cell size is larger $\Delta\eta \times \Delta\phi = 0.1 \times 0.1$.

The hadronic calorimeter measures energy deposits of hadrons: protons and neutrons, pions and kaons. In the case of the Tile hadronic calorimeter hadronic showers are formed in the steel plates and the shower particles traverse the scintillating tiles such that the emitted light is proportional to the energy of the incident particle. In the end-cap regions where the intensity of particles is higher liquid argon is used as active medium to increase resistance against high radiation rates while copper plates serve as absorbers.

The hadronic calorimeters consist of a Tile barrel, two Tile extended barrel calorimeters and two Hadronic End-cap Calorimeters (HEC). The barrel hadronic calorimeter and extended barrel calorimeters cover the range $|\eta| \leq 1.7$. The cell granularity in the barrel region is $\Delta\eta \times \Delta\phi = 0.1 \times 0.1$. The HEC covers the range

$1.5 \leq |\eta| \leq 3.2$ with the cell granularity of $\Delta\eta \times \Delta\phi = 0.1 \times 0.1$ for $1.5 \leq |\eta| \leq 2.5$ and $\Delta\eta \times \Delta\phi = 0.2 \times 0.2$ for $2.5 \leq |\eta| \leq 3.2$.

The forward calorimeters cover the range $3.2 \leq |\eta| \leq 4.9$ and use copper and tungsten rods and tubes parallel to the beam axis. The LAr in the volume between the rods and the tubes is the sensitive medium. The cell sizes in the forward calorimeters vary from $\Delta X \times \Delta Y = 3.3 \times 4.2\text{cm}^2$ to $5.4 \times 4.7\text{cm}^2$.

In total, the calorimeters of ATLAS have 260000 readout channels.

1.5.3 Muon system

The muon system is the outermost subdetector of ATLAS. It is located inside the large superconducting air-core toroid magnets which consist of a barrel toroid and two end-cap toroid magnets. Each toroid contains eight coils assembled radially and symmetrically around the beam axis. The magnetic field is centered on the beam line and reaches a maximum of 4.1T. It is mostly orthogonal to the muon trajectories to provide momentum resolution independent of the pseudorapidity. In the barrel region the muon chambers are arranged in three cylindrical layers around the beam axis. In the end-cap region three layers of the chambers are installed in planes perpendicular to the beam. There are several chamber types used in the muon system: for precision muon trajectory reconstruction 1088 Monitored Drift Tube chambers (MDT) for the barrel and 32 Cathode Strip Chambers (CSC) for the forward regions are used. The total number of readout channels for the muon tracking chambers is 385000. The MDT chambers have optical alignment monitoring with about 12000 sensors to achieve a precision of $30\mu\text{m}$ for the

relative alignment of the chambers.

For fast muon identification and triggering as well as measurement of the muon coordinate in the direction orthogonal to the tracking chambers the muon system also has 544 Resistive Plate Chambers (RPC) in the barrel and 3588 Thin Gap Chambers (TGC) in the end-cap regions. These cover the pseudorapidity range $|\eta| \leq 2.4$. First level muon triggering is based on trigger chamber track segment reconstruction. The total number of readout channels for the muon trigger system is 691000.

The MDT chambers employ aluminium-walled gaseous drift tubes. Charged particles passing the tubes ionize the gas and the electrons are accelerated towards the central anode wire. Close to the wire the kinetic energy of the electrons is large enough to create secondary ionizations leading to avalanches which are measured. The CSC used in the forward regions where the radiation is higher are realized with multi-wire proportional chambers. For the trigger chambers in the barrel regions RPC gaseous parallel electrode-plate tubes without wires are used since the time for collecting the charge is much shorter than for the MDT. For the forward trigger chambers (TGC) multi-wire proportional chambers are used as for the CSC chambers.

For a high momentum muon the muon-spectrometer performance is independent of the inner-detector system and the expected transverse momentum resolution is $\sigma_{p_T}/p_T = 10\%$ at $p_T = 1 \text{ TeV}$ [2].

1.5.4 Trigger and Data Acquisition System

For ATLAS a 3 level trigger system was designed. The aim of the trigger system is to reduce the initial bunch crossing rate from 40 MHz down to the data recording rate of 200 Hz. On figure 1.13

a schematic representation of the ATLAS Trigger System is shown [2].

The Level 1 (L1) trigger is hardware based and uses only parts of the available detector information. The muon system measurements are represented by the trigger chamber (RPC/TGC) information and only reduced-granularity information of the calorimeter system is used. No information of the tracking system is considered. The central L1 trigger processor attempts to find high transverse momentum muons, electromagnetic clusters, jets, τ -leptons, missing transverse energy, and large total transverse energy. This procedure is performed in less than $2.5 \mu s$. The data rate after applying the L1 trigger is reduced to 75 kHz. L1 accepted events are transferred first to the Readout Drivers (ROD) of each sub-detector and afterwards the signal of all detector components are sent to the data acquisition (DAQ). L1 also defines the Regions-of-Interest (RoI) in η and ϕ space for various physics signatures which are used afterwards by the High Level Trigger (HLT).

The Level 2 (L2) trigger uses full information from the detector but processes the events only within the RoIs. The L2 trigger reduces the trigger rate to 3.5 kHz in about 40 ms. Information about the L1 and L2 accepted events are stored in DAQ local buffers.

The third trigger level is the Event Filter (EF) based on offline reconstruction using measurements from every subdetector. The EF improves the event selection and brings the trigger rates down to 200 Hz in a few seconds. After the final event selection by the EF the data are transferred to permanent storage at the CERN computer center.

The DAQ provides the data flow management, configuration, control and monitoring of the hardware and software components

of the detector.

The Detector Control System (DCS) monitors the operation of all subdetectors and has direct interaction with the detector hardware components to adjust operation parameters.

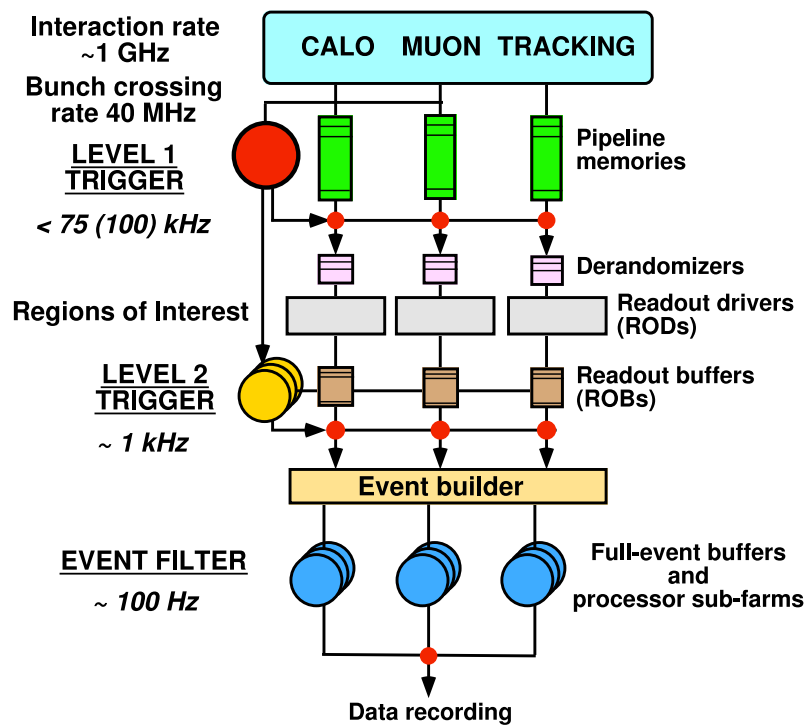


Figure 1.13: Schematic representation of the ATLAS Trigger System [2].

Chapter 2

Track based alignment of the Inner Detector

The ATLAS Inner Detector (ID), consisting of the silicon pixel detector, the SemiConductor Tracker (SCT) and the Transition Radiation Tracker (TRT), serves to reconstruct and measure the momenta of charged particles as well as primary and secondary decay vertices. The precision of the measurement depends on the intrinsic resolution of the detector elements which varies for the different detector element types and is a property of their design [2]. In addition to the intrinsic resolution, the overall measurement precision depends on the knowledge of the position of the detector elements, known as the detector alignment.

The overall required alignment precision, driven by physics motivations, is given in table 2.1. The limits are obtained by requiring that the alignment uncertainty must not degrade the track parameter resolution by more than 20% with respect to the values with perfect alignment [2]. More tight limitations are derived from the momentum scale constraints for precise Z and W boson invariant

Coordinates	Required precision			
	Pixel		SCT	
	Barrel	Endcap	Barrel	Endcap
x [μm]	7	7	12	12
y [μm]	20	20	100	50
z [μm]	20	100	50	200

Table 2.1: Required alignment precision for the various silicon detector elements [2]. Coordinate axes (x, y, z) denote the local [54] frame of a silicon detector module (see section 2.1).

mass measurements [53].

In order to make full use of the ATLAS Inner Detector, the positions of the sensitive elements have to be determined using an alignment algorithm. Different alignment techniques are used in ATLAS: direct detector survey [55], hardware based alignment (frequency scanning interferometry (FSI) [56]), and track based alignment. In the following studies only track based alignment is considered.

A charged particle generates on average 10 hits in the SCT and Pixel subdetectors [2]. The distances between the fitted track and hits associated with this track are called residuals (for an exact definition of residuals see section 2.4). The pattern recognition algorithm and the subsequent track fitting tries to get the best fit of the trajectory of the charged particle in the detector volume, changing the track parameters to minimize the residuals. Track based alignment algorithms are based on minimization of the residuals, by changing the assumed position of the detector elements while keeping the track parameters fixed.

Two of the ATLAS coordinate systems are used in the context of ID alignment [57]. The global coordinate system for ID tracking is a right-handed three-dimensional orthogonal coordinate system

whose z -axis is parallel to the direction of the magnetic field in the inner detector. The origin lies at the nominal interaction point, and the x -axis points to the center of the LHC ring. Coordinates in this frame are denoted with (X, Y, Z) and directions are given using the angles θ , which is the deflection with respect to the z -axis, and ϕ , which is the angle around the z -axis starting from the x axis.

Each detector module (x, y, z) has its own unique right handed local coordinate system denoted by (x, y, z) . For SCT and pixel modules it lies in the plane of the detector with the origin at the center of the module. The x -axis points in the direction across the short coordinate of the strip, the y -axis points in the direction along the long coordinate of the strip and the z -axis is perpendicular to the surface and oriented away from the interaction point [58].

The main purpose of this chapter is to show that a common vertex per event can constrain the end point of tracks strongly. Afterwards the tracks are used as input to the alignment, leading to improved results. Results were obtained by applying the vertex constraint for the local χ^2 alignment approach [59, 58].

2.1 Data sets

Several sets of simulated data are used to examine the performance of the ATLAS detector and to check the whole software chain from trigger to calibration and alignment to derivation of physics results. Details about simulated data used in our studies follow.

2.1.1 Multimuon samples

The multimuon samples were generated with the ATLAS offline software framework 11.0.5 [60]. 10 muons per event were generated from

a common vertex. The vertex distribution (X, Y, Z) was spread around the nominal interaction point $(0,0,0)$ with a Gaussian distribution with widths of $(0.015, 0.015, 56.0)$ mm in (X, Y, Z) .

Particle momenta were generated with flat distributions in transverse momentum p_T and in azimuthal angle ϕ and in pseudorapidity η , using $p_T \in [2; 50] \text{ GeV}$, $\phi \in [0; 2\pi]$, and $|\eta| < 2.5$. These samples were generated and reconstructed with the nominal geometry of the ATLAS detector corresponding to perfect alignment of the detector. We will use this dataset to check the performance of the vertex constraint tool.

2.1.2 The Computing System Commissioning (CSC) Data challenge

The Computing System Commissioning data challenge was intended to exercise the full ATLAS software chain. To be as realistic as possible the Monte Carlo events were generated considering possible misalignments of the detector modules [61]. For reconstruction the nominal geometry of the ATLAS detector was used and the alignment algorithms were exercised in order to see how well misalignment can be corrected under realistic conditions.

For the CSC data, the misalignment of the ATLAS Inner Detector was introduced in the following way: different levels of transforms needed to be generated in order to test the alignment algorithms with a realistic detector description as close as possible to the real experiment. For this the ATLAS calibration database provides three levels of alignment transformations. For *level3* transforms misalignments of each SCT or Pixel module were generated. For *level2* transforms misalignments of the Pixel and SCT barrel layers or endcap

	Translations	Rotations
Level 1	O(1 mm)	O(0.1 mrad)
Level 2	O(100 mm)	O(1.0 mrad)
Level 3	O(100 mm)	O(1.0 mrad)

Table 2.2: Order of misalignments applied on different levels for Pixel and SCT [62].

disks were introduced. For *level1* transforms misalignments of the Pixel and SCT subdetectors were applied [62]. The approximate size of the misalignments for each transformation level are shown in table 2.2.

2.2 Track Reconstruction

The charged particles passing the detector volume leave a track which is found and reconstructed by track reconstruction algorithms implemented in the overall ATLAS computing framework [57]. Tracks were represented with respect to the nominal beam line. This is called the perigee representation; a schematic view of this representation is given in figure 2.2. The perigee representation of the tracks is given by a set of five parameters $(d_0, z_0, \phi, \eta, q/p)$, where (d_0, z_0) denote the two coordinates in the intrinsic frame of the nominal z axis and $(\phi, \eta, q/p)$ is a representation of the track momentum in the global frame.

2.2.1 Error scaling

During track reconstruction the hit errors were scaled up to make tracking more efficient in the misaligned environment. Hit error scaling is intended to improve the tracking in terms of track scoring,

outlier flagging, tracking efficiency and parameter resolution [63]. The discrepancy between the scaled hit error and the unscaled hit error provided by the clustering algorithm can be explained by noting effects of misalignment and imperfect calibrations. To modify the error matrix for each measurement on a track two parameters a and c were introduced to translate the intrinsic resolution σ to the scaled resolution σ' :

$$\sigma'^2 = a^2 \sigma^2 + c^2 \quad (2.1)$$

The intrinsic detector resolution σ is multiplied by the factor a to correct for effects which increase the measurement error. The constant term c added in quadrature absorbs effects such as misalignments which do not change the intrinsic detector resolution. These parameters were tuned for different parts of the detector (Pixel, SCT and TRT), parameterized in ϕ and η coordinates. In total 16 error scaling parameters for the Inner Detector are used [63].

For the analysis of the calibration effects the multiplicative discrepancy of the pull distribution width from 1.0 can be directly used as the error scaling factor a . The pull is calculated as ratio of the track residual and the error on the hit measurement. To cover residual misalignments with the measurement errors the additive term c^2 is introduced to the covariance matrix. The derivation of the mean (p_{obs}) can be seeded by an educated guess from simulation displacements, detector survey, or a previous iteration. Taking into account such a guess in form of an already added term c_0 to the mean intrinsic error σ_0 of a certain detector part, the new tuning c is calculated to be [63]:

$$c^2 = (p_{obs}^2 - 1)a^2 \sigma_0^2 + p_{obs}^2 c_0^2 \quad (2.2)$$

2.3 Vertex Reconstruction

The track fit can be improved using the information that in one event most tracks come from a common vertex. This information can be used in different ways. It can be used implicitly, by parametrising track parameters constrained at the vertex point. This approach is used in the Global χ^2 alignment [64]. Alternatively it can be used explicitly by refitting the tracks with the vertex point. This is the method which we use in Local χ^2 alignment.

This procedure influences tracking, therefore tracks before and after including the vertex point were compared. Since vertices are reconstructed for each alignment iteration, the alignment procedure can be monitored by looking at the vertex position distributions.

2.3.1 Vertex fitting

The vertex constraint uses the information of a common vertex per event to refit the tracks with that vertex point. The first step of the procedure is to reconstruct the common vertex per event. The input of the refit with vertex tool is therefore the track collection. No additional track selection is implemented in the tool itself. Track selection can be performed using the track selection tools to obtain optimized track collections before vertex reconstruction. It is also possible to use track quality cuts implemented in the vertex fitter tools.

Vertices can be reconstructed using different vertex fitting algorithms. There are application packages for the vertex fitter, in which additional constraints such as a mass constraint or a beam spot constraint are implemented. We used the beam spot constraint within our studies.

2.3.2 Refit of tracks with vertex

After reconstructing a common vertex per event the next step is to add this information to the individual tracks. One way to do this is to refit the track and to consider the vertex point explicitly [65]. For this procedure the common vertex position is added to each track as an additional measurement point. A new measurement collection for each track is provided and passed to a track fitter. Thus, as a final result one obtains a new refitted track collection. The vertex constraint tool, `RefitWithVertexTool`, is implemented in the ATLAS software package (Athena) and can be used for any track based alignment approaches.

2.3.3 Performance Studies

For performance studies we used data generated and reconstructed with the nominal geometry described in section 2.1.1. The reconstructed vertex distributions are shown in figure 2.1. The reconstructed vertex distributions are centred at zero and the RMS values are close to the generated width of the vertex distribution given in section 2.1.1.

The beam constraint to the vertex reconstruction procedure was applied using the primary vertex reconstruction package. The beam spot profile is centered at $(0, 0, 0)$ with a Gaussian (X, Y, Z) spread of $(0.015, 0.015, 54.0)$ mm. The beam constraint is applied only to x and y directions, as the measurement of the beam spread for the z coordinate is not accurate.

The vertex x and y distributions had smaller width when the beam constraint was used, shown in figure 2.1. The distribution for the z coordinate remained the same, because the beam spot

constraint was imposed only on the x, y coordinates [66].

As explained above the tracks were refitted with the vertex point. A comparison of the track perigee parameters before and after adding the common vertex per event to each track are shown in figure 2.3. The track perigee parameter distributions did not change after this procedure.

2.4 Alignment of the ATLAS Inner Detector

The local χ^2 alignment approach treats the 1744 pixel modules and the 4088 SCT modules of the ATLAS ID independently and uses a linearized χ^2 minimization of the residuals with respect to the six degrees of freedom of a rigid body to get the alignment corrections for each module [59, 58].

Residuals are defined as the smallest distance between the track trajectory and the hit position. In plane residuals are the projected length on the detector surface. For the local χ^2 approach, the Distance Of Closest Approach (DOCA) between the track and the hit is used to define the residual. The hit position is given by the straight line corresponding to the readout-coordinate of the detector, as shown in figure 2.4.

In the local χ^2 alignment approach correlations between the modules are not considered explicitly. The correlations between modules are restored via iterations. In the data set which was used to find the alignment parameters the tracks are reconstructed again with the new alignment parameters before the next iteration. This procedure indirectly restores the neglected correlations in the local alignment approach [59, 58].

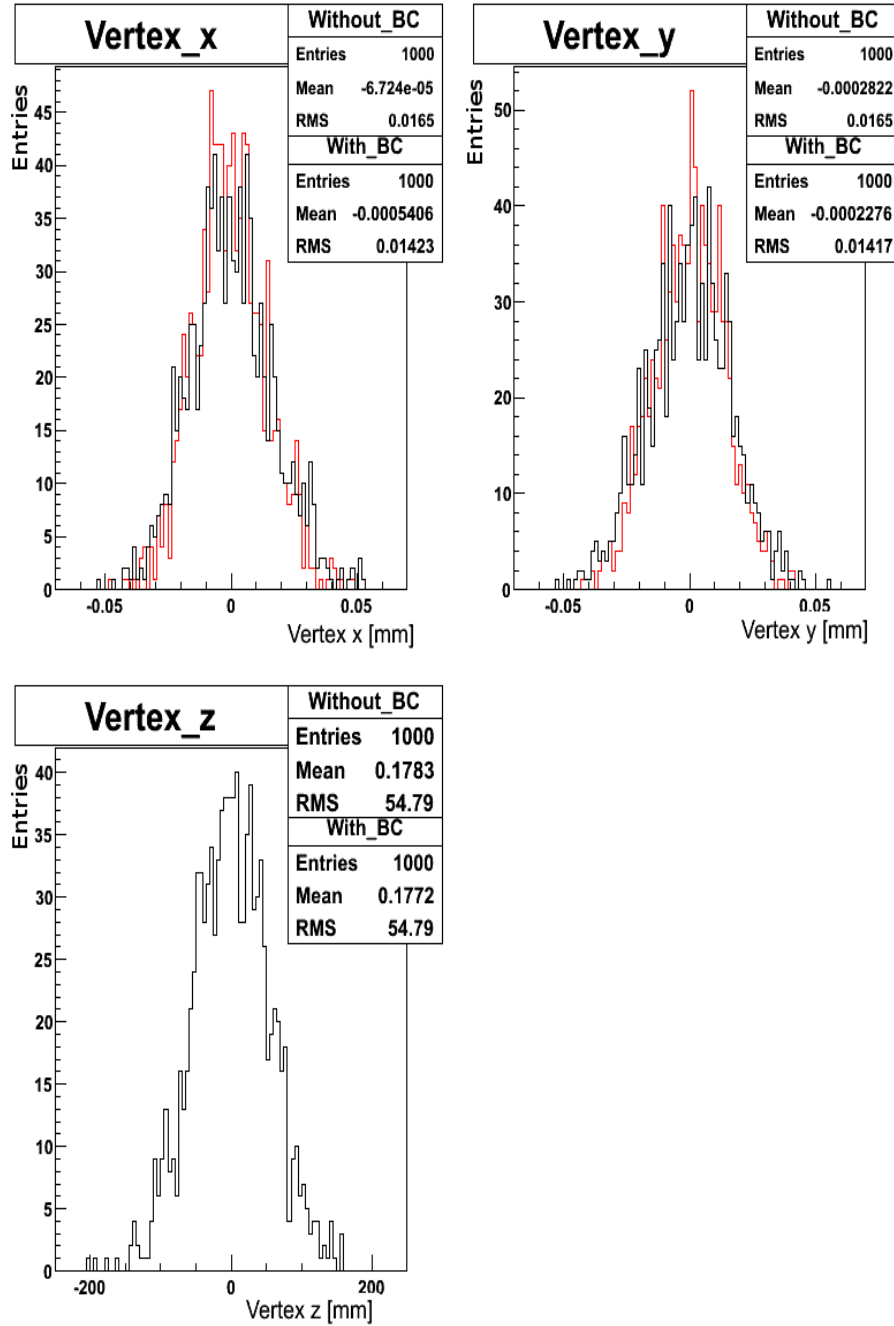


Figure 2.1: Reconstructed vertex distributions for multimueon samples with nominal geometry and with (red) and without (black) beam constraint (BC). Coordinate axes (X, Y, Z) denote the global [54] frame of the ATLAS detector.

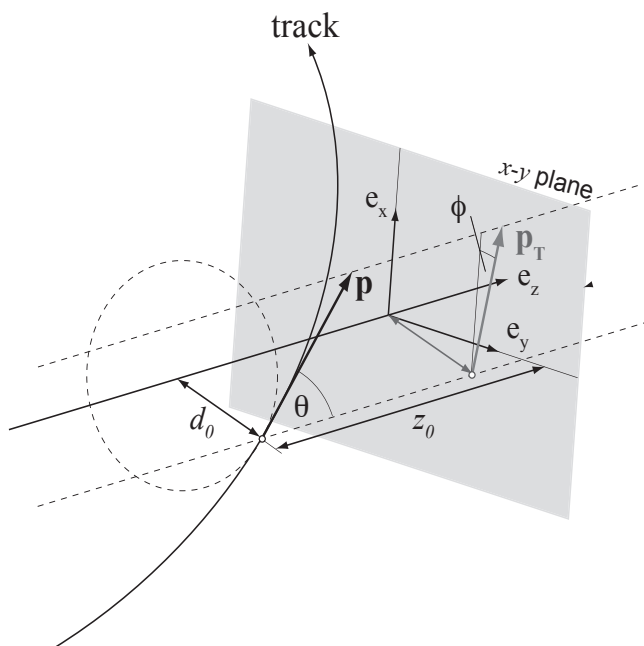


Figure 2.2: The perigee representation of the tracks is given by a set of five parameters $(d_0, z_0, \phi, \eta, q/p)$, where (d_0, z_0) denote the two coordinates in the intrinsic frame of the nominal z axis and $(\phi, \eta, q/p)$ is a representation of the track momentum in the global frame, where $\eta = -\ln[\tan(\theta/2)]$ [57].

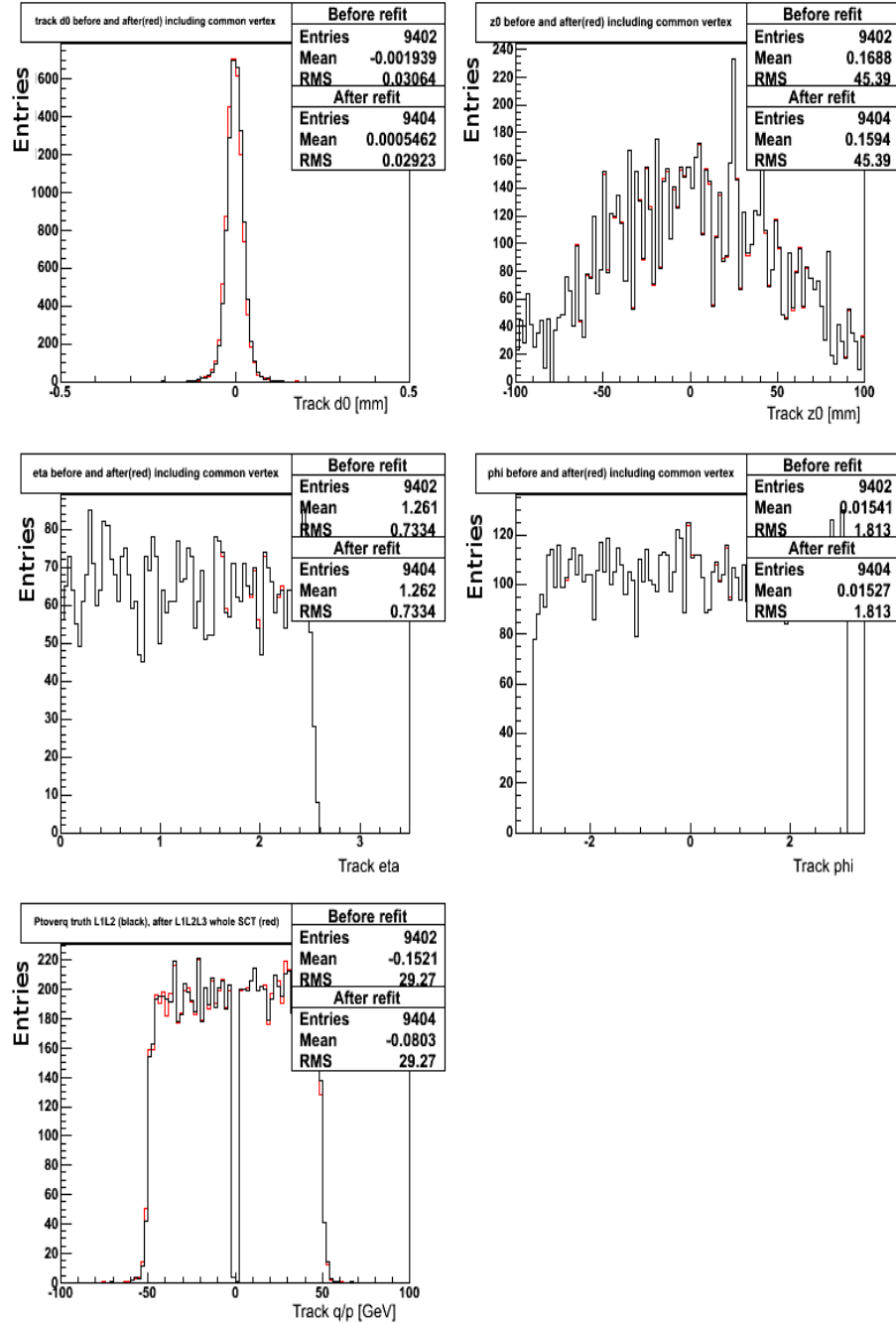


Figure 2.3: Track perigee parameters before (black) and after (red) refitting including the vertex point using multimueon samples.

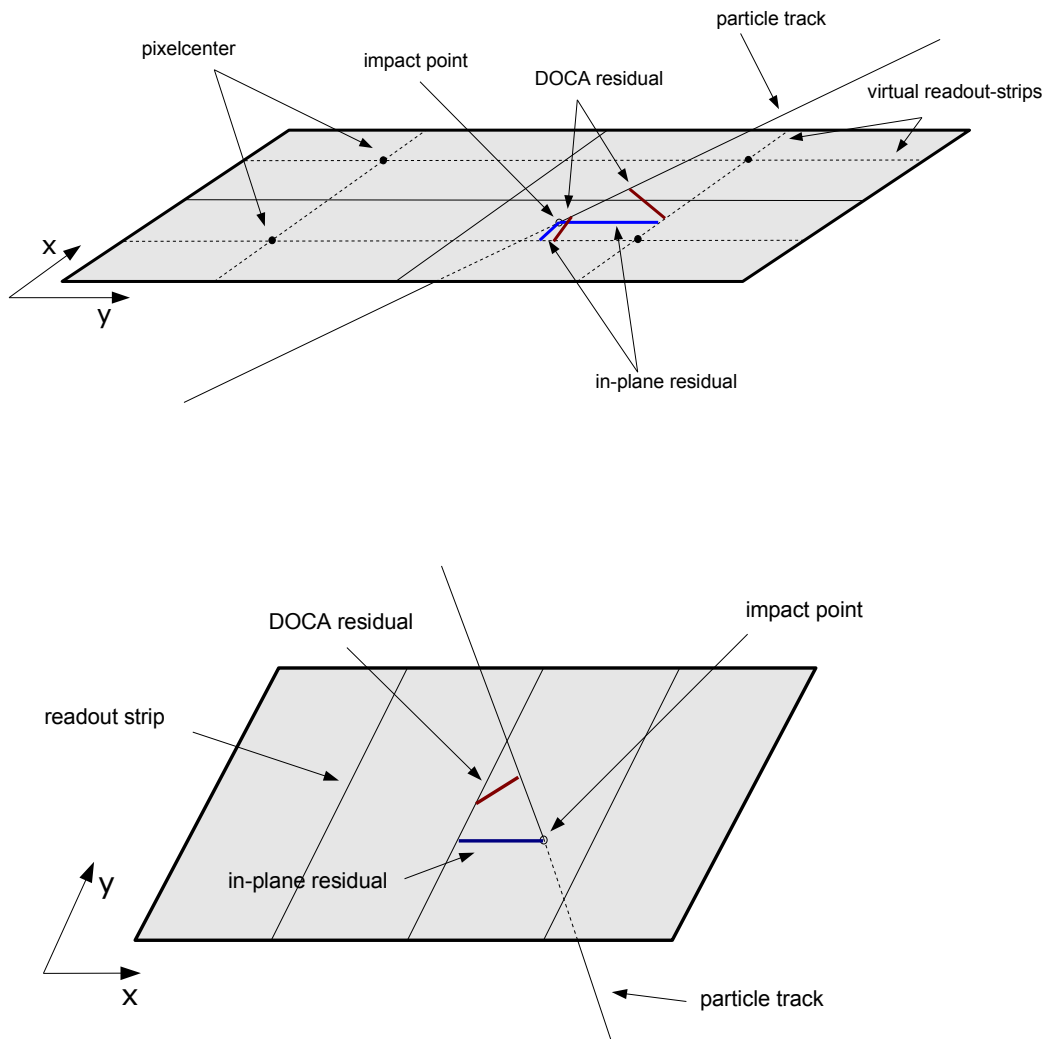


Figure 2.4: The definition of distance of closest approach (DOCA) residuals for the Pixel (top) and SCT (bottom) modules. The blue lines are used for the in-plane residuals and the red lines denote the DOCA residuals.

2.4.1 Including the vertex information in the local χ^2 alignment

The track error is given by the propagated error matrix of the track parameters. The error of the track fit corresponding to the innermost Pixel layer is generally higher than for other parts of the Inner Detector, because the innermost pixel layer is at the beginning of the track and there is no subsequent interpolation of the track [58]. An alignment procedure for these modules needs more iterations to converge. The vertex point used as an additional measurement to the track improves the track fit error for the innermost Pixel layer and thus can improve the alignment.

In addition the vertex point correlates more modules in one event compared to the standard Local χ^2 alignment. Therefore it can improve the alignment procedure, making it more robust.

Including the vertex point can provide sensitivity to weak modes. Weak modes are translations and rotations of the detector elements which do not change residual distributions for the given data samples. The χ^2 expression depends only weakly on these parameters, which leads to degenerate solutions of the χ^2 minimization. In order to handle these kinds of distortions a combination of different kinds of track collections are needed, e.g. tracks coming from the interaction point and cosmic data recorded in the ATLAS pit. Some weak modes can be recovered using external constraints, e.g. the LHC beam position, or internal information, which potentially can constrain degrees of freedom of the system. An example of a weak mode is a global translation of the whole detector. This kind of transformation will not change track residual distributions, therefore track based alignment will not be sensitive to it. In this scenario external

constraints such as the LHC beam position or an internal reference point can be imposed, as discussed below.

2.4.2 Alignment with the CSC data

We performed studies with the simulated data set CSC7270 [61], which contains 10 muons per event coming from a common vertex discussed above in chapter 2.2.

Particle momenta were generated with a flat distributions in transverse momentum p_T and in azimuthal angle ϕ , using $p_T \in [2; 50] GeV$, $\phi \in [0; 2\pi]$, and $|\eta| < 2.5$. Error scaling was used for track reconstruction (see section 2.2.1).

The alignment strategy for the CSC data was the following: the Local χ^2 alignment with vertex constraint was performed. The TRT part of the ATLAS Inner Detector was not aligned in this procedure, i. e. hits from the TRT were removed from the tracks before the vertex reconstruction and alignment procedures. For the *level1* alignment, which will be described below, only barrel hits were used. For our studies tracks were refitted with the common vertex point before each alignment iteration. We performed *level1*, *level2* and *level3* alignment procedures for the CSC data. Different levels of the alignment minimize the residuals correcting the misalignment for the modules corresponding to the level. For example at *level1* alignment parameters for the Pixel and SCT barrel and the two SCT endcaps are updated during the alignment procedure.

Comparisons between Local χ^2 (silicon only) alignment with and without vertex constraints were performed. In order to compare the performance of the alignment procedure with perfect knowledge of the detector geometry the generated misalignment was corrected

ATLAS software packages
Athena release 12.0.6
InDetRecExample-01-03-42-05
InDetLocalChi2AlignAlgs-00-00-18
InDetLocalChi2AlignTools-00-00-35
InDetLocalChi2AlignEvent-00-00-09

Table 2.3: ATLAS software packages used for the given studies.

for.

The ATLAS software packages used are listed in table 2.3. The following sequence of actions was performed to obtain the results. The first 5 iterations were *level1* local χ^2 alignment of the Pixel and SCT barrel subdetectors. The position of the Pixel barrel was fixed at this stage. As discussed above, possible global shifts of the whole detector (weak modes) will not change the results of the track based alignment. So without loss of generality, we can choose an internal reference point and align the other parts with respect to the chosen reference module. This will not change the relative alignment between alignable modules, i. e. the SCT alignment with respect to the Pixel subdetector. On the 6th iteration we used the reconstructed primary vertex position distributions to shift the center of the ID to the corresponding beam spot position. Afterwards the *level2* and *level3* alignment procedures were performed for the SCT and Pixel subdetectors.

Residual distributions for Pixel part of the Inner Detector

The residual distributions for the Pixel barrel layers with the misalignment present in the data are shown in figure 2.5. Residual distributions for the Pixel layers before any alignment are shown in

plots a) and c). In a) all track hit residuals are shown, in c) only tracks associated to the primary vertex are shown, after re-fitting with the vertex measurements. Due to the misalignment the residual distributions for each layer are not centered at zero. The residual distributions for the Pixel layers are slightly wider when the tracks are refitted with the vertex point. Using reconstructed vertices correlates more SCT and Pixel modules per event compared to using individual tracks.

Residual distributions after the local χ^2 alignment procedure are shown in plot b) and residual distributions after the local χ^2 alignment with vertex constraint are shown in plot d). The residual distributions are centered more closely at zero and the RMS values of the distributions are smaller compared with plot a).

The different numbers of entries in plots a) and b) compared with c) and d) are due to the vertex constraint used for the alignment procedure, which takes the tracks associated with a vertex in plots c) and d) and all tracks in plots a) and b). In plot d) we see the residual distribution after the beam position constraint (see section 2.4.2) was applied. The distributions are centered more closely on zero and the RMS is slightly smaller compared with the other distributions after alignment. We find that the results after the alignment procedure are near to optimal.

Residual distributions for SCT part of the Inner Detector

The same distributions for the SCT barrel part of the detector are shown in figure 2.6. Again in plots a) and c) the residuals are calculated before the alignment procedure. In plot a) all track hits residuals are shown and in plot c) only tracks associated to the primary vertex and refitted with the vertex measurements contribute.

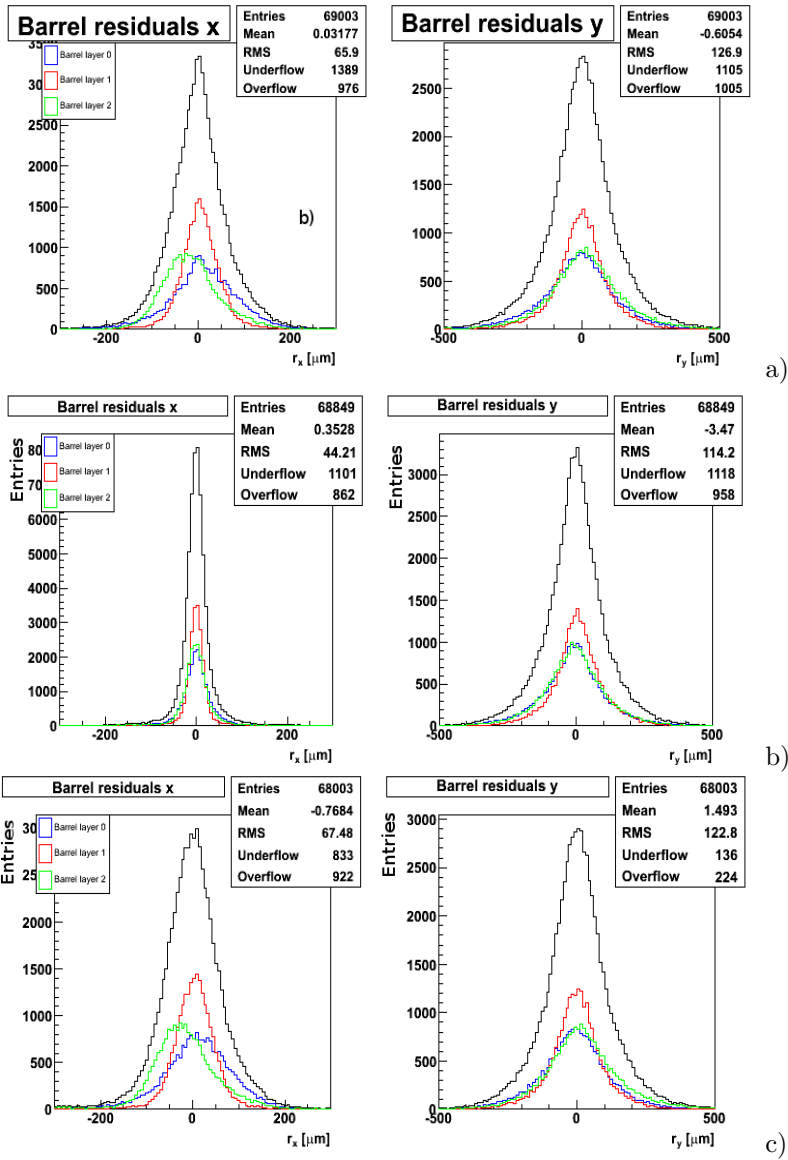
In plots b) and d) we see residual distributions after the local χ^2 alignment and after the local χ^2 alignment with vertex constraint. For both b) and d) the residual distributions are already centered at zero and the RMS values are smaller compared with plots a) and c). Plots e) show the residual distributions after the beam position constraint was applied in the alignment. The distributions are centered more closely on zero and the RMS is slightly smaller compared with the other distributions after alignment.

The alignment procedure gives more significant improvements for the x coordinate than for y . This can be explained by noting that the generated misalignment was larger for the x coordinate than for the y [62].

2.4.3 Alignment with reconstructed vertex distributions

Several control plots were produced to study the reconstruction before and after each step of the alignment procedure. Figure 2.7 shows that before alignment the reconstructed vertex distributions' (black curves) mean values are shifted from zero. After the alignment this shift is recovered. The main improvement came after the *level1* alignment procedure, where the reconstructed vertex position was used to shift the whole detector. Thus the vertex distributions were moved towards zero as well. However, after alignment the vertex distribution RMS improved as well showing that the introduced misalignment was recovered.

CSC misalignment of the detector gives the distributions of the reconstructed vertex positions significantly displaced from the nominal position corresponding to the generated beam spot, see section 2.1.1. In order to see improvements of the alignment procedure with



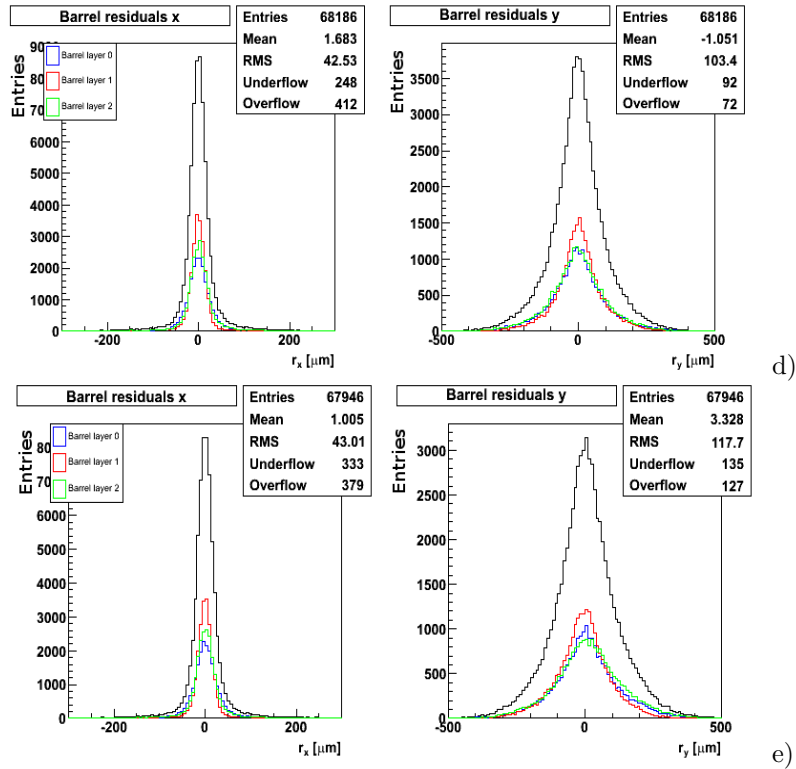
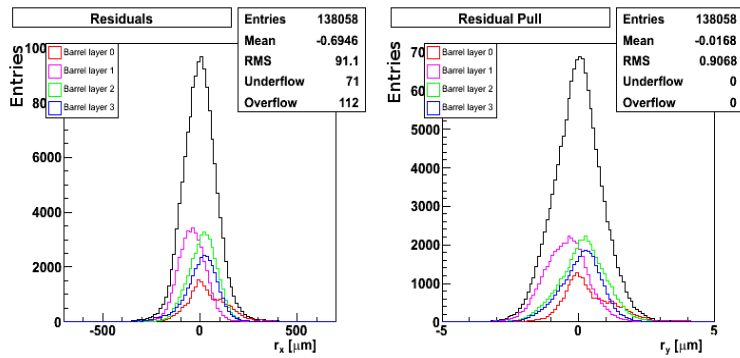
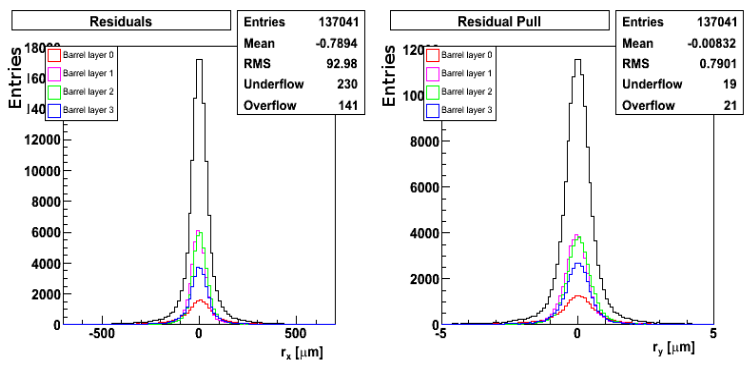


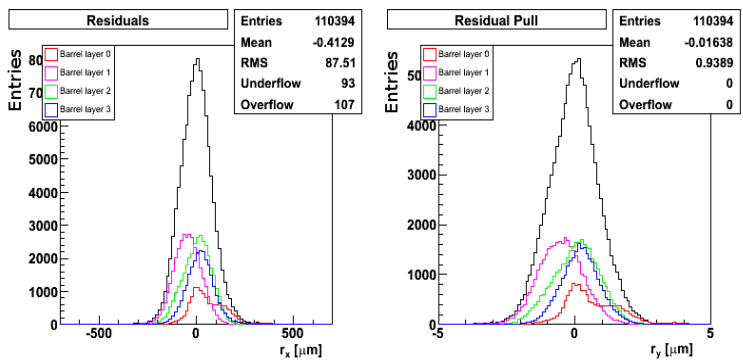
Figure 2.5: a) Pixel Barrel residuals before Alignment. b) Pixel Barrel residuals after Local χ^2 SiOnly Alignment (all 3 levels) c) Pixel Barrel residuals before Alignment with vertex constraint. d) Pixel Barrel residuals after Local χ^2 SiOnly Alignment with vertex constraint (all 3 levels). e) Pixel Barrel residuals after Local χ^2 SiOnly Alignment with vertex constraint and beam constraint.



a)



b)



c)

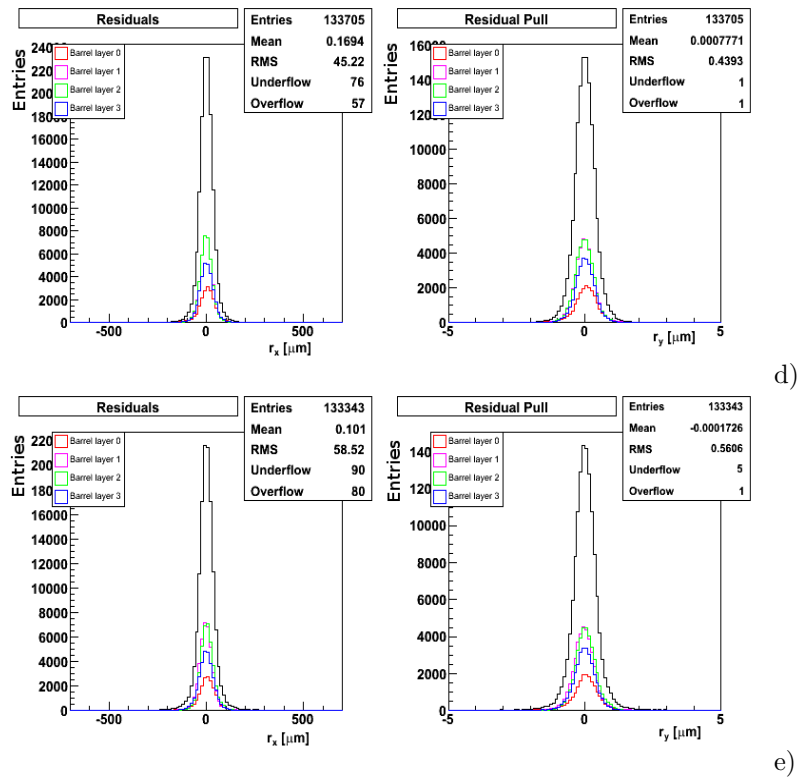


Figure 2.6: a) SCT Barrel residuals before Alignment. b) SCT Barrel residuals after Local χ^2 SiOnly Alignment (all 3 levels) c) SCT Barrel residuals before Alignment with vertex constraint. d) SCT Barrel residuals after Local χ^2 SiOnly Alignment with vertex constraint (all 3 levels). e) SCT Barrel residuals after Local χ^2 SiOnly Alignment with vertex constraint and beam constraint.

an additional precise beam spot measurement, an iterative beam position constraint for the alignment procedure was implemented. The beam position constraint implemented in `InDetPriVxFinderTool` in Athena [66] was used. The size of the beam spot can be configured for every iteration of the alignment procedure. This allows the procedure to be started using a large beam spot size (7 mm). The beam spot size is reduced after each iteration of the alignment until the generated beam spot size (0.015 mm) is reached.

The results of the reconstructed vertex distributions after alignment with beam constraints are shown in figure 2.7 (red curve). The results show that after the alignment procedure with beam constraint the vertex position distributions are near to the generated spread of the beam spot for the X and Y coordinates. In table 2.4 are shown the mean and RMS of the vertex distributions for the initial geometry, after alignment procedure and after alignment plus beam constraint. For comparison the size of the generated vertex spread is also shown. The RMS values of the vertex distributions in the X and Y coordinates after the alignment procedure are still one order higher than the generated vertex spread and the improvement was obtained only after beam constraint was applied. The distribution for the vertex position Z coordinate is unchanged. The external measurements of the beam spot by the LHC machine are less sensitive to the Z direction and there is no corresponding beam constraint for this coordinate.

2.4.4 Track parameters before and after vertex refit

The main functionality of the vertex constraint tool is to improve the track fit by adding the common event vertex to the track. Then the

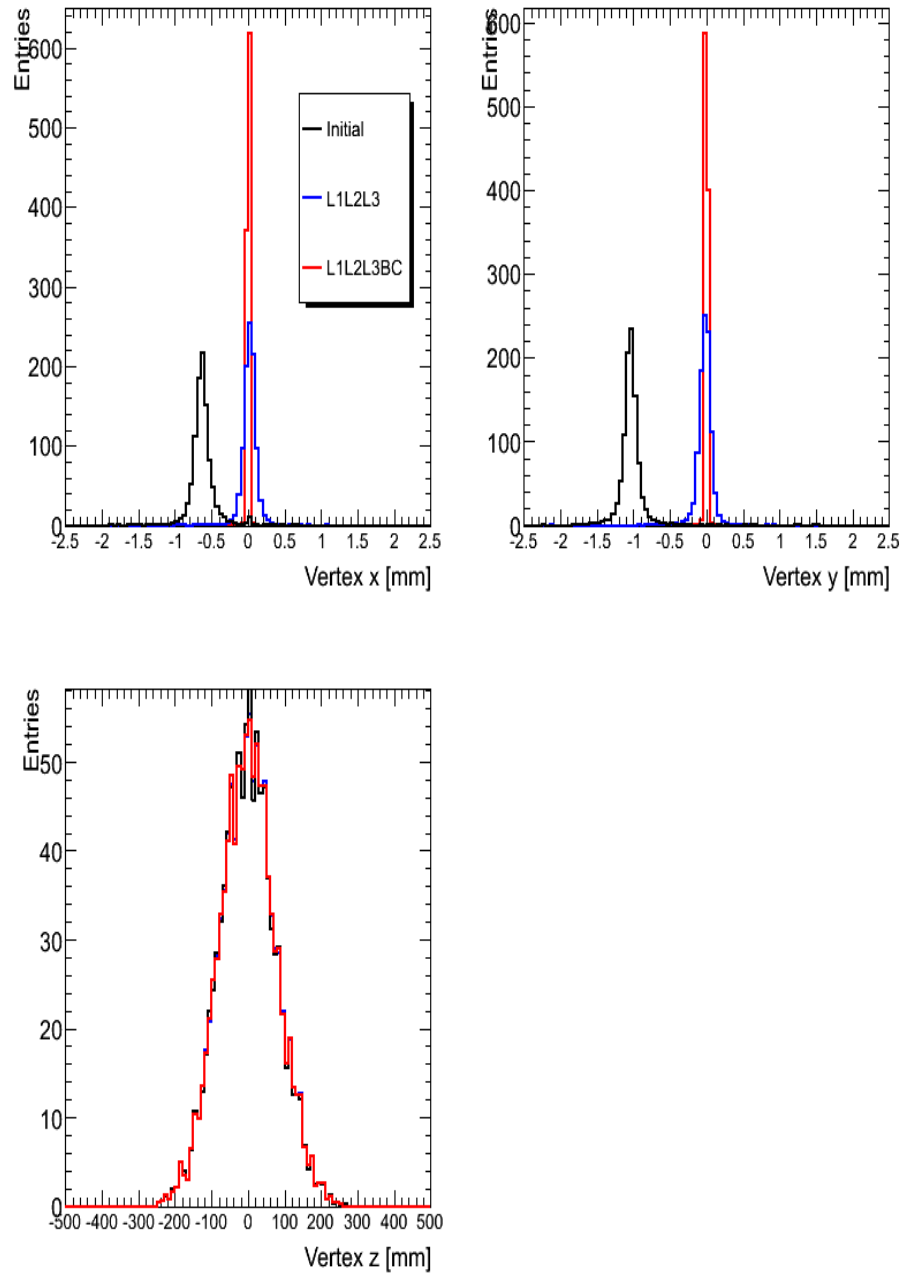


Figure 2.7: Vertex position distributions for the CSC data before the alignment (black), after the *level1*, *level2* and the *level3* alignment (blue), and after alignment with the iterative beam constraint (red). Coordinate axes (X, Y, Z) denote the global frame of the ATLAS detector.

Geometry	Vertex distributions mean			Vertex distributions RMS		
	x [mm]	y [mm]	z [mm]	x [mm]	y [mm]	z [mm]
Generated vertex distributions	0	0	0	0.015	0.015	0.015
CSC misaligned geometry	-0.6157	-1.024	0.7673	0.2162	0.2296	77.55
L1L2L3 alignment	0.0249	-0.0231	0.0504	0.1485	0.1502	77.58
L1L2L3 alignment plus beam constraint	0.0027	-0.0026	0.0559	0.0203	0.0209	77.58

Table 2.4: The vertex distribution mean and RMS values for the generated vertex spread, for the initial CSC misalignment geometry, results after alignment and after alignment with beam constraint.

tracks are refitted and improved tracking errors for the innermost pixel layer are expected. In figure 2.8 the distributions for the track perigee parameters at the nominal interaction point are presented, before and after the alignment. The distributions are slightly different. Only improvement of the track d_0 distributions is observed, as *level1* misalignment (global shifts of the detector) was corrected. For comparison the track parameter error distributions at the nominal interaction point and at the vertex point are shown in figure 2.9. The tracking error is better at the vertex point (red curve) than at the nominal interaction point (black curve). Since several tracks are associated with a vertex the position measurement is improved at that point. In figure 2.8 the track transverse momentum distributions are shown. The plot shows that misalignment effects were not recovered completely. The distribution after alignment is better than the initial distribution for the misaligned geometry, but still is far from the distribution which one obtains with perfect knowledge of the detector alignment.

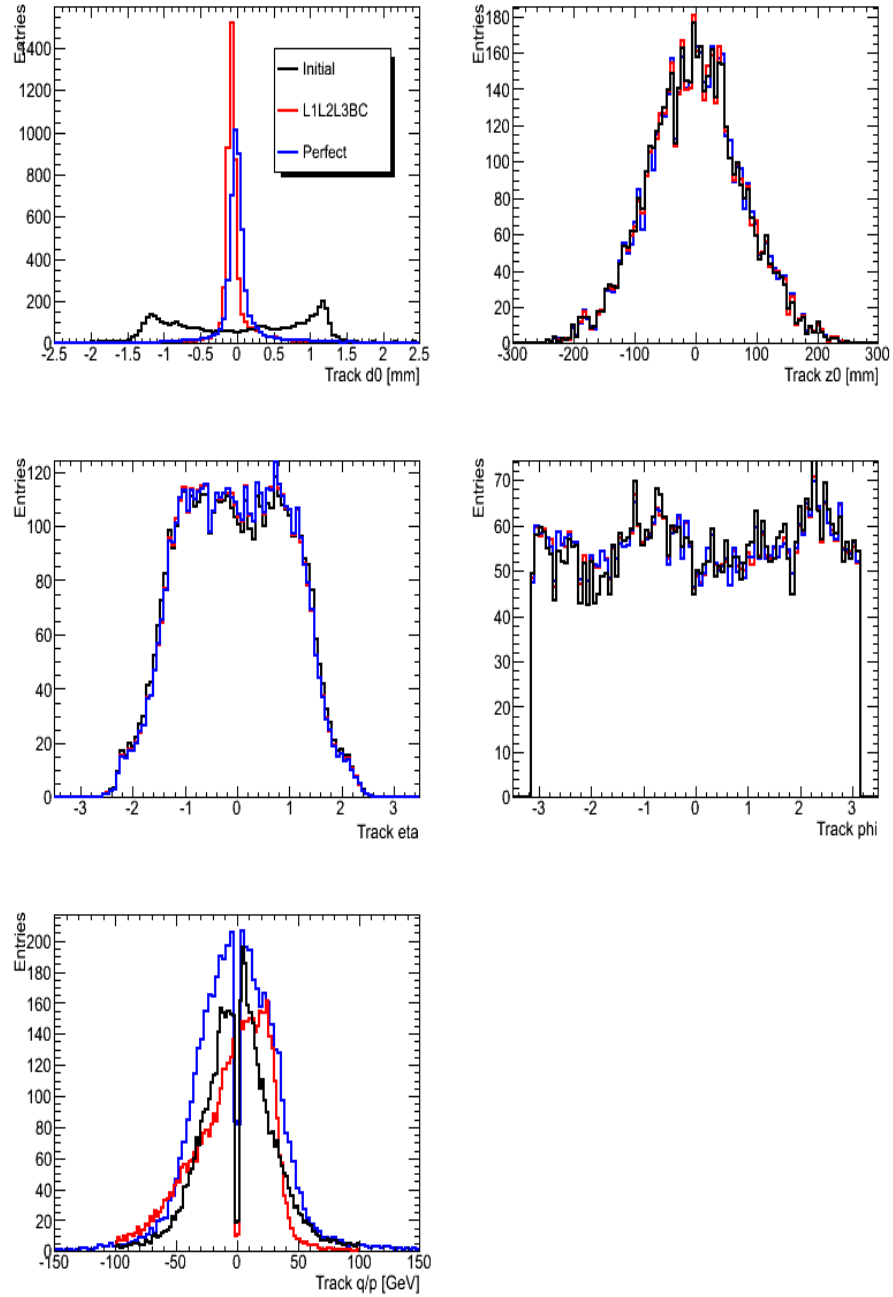


Figure 2.8: Track perigee parameters for CSC data before alignment (black), after *level1*, *level2*, *level3* alignment with BC (red) and for perfect alignment are shown in blue.

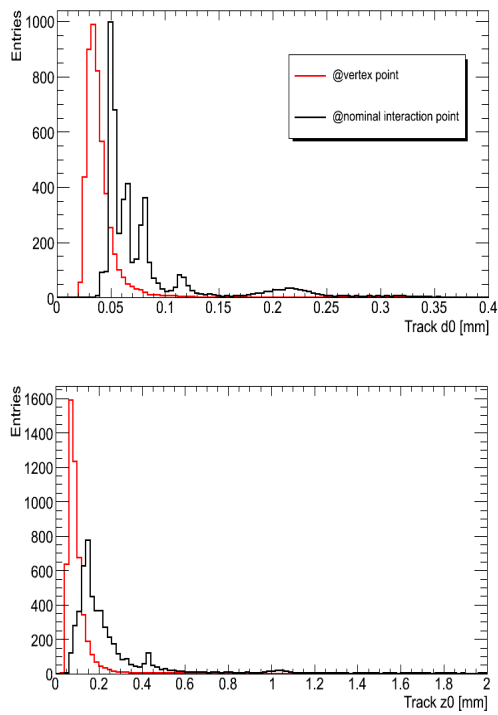


Figure 2.9: Track perigee parameter error distributions at the nominal interaction point (black), and at the vertex point (red).

2.5 Conclusions

Local χ^2 alignment was performed for the SCT and Pixel subdetectors for the CSC generated misalignment. A new constraint for the track based alignment procedure was introduced. The interaction vertex point was added to the track fit to combine the information from the detector measurements with the accumulated information from the reconstructed vertices. Refined tracks were used for the track based alignment procedure and improved results were obtained. The tool which performs the refit of tracks with vertex point is implemented in Athena and can be used as pre-processing tool for any track based algorithm.

Chapter 3

Heavy flavor tagging with ATLAS

Final states of the majority of LHC physics processes involve jets of hadrons. Jets are formed when the final state partons hadronise and form color singlet bound states which may subsequently decay into long lived charged and neutral particles. Charged particles leave tracks in the inner detector and all particles deposit energy in the calorimeter system. The definition and the measurement of jets depends on the procedure used to collect the deposited energy in the detector.

Identification of jets which originate from a b quark (b-tagging) is important for a large part of the ATLAS physics program such as precise measurements of the top quark sector and searches for physics beyond the Standard Model. We studied the performance of the existing b-tagging algorithms in ATLAS using Monte Carlo simulated events. The aim of the studies was to investigate the b-tagging performance in the case of systematic and random misalignment of the ID. The performance variation due to the underlying

jet reconstruction algorithm used and the corresponding calibration scenarios for the b-tagging procedure were also investigated.

3.1 Jet reconstruction algorithms

The ATLAS calorimeters have fine granularity in $\phi - \eta$ space over $|\eta| \leq 3.2$ (details can be seen in chapter 1.5.4), while the forward calorimeters cover the region up to $|\eta| \leq 4.9$ and provide sufficient granularity to reconstruct jets with small polar angles. Jet reconstruction algorithms combine calorimeter objects based on their space location (fixed cone algorithms) or space and momentum proximity criteria (k_T algorithms). Two kinds of calorimeter objects (see below) are used as input for the jet reconstruction algorithms: towers or topological clusters. Calorimeter towers are formed by collecting the cell energies based on their location and summing their signals. Topological clusters are formed iteratively around seed cells with energy above a given threshold considering the noise and the pile-up contributions for each calorimeter region.

Cone algorithms combine calorimeter objects within a cone of fixed size around the stable jet axis. Typical cone sizes in ATLAS are narrow cone with size $\Delta R = \sqrt{\Delta\eta^2 + \Delta\phi^2} = 0.4$ and wide cone with size $\Delta R = 0.7$. In order to find the stable cone position, a p_T -weighted centroid for the input objects is found within the cone. If the centroid and the cone axis do not coincide then the cone is moved to the position given by the p_T -weighted centroid. The procedure is repeated until a stable cone is found. In the seeded cone algorithms a pre-clustering procedure defines regions of the detector where substantial energy is collected and these regions are used as starting points (seeds) for the jet finding procedure. A transverse

energy threshold for a seed of $E_T = 1$ GeV for all cone jets used in ATLAS. When two stable cones overlap they are merged if 50% of the less energetic jet overlaps with the more energetic jet. If the overlap is less than 50%, the shared objects are assigned to the nearest jet.

k_T algorithms were originally used at electron-positron collider experiments [67]. The clustering process of the k_T algorithm initially considers each calorimeter object as a proto-jet. The following quantities are computed for each proto-jet i and each pair of proto-jets i, j , respectively:

$$k_{T,i}^2 = p_{T,i}^2, \quad k_{T,(i,j)}^2 = \min(p_{T,i}^2, p_{T,j}^2) \frac{\Delta R_{i,j}^2}{D^2} \quad (3.1)$$

$p_{T,i}$ is the transverse momentum of the i^{th} proto-jet and $\Delta R_{i,j}$ is the distance in (η, ϕ) space $\Delta R_{i,j} = \sqrt{(\eta_i - \eta_j)^2 + (\phi_i - \phi_j)^2}$ between each pair of proto-jets. D is the parameter that controls the size of the jet (analogous to the cone size R). If the smallest of the above quantities is a $k_{T,i}^2$, then that proto-jet becomes a jet and is removed from the proto-jet list. If the smallest quantity is a $k_{T,(i,j)}^2$, then the two proto-jets (i, j) are merged into a single proto-jet by adding their four-vectors, and the two original entries in the proto-jet list are replaced by this merged entry. This process is iterated with the corrected proto-jet list until all the proto-jets have become jets, i. e. at the last step the $k_{T,(i,j)}^2$ for all pairs of proto-jets are larger than all $k_{T,i}^2$ for the proto-jets individually.

The anti- k_T jet reconstruction algorithm was introduced recently [68]. It is similar to the k_T algorithm, except that the distance measures are now defined as:

$$k_{T,i}^2 = 1/p_{T,i}^2, \quad k_{T,(i,j)}^2 = \min(1/p_{T,i}^2, 1/p_{T,j}^2) \Delta R_{i,j}^2 / D^2. \quad (3.2)$$

In this case soft proto jets are merged first. This algorithm is attrac-

tive in terms of jet shape, which is conical in η, ϕ space, and thus easier to handle for calibration schemes.

3.1.1 Heavy flavor tagging algorithms

Jets originating from b quarks (b-jets) can be identified by exploiting the relatively high mass and long lifetime of the final state B-hadrons. The average lifetime of B hadrons ($B^\pm, B_0, B_S, \Lambda_b$) multiplied by the speed of light gives a length of the order 400-500 μm and for highly energetic B hadrons ($E = 50 \text{ GeV}$) this leads to a flight length of a few millimeters. Therefore B hadron decay particle tracks are not expected to be compatible with the primary vertex and this is used to distinguish b-jets from jets originating from light quarks.

In ATLAS jets are measured using the calorimeter objects. For the b-tagging the tracks measured in the ID must be associated with the jets and therefore only the jet direction is relevant from the calorimeter jet measurements. The jet direction is used to define which tracks should be associated with the jets. Currently at ATLAS tracks within a distance $\Delta R < 0.4$ around of the jet axis are associated with the jet.

There are several b-tagging algorithms implemented in the ATLAS software. In table 3.1 the b-tagging algorithms used within ATLAS are listed. The so-called spatial tagging algorithms are based on identifying of decays of B-hadrons within the jets. One method looks at track impact parameters with respect to the primary vertex, which will on average be larger for tracks coming from B-hadron decays those for primary tracks. A second method is the explicit reconstruction of the secondary vertex and the determination of the

decay length significance. As the third method semi-leptonic decays of B-hadrons can be used by identifying a lepton in or near the jet to tag heavy flavor jets. The spatial tagging algorithms based on track impact parameters and/or secondary vertices measurements, will be considered in this thesis.

The transverse impact parameter, d_0 , is the distance of closest approach of the track to the primary vertex point in the $(r - \phi)$ projection. The longitudinal impact parameter, z_0 , is the z coordinate of the track at the point of closest approach in $(r - \phi)$. The track significance is signed positively if the track crosses the jet axis in front of the primary vertex and negatively otherwise.

Since the resolution in the (x-y) plane is an order of magnitude better than compared to the resolution in the z direction, track impact parameters may be measured in the transverse plane only (d_0) although one could obtain more information from including the longitudinal impact parameter z_0 . For the impact parameter based b-tagging algorithms the track significance is calculated for each track by taking the ratio of the track transverse impact parameter, d_0 , and the error on the measurement $\sigma(d_0)$. The simplest tagging algorithm consists of counting tracks with either large impact parameter or impact parameter significance. In figure 3.1 are shown signed transverse impact parameter and signed transverse impact parameter significance distributions for b, c- and light jets.

A further increase of the discrimination between b-jets and light jets can be achieved by reconstructing the inclusive vertex formed by the decay products of the B-hadron, including the products of a possible subsequent charm hadron decay. Three additional vertex properties are used in the likelihood approach described below: i) the invariant mass of all tracks associated with the vertex, ii) the

ratio of the sum of the energies of the tracks coming from the secondary decay vertex to the sum of the energies of all tracks in the jet and iii) the number of two-track vertices within the jet. In figure 3.2 are shown secondary vertex variables for b- and light jets.

The advanced b-tagging algorithms use a likelihood ratio approach: the measured values of a discriminating variable are compared to previously determined smoothed and normalized distributions for both the b- and light jet hypotheses and two- and three-

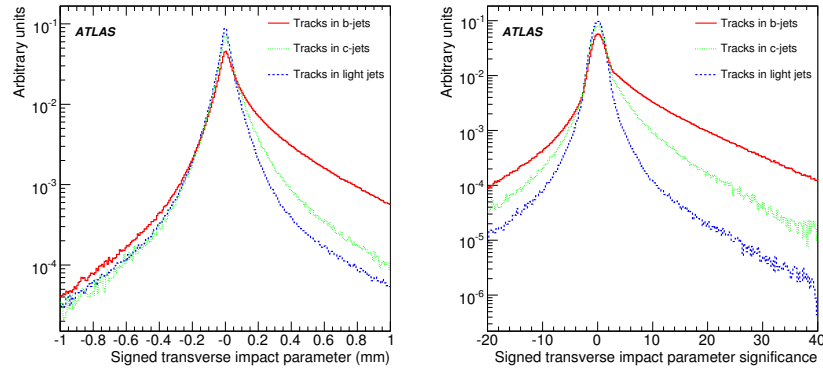


Figure 3.1: Signed transverse impact parameter d_0 distributions (left) and signed transverse impact parameter significance d_0/σ_{d_0} distributions (right) for b-jets, c-jets and light jets [69].

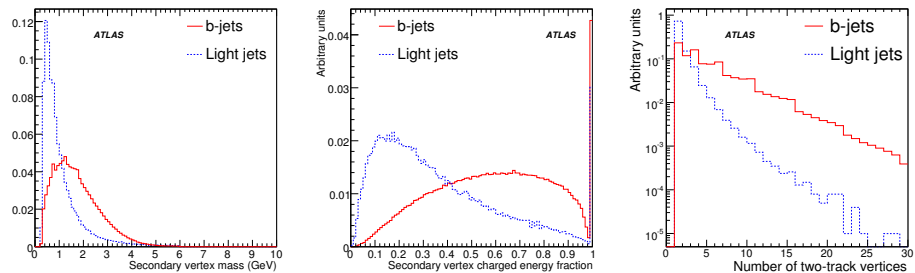


Figure 3.2: Secondary vertex variables: invariant mass of all tracks in vertex (left), energy fraction vertex per jet (center) and number of two-track vertices (right) for b-jets and light jets [69].

dimensional probability density functions (pdfs) are computed. The ratio of the probabilities for the b and light jet hypotheses defines the track or vertex weight, which can be combined into a jet weight as the sum of the logarithms of the individual track and/or vertex weights [69]. In the most advanced algorithm the resulting b-tagging weight of the secondary vertex based algorithm is combined with the weight of the impact parameter based approach. In figure 3.3 the jet b-tagging weight distributions for b-jets, c-jets and light jets are shown. The left plot is for the impact parameter based tagging algorithm (IP2D) and the right plot corresponds to the combined tagging algorithm (IP3D+SV1).

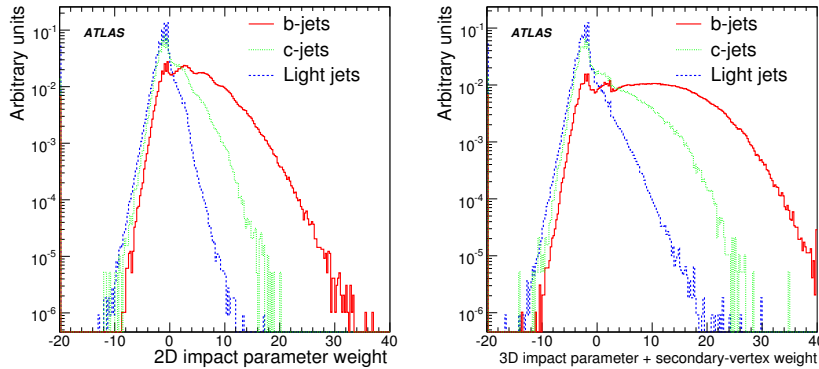


Figure 3.3: Jet b-tagging weight distribution for b-jets, c-jets and light jets. The left plot is for the IP2D tagging algorithm. The right plot corresponds to the IP3D+SV1 tagging algorithm [69].

To select b-jets, a cut value on jet weight is chosen using the pdf distributions, corresponding to a given efficiency. The relation between the cut value and the efficiency depends on the jet transverse momentum and rapidity.

Impact parameter based	
IP1D	Combining track longitudinal impact parameters.
IP2D	Combining track transverse impact parameters.
IP3D	Combining longitudinal vs transverse impact parameters.
Counting	Counting of tracks with large impact parameter.
JetProb	Comparing track transverse impact parameters to the resolution function for prompt tracks.
Secondary vertex based	
SV0	Finding secondary vertex within jet.
SV1	The invariant mass of all tracks, the ratio of the sum of the energies of the tracks at the vertex to the sum of all tracks at jet (2D histogram) and the number of two-track vertices (1D histogram).
SV2	3D histogram of all three secondary vertex variables.
JetFitter	Exploits the topological structure of weak b- and c-hadron decays inside the jet.
Combined IP3D+SV1 algorithm	The weights of the individual tagging algorithms are summed up.
Soft lepton algorithms	Relies on the semi-leptonic decays of b and c hadrons.

Table 3.1: b-tagging algorithms at ATLAS [70].

3.2 Calibration of the tagging procedure

The likelihood-based tagging algorithms use the probability density functions for discriminating variables for the b- and light jet hypotheses. The determination of the pdfs is called calibration of the tagging algorithm. Initially pdfs are produced using the Monte Carlo simulated data sets containing b-jets and light jets. During the running of the ATLAS experiment reference histograms for heavy quark and light jets will be obtained using selected data samples with high fractions of heavy or light jets, e.g. $t\bar{t}$ events or di-jet events [69].

3.3 Performance studies

The performance of the b-tagging procedure can be evaluated by looking at the fraction of misidentified light jets for a fixed b-jet selection efficiency. The fixed b-jet efficiency is estimated using the calibration histograms for b-jets. The light jet rejection rate (R_l) is used for the measurement of light jet misidentification as heavy jet. The variable R_l is defined as the inverse of the light jet selection efficiency when b-jet selection criteria are applied. For the performance studies only jets fulfilling $p_T > 15$ GeV and $|\eta| < 2.5$ are considered, except when stated otherwise. There was no attempt to remove the jets which are composed only of electrons from the reconstructed jet collection. We investigated the b-tagging performance for different detector geometries to study systematic detector misalignment effects. We also investigated the performance for different jet reconstruction algorithms and track-to-jet association procedures. Finally we studied the dependence of the b-tagging performance on various calibration scenarios.

3.4 Data samples and detector geometry

The data samples we used for the b-tagging performance studies were $t\bar{t}$ pair production samples from the central ATLAS simulated data production commonly used by many groups. The $t\bar{t}$ signal samples were generated using the MC@NLO [71] next-to-leading order (NLO) Monte Carlo generator combined with HERWIG parton shower and hadronisation [72]. The ATLAS detector was fully simulated using the Geant4 ([73], [74]) program. For the NLO cross section estimates the CTEQ6M set of parton density functions (PDF) was used [38] [75].

For the alignment and calibration studies different detector descriptions were tested. In the detector simulations the misalignment of the inner detector components and distorted magnetic field were introduced as it was described in chapter 2.2. If not stated otherwise we use the knowledge of the detector misalignment introduced during the simulation for the event reconstruction and analysis procedure and in this case we have perfect alignment of the detector.

3.4.1 Performance with various inner detector misalignment scenarios

The spatial b-tagging procedure is based on identification of secondary decays within the jet by looking at track parameter distributions and secondary vertices. Therefore the performance of tracking sub-detectors is important. The tracking sub-detectors alignment precision requirements are derived from physics motivations and one of them is good performance of b-tagging algorithms [2].

We studied the primary vertex reconstruction depending on the alignment quality in chapter 2.4.3. In this chapter we will have a

look at the b-tagging performance in the case of systematic distortions of the ID. The global systematic misalignments are rotations or translations of the large structures of the ID. Most of them will cause changes in track reconstruction and therefore the track based alignment procedure can recover them. However, there can be some systematic misalignments which conserve the given track residual distributions and therefore cannot be recovered by the χ^2 minimization alignment procedure. These distortions are called weak modes of the χ^2 alignment procedure. The ATLAS ID alignment group created systematic misalignments of the ID. In figure 3.4 the schematic view of a possible weak modes considered within ATLAS is shown.

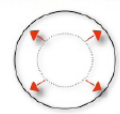
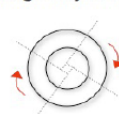

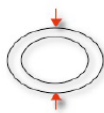
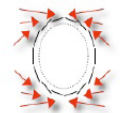
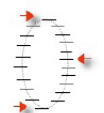

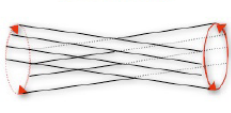
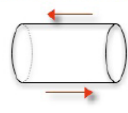
	ΔR	$\Delta\phi$	ΔZ
R	Radial Expansion (distance scale) 	Curl (Charge asymmetry) 	Telescope (CM boost) 
ϕ	Elliptical (vertex mass) 	Clamshell (vertex displacement) 	Skew (Z momentum) 
Z	Bowing (total momentum) 	Twist (vertexing) 	Z expansion (distance scale) 

Figure 3.4: The possible global distortions of the ID [76], [77]. “Weak modes” depicted in red were investigated by the ATLAS ID alignment group and within this thesis.

We tested the b-tagging performance for the curl, twist, ellip-

Geometry	Parametrisations	Max. outer SCT module shift
Curl	$\Delta\phi = c_1 R + \frac{c_2}{R}$	250 μm
Twist	$\Delta\phi = cZ$	100 μm
Elliptical	$\Delta R = \frac{1}{2} c \cos(2\phi) R$	250 μm
Elliptical big	$\Delta R = \frac{1}{2} c \cos(2\phi) R$	1000 μm
Telescope	$\Delta Z = cR$	500 μm
Telescope big	$\Delta Z = cR$	3000 μm

Table 3.2: Summary of the residual systematic misalignment sets used for the b-tagging performance studies.

tical and telescope distortions shown in red frames in figure 3.4. For comparison the b-tagging in the case of random misalignment of the inner detector modules was also examined. The inner detector alignment group produced a geometry setting corresponding to the “Day 1” expectation of the alignment precision. It is based on a direct survey of the detector and the results from the alignment procedure with cosmic rays taken in 2008 during the detector operation [78]. There is also an estimate of the precision of the detector alignment after the track based alignment is performed with sufficient collision data, the so-called “Day 100” geometry [79]. For the “Day 1” the individual pixel modules were shifted randomly by a Gaussian distributions with σ_x and $\sigma_y = 20-50 \mu m$ (barrel-endcaps) for the Pixel/SCT subdetectors. For the “Day 100” the individual pixel modules were shifted randomly by a Gaussian distributions with σ_x and $\sigma_y = 10 \mu m$ for the Pixel and SCT subdetectors. Shifts along the z direction and rotations of the modules were not introduced. In table 3.2 the order of the residual systematic misalignment used for the b-tagging studies are shown.

For our studies we had to reconstruct events with different detector geometries. For the systematic misalignment studies additional

distortions were applied to the perfect knowledge of the detector alignment. The order and parameterization of the systematic distortions are described in [80].

The b-tagging procedure was run after the data samples were reconstructed with various detector geometries and the performance was measured. In figure 3.5 the light jet rejection rates (R_l) for the various geometries are shown for 50% b-tagging efficiency in all cases. It can be seen that the performance is slightly degraded in the cases of the twist, elliptical and telescope distortions. In the case of curl misalignment the performance drops by a factor of two. The significant degradation of the performance was expected from the parameterization of the curl distortions, which give significant shifts of $O(50\mu\text{m})$ for the innermost Pixel layer modules. The given curl distortions are not completely weak modes and therefore the alignment procedure could partially recover the distortions. After the alignment of the curl distortions the improved performance of the b-tagging procedure is also shown in figure 3.5 (Align/Curl).

The size of the distortions for the other systematic misalignments is negligible for the innermost layer and therefore the b-tagging performance is rather stable. In order to check when the effect becomes more significant the size of the misalignment was increased for the outermost SCT layer up to 2 mm in the case of elliptical distortions and 3 mm for the telescope. The corresponding results are also shown in figure 3.5 and show that even in this case b-tagging is rather stable if the positions of the innermost layer modules are known with good precision.

The random statistical misalignment “Day 1” geometry gives results worse than the systematic misalignment scenarios. However it can be also recovered by the alignment procedure as shown in the

last bin for “Day 100” geometry in figure 3.5.

For our studies we also produced b-tagging calibration files (pdfs) with systematic distortions and re-run the b-tagging procedure. The corresponding results for the elliptical distortions are shown in figure 3.5 (Ell/Calib). The performance is slightly better in the case of elliptical distortions when calibration is done with the same geometry compared to the calibration with perfect geometry. This is shown in bin 5 (Elliptical) and bin 7 figure of 3.5 (Ellipt.big). The elliptical distortion (bin 5) gives slightly better performance for the light jet rejection rate than perfect alignment (bin 1). This can happen when the calibration files for the b-tagging procedure are produced for the perfect alignment and used for a distorted geometry. The light jet rejection rate for the elliptical distortion is almost the same as for the perfect alignment if the calibration files are produced also for the elliptical distortions.

As discussed above, the rejection rate drops by a factor of two for the curl misalignment. We studied which part of the b-tagging procedure was affected most. In figure 3.6 the primary vertex distribution x and y coordinates and in figure 3.7 the track impact parameter distributions are shown for perfect and curl geometry. The distributions are not shifted, but the RMS is wider for curl compared to the perfect geometry. These variables are used by spatial b-tagging algorithms to estimate the weighting factor for each jet. The jet weight factors are used for the b-jet selection. In figure 3.8 the b-tagging weight cut vs corresponding b-jet selection efficiencies for curl and perfect geometries are shown. The weight cut is estimated by looking at b-jet weight distributions and finding the selection point which gives the desired b-tagging efficiency. A slight difference of selection efficiencies will be observed if the weight cut

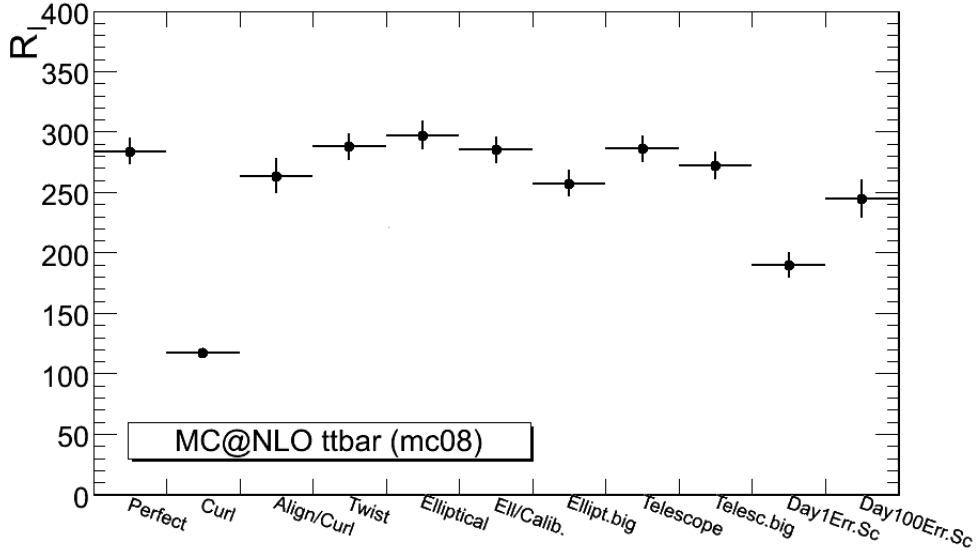


Figure 3.5: Light jet rejection rates for 50% b-tagging efficiency for various detector geometries. The first bin was produced for the perfect knowledge of the geometry, the second for the curl systematic misalignment, the third shows the curl misalignment after the alignment procedure, the fourth shows the twist distortions, the fifth shows the elliptical distortions, the sixth bin gives the result of b-tagging performance for the elliptical distortion with corresponding calibration, the seventh bin shows an elliptical distortion with larger distortions (max. 2 mm), and the eighth bin shows the results for the telescope misalignment and ninth bin corresponds to the telescope with larger distortions (max. 3 mm). The last two bins show the b-tagging performance in case of random misalignment of ID modules. “Day 1” corresponds to an estimate of initial misalignment of the ID, and “Day 100” geometry is an estimate of the precision after 100 days of running of the detector and aligning it with accumulated data. For the random misalignment studies corresponding error scaling was applied for the track reconstruction.

for the b-tagging procedure which is obtained from one geometry setting is applied to the misaligned detector measurements.

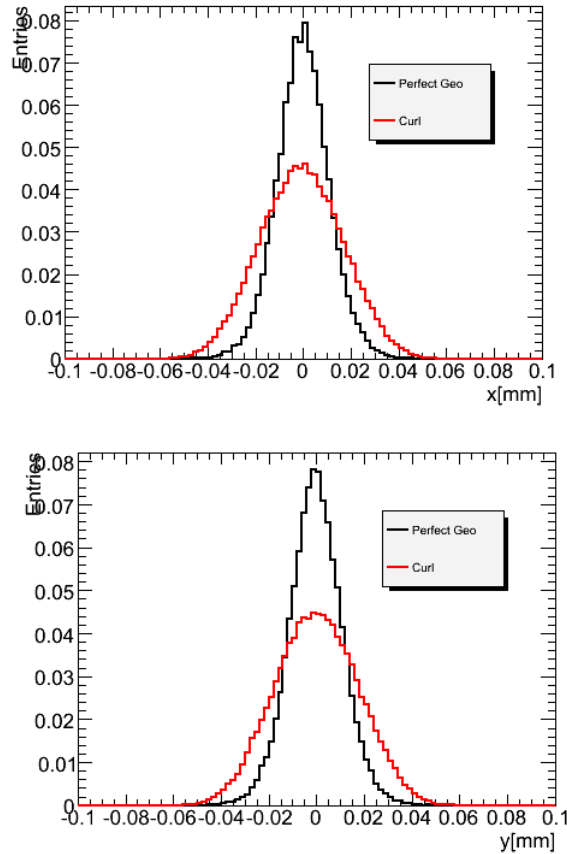


Figure 3.6: Primary vertex x and y distributions for perfect and curl geometries.

3.4.2 Performance with different jet reconstruction algorithms

The seeded fixed cone algorithm is commonly used within the ATLAS physics and performance groups. Jets are reconstructed with calorimeter towers or topo clusters with cone size $\Delta R = 0.4$. We considered two jet energy calibration scenarios: i) the cells were calibrated using the H1 method [2] and ii) topological clusters with local hadron

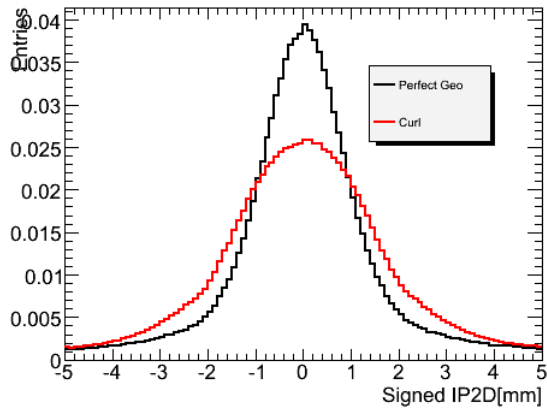


Figure 3.7: Track impact parameter distributions for perfect and curl geometries.

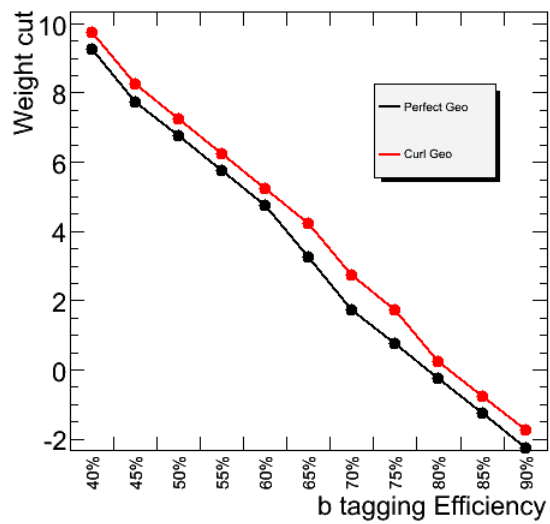


Figure 3.8: The b-tagging efficiency values vs corresponding weight cut for curl and perfect geometries.

calibration. The details of the procedure can be found elsewhere [2]. The geometrical size of the jet depends on the event topology and the transverse momenta of the hadrons. We studied the b-tagging performance for various jet reconstruction algorithms, and also varied the parameters for the jet reconstruction procedure.

The results of these studies are shown in figure 3.9. We compare the R_l for cone $\Delta R = 0.4$ (bin 1) and 0.7 (bin 3) and k_T $D = 0.4$ (bin 6) and 0.7 (bin 11) jet reconstruction algorithms. We also used different calorimeter objects as input for the jet reconstruction: bin 1 and bin 2 correspond to the calorimeter tower and topo clusters used for the Cone $\Delta R = 0.4$ jet reconstruction algorithm. The b-tagging performance strongly drops when the cone size of the jet reconstruction is increased from cone size $\Delta R = 0.4$ to 0.7 and for k_T jets from $D=0.4$ to 0.7 . The performance depends slightly on the input calorimeter objects for the jet reconstruction and gives better results in the case of the calorimeter towers (bin 1 compared to bin 2). The performance for the k_T ($D=0.4$) jet reconstruction algorithm is slightly better than for Cone $\Delta R = 0.4$ algorithm (bin 6 compared to bin 2). Comparing the last 5 bins in figure 3.9 we see how the performance drops continuously when the geometrical size of the jets is increased from 0.4 to 0.7 .

We obtain almost the same results for the corresponding k_T jets with H1 calibration and with local calibrations (bin 6 and bin 8). Thus the b-tagging performance does not depend much on the jet energy calibration scenario.

The tagging performance for jets reconstructed with the anti- k_T algorithm was also studied. In figure 3.10 we show the rejection rates, R_l for different jet reconstruction algorithms and fixed geometrical size $\Delta R = 0.4$. Comparing bin 1 and bin 2 the performance

is 60% better for anti- k_T jets. The properties of the jets were investigated more closely to find out the reason of increased R_l of the jets reconstructed with anti- k_T algorithm for the same data set and for the same tagging procedure. In figure 3.11 the jet transverse energy distributions for the cone and anti- k_T algorithms are shown. One sees the increased number of low energy jets in the same event samples when the anti- k_T jet reconstruction algorithm is used. The track multiplicities for the cone and anti- k_T jets are shown in figure 3.12. A significant number of jets have fewer than 2 tracks associated with them and the number of jets which has no associated tracks is significantly higher for the anti- k_T algorithm. The heavy flavor tagging procedures use the jets with no tracks for the tagging performance estimation and they reject these jets. Therefore the performance of the tagging procedure is increased for the anti- k_T jet reconstruction algorithm.

We introduced the requirement in the b-tagging procedure, that the jets must have at least two associated tracks. This requirement made the procedure more robust with respect to the different jet reconstruction algorithms, and the performance numbers for the different jet algorithms are closer to each other as shown in figure 3.13 bin 1 and bin 2 for the cone and anti- k_T jet algorithms.

Another possibility to reject the low energy jets with low track multiplicity would be to increase the jet transverse energy requirement from the default value of 15 GeV. We increased the jet transverse energy requirement to 30 GeV and studied the performances for several jet reconstruction algorithms. The last two bins in figure 3.13 show that the performance for the different jet algorithms is still significantly different. Thus not only low energetic jets contribute to the jet sample with no associated tracks.

The dependence of the light jet rejection rates on the jet transverse energy is shown in figure 3.14. One finds higher rejection rates for lower energy jets. At high energies light jet rejection rates drop as the jets are more collinear and thus spatial b-tagging procedures perform less well.

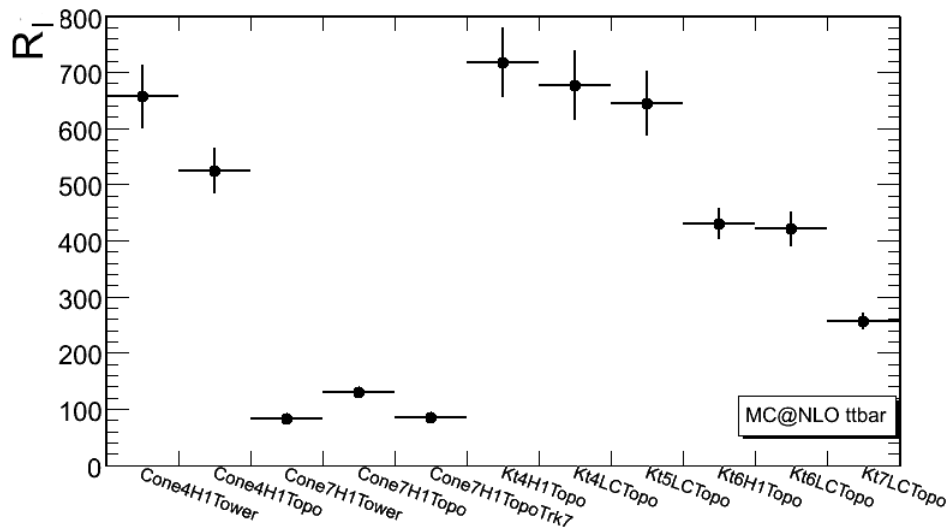


Figure 3.9: Light jet rejection rates for 50% b-tagging efficiency for various jet reconstruction algorithms, for different input reconstruction objects (Tower and Topological clusters) and for different energy calibration scenarios (H1 and local hadron calibration,) see text for details.

3.4.3 Track to jet association studies

Currently tracks are associated with jets within a fixed cone $\Delta R = 0.4$ in ATLAS. A given track is associated only once with the jet closest in ΔR . This is the case for any jet regardless of the cone size or reconstruction algorithm of the jet. In the k_T reconstruction algorithms calorimeter objects are clustered according to the space and momentum proximity and the resulting jets are not necessarily

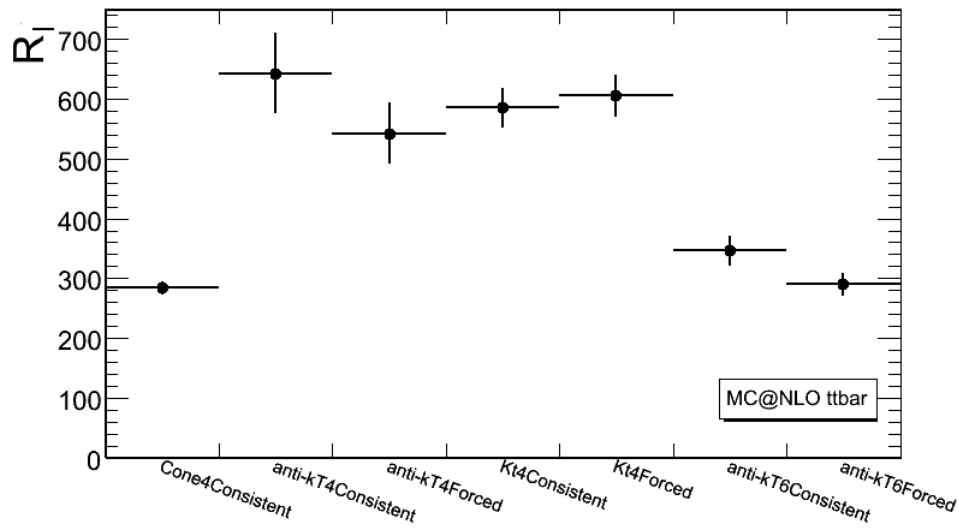


Figure 3.10: Light jet rejection rates for 50% b-tagging efficiency for various jet reconstruction algorithms, and different calibration settings for the b-tagging procedure. "Consistent" indicates that calibration procedure was done for the corresponding jet collection and consistently used for the given set, and "forced" shows results when the calibration files were derived for Cone $\Delta R < 0.4$ jets and were used for other jet collections. The first bin error is smaller than measurement point and is not well visible.

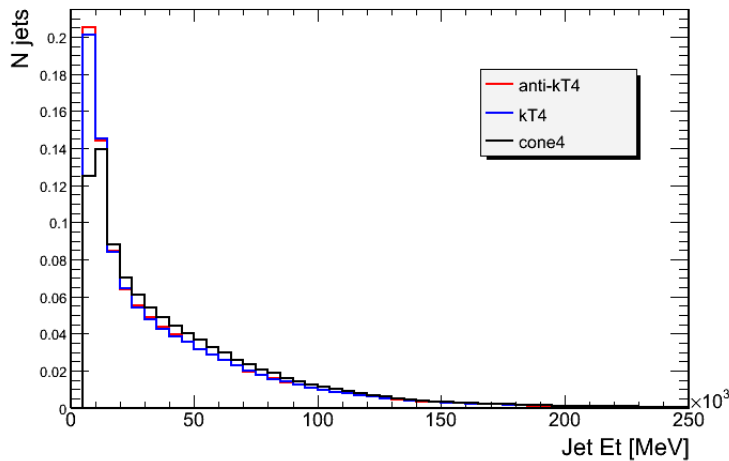


Figure 3.11: Jet transverse energy distributions for the Cone4, k_T4 anti- k_T4 jet reconstruction algorithms.

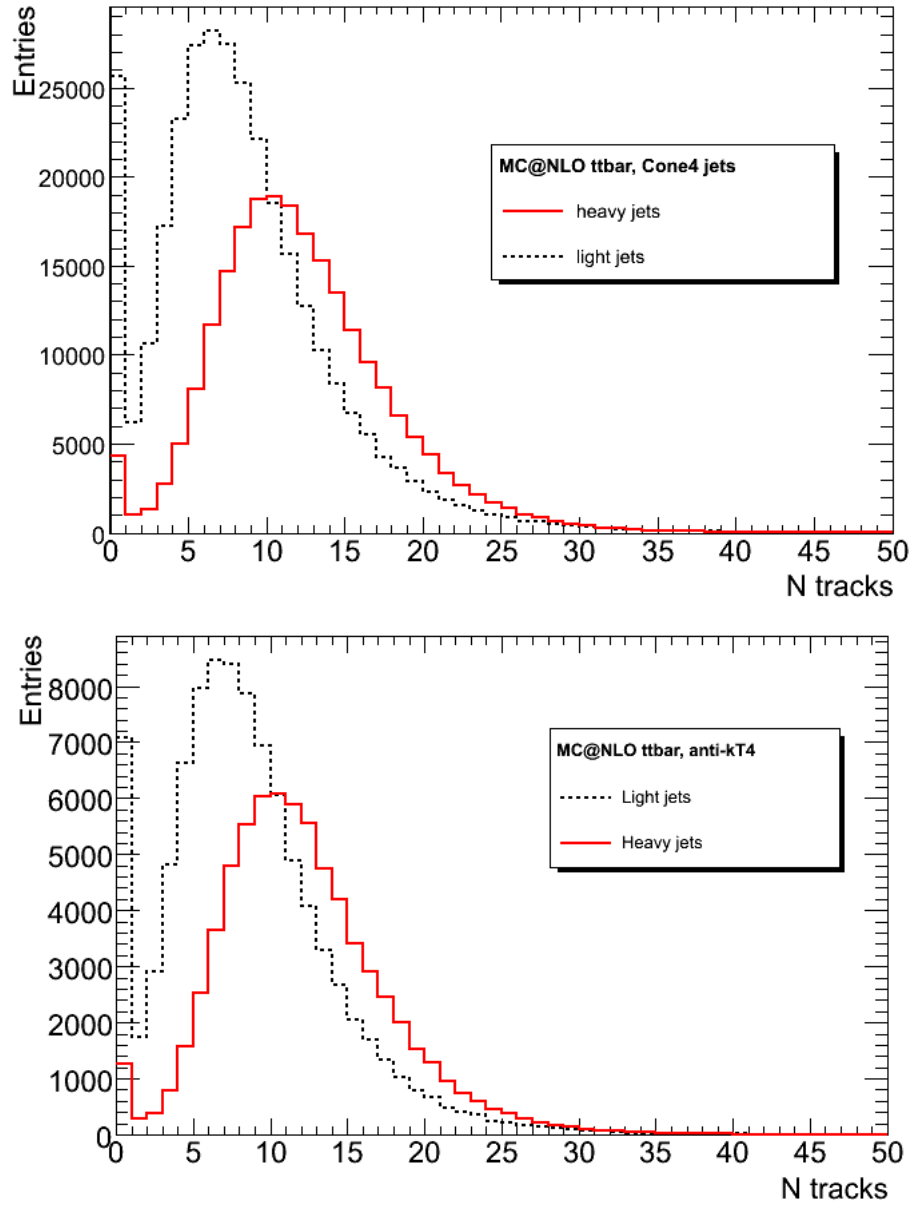


Figure 3.12: Track multiplicities per jet for heavy and light Cone $\Delta R < 0.4$ jets (top plot) and for anti- k_T4 jets (bottom plot) with transverse energy higher than 15 GeV and $|\eta| < 2.5$.

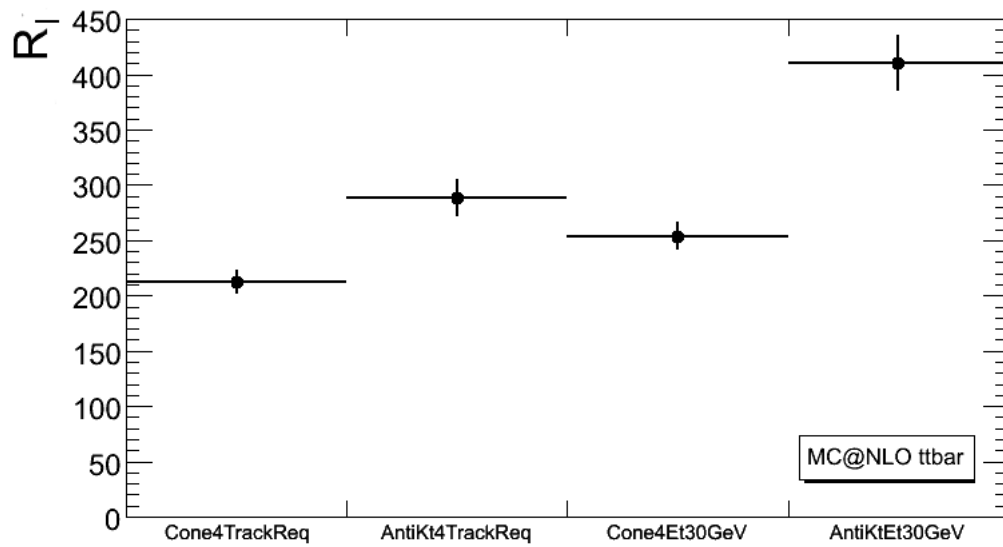


Figure 3.13: Light jet rejection rates for 50% b-tagging efficiency for cone and anti- k_T jet reconstruction algorithms. At least two tracks per jet are required in addition to the jet energy cut of 15 GeV before the tagging procedure for the results shown in the first and second bins. The last two bins show the b-tagging performance without the track requirement, but with a jet energy cut of 30 GeV.

symmetric in space. Therefore the track to jet association for k_T jets could benefit from transverse momentum weighted track association. Considering that low momentum tracks are bent more strongly in the magnetic field of the inner detector we implemented a momentum weighted association of tracks with jets. We have chosen the highest transverse momentum track as reference. The other tracks were associated within a cone size given by the following expression:

$$p_T \Delta R < p_{Tmax} R, \quad (3.3)$$

where p_T is the transverse momentum of the track, p_{Tmax} is the highest transverse momentum of all tracks of the given jet within the cone with respect to the jet axis, and $R=0.4$ is the fixed cone size. It follows from this relation that low momentum tracks will be

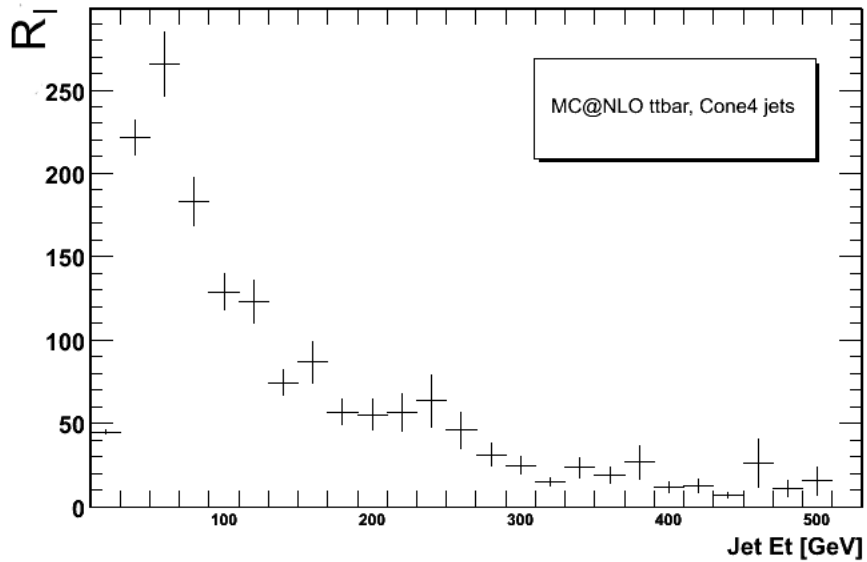


Figure 3.14: The light rejection rates for the fixed b-tagging efficiency point (50%) vs jet transverse energy.

associated with jets with relatively large cone size.

The performance of the b-tagging procedure for k_T jets with the new track association procedure is shown in figure 3.15. The performance is slightly lower for the new track association procedure since there was no selection on associated tracks. In order to reduce the effects of possible fake tracks a cut of $p_T > 2$ GeV for associated tracks can be introduced, since this cut reduces fake track rates in jets [2]. The results are also shown in figure 3.15, 3rd bin. The performance of the b-tagging for k_T jets with the new track association procedure gives the same results as with the standard fixed cone size association.

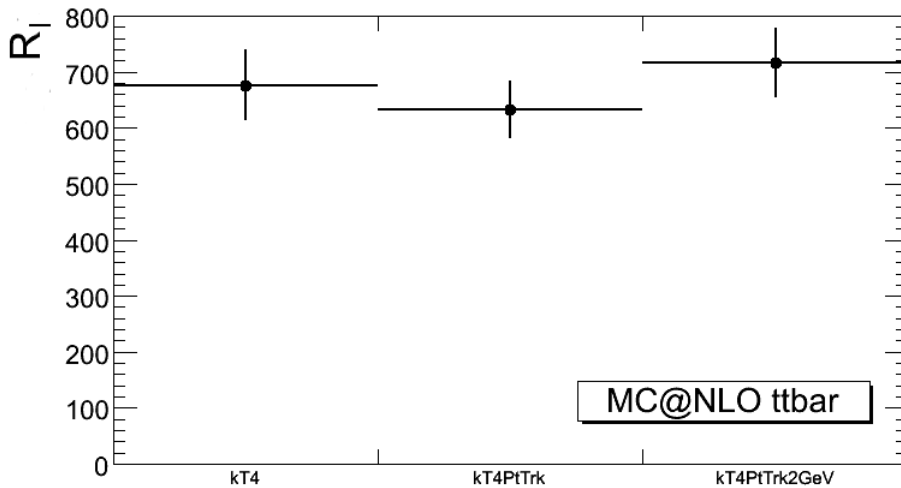


Figure 3.15: The light jet rejection rates, R_l for 50% b-tagging efficiency for the k_T jet reconstruction algorithm. The first bin corresponds to the track association with fixed cone, the second bin displays the result of the p_T -weighted track association procedure and in the third bin an additional track quality cut is applied before the p_T -weighted track association procedure, see text for details

3.4.4 Performance of different b-tagging calibration scenarios

Before the LHC starts running the likelihood-based tagging algorithms the probability density functions are built using Monte Carlo simulated events. Later, data-driven methods can be used, where the pdfs are derived from a pure b-jet sample e. g. extracted from $t\bar{t}$ events [2].

For physics analysis various jet reconstruction algorithms are used at ATLAS chosen depending on the event topology. We need to get b-tagging information for any jet collection used for the physics studies. We studied how the performance of b-tagging for a given jet reconstruction algorithm is affected when using the calibration files derived for another jet reconstruction algorithm. The b-tagging performance in terms of the light jet rejection rates are better with the consistent calibration for each given jet reconstruction algorithm, but using the calibration files derived for other jet collections gives comparable results, as shown in figure 3.10.

3.5 Summary of systematic performance studies

We investigated the b-tagging performance for various ID misalignment scenarios. The b-tagging performance in terms of light jet rejection power drops significantly when the innermost pixel layer is misaligned. Random misalignment of the ID elements also gives significant changes in the b-tagging performance. Performance can be recovered by alignment, e. g. curl vs align/curl or Day 1 vs Day 100 in figure 3.5. It was shown that the b-tagging performance depends on the choice of jet reconstruction algorithm: k_T and anti- k_T al-

gorithms show better performance than the fixed cone algorithm. This affect can be explained by considering the differences in the number of final jets in the events and differences in their properties for cone and k_T algorithms. Also a general drop in the performance was observed when the geometrical size of the reconstructed jet was increased, i. e. from cone $\Delta R = 4$ to cone $\Delta R = 7$. The b-tagging performance depends slightly on the jet calibration procedure. We investigated b-tagging calibration scenarios with various jet algorithms and it was seen that the b-tagging performance for a given jet algorithm does not change dramatically when calibration files are produced using different jet algorithms. We studied the track-to-jet association procedure and implemented p_T -weighted cone association for the jets reconstructed with a k_T algorithm. We were able to show that after some track quality criteria are applied the performance is identical to the fixed cone association procedure.

Chapter 4

Top-Antitop cross section measurement with early data

The SM top quark decays to Wb with a branching ratio of $\sim 100\%$. The final state of the $t\bar{t}$ system depends on the decay modes of the W bosons. The final states are referred to as *lepton plus jets*, *all jets* and *di-lepton* channels, as discussed in chapter 1.1.5. The $t\bar{t}$ pair production cross section will be measured in ATLAS using all these channels. Here only the *lepton plus jets* final state will be discussed. This final state occurs when one W decays leptonically and the other decays hadronically. The branching fraction for the *lepton plus jets* channel is 44%. The final state is characterized by 4 energetic jets, one lepton and one neutrino which can be measured indirectly as missing energy in the detector.

It is expected that with the early data top quarks will be "re-discovered" at the LHC. Precise measurements of its properties will be obtained after having a better understanding of the detector cal-

ibration and the reconstruction algorithms.

The "cut and count" method was investigated for the early data measurement of the $t\bar{t}$ cross section with and without b-tagging. This method has the advantage that it does not rely on estimating correctly the shape of any distribution such as the top mass, but on the other hand it presents the disadvantage, that to estimate the signal and background contributions, it relies on a Monte Carlo simulation which will not be optimal at early stage. A related problem is the overall normalization of the background processes.

The studies reported here are based on 200 pb^{-1} of ATLAS simulated data, assuming 10 TeV pp-collisions. As shown in chapter 3.5 the b-tagging performance is sensitive to the alignment of the inner detector and the jet reconstruction algorithms. We investigated the systematic uncertainties on the cross section measurements with b-tagging for various scenarios of the alignment of the inner detector, for several jet reconstruction algorithms and for variations of the absolute jet energy scale (JES). Also the uncertainties coming from the MC generators were studied by looking at ACERMC and MC@NLO event samples. Different Monte Carlo data sets with various initial and final state radiation (FSR/ISR) parameterizations were used to estimate FSR/ISR modeling uncertainties.

4.1 Theoretical cross section and simulated data sets

At the LHC, due to the high center of mass energy, $t\bar{t}$ production takes place at small momentum fraction of the proton constituents. This process is dominated by gluon-gluon fusion as discussed in chapter 1.1.5. The theoretical cross section was calculated

at NLO ([81], [82]) and using resummation techniques up to next-to-leading logarithms (NLL) [83]. The corresponding cross section for 10 TeV cms energy, using the CTEQ6.6 PDFs [84] and assuming $m_t = 172.5$ GeV, is estimated to be [83]:

$$\sigma_{t\bar{t}}^{NLO+NLL} = 396.9\text{pb}_{-9.2}^{+8.6}(\text{scales})_{-6.5}^{+4.9}(\text{PDFs}) \quad (4.1)$$

where the uncertainties come from the renormalization and factorization scales and from the error on the PDF sets. Recent theoretical calculations include terms of NNLL accuracy and this results in "approximate" NNLO QCD predictions. The so-called "K factors" were introduced to normalize production cross sections to the latest theoretical cross-section calculations whenever available [85].

NLO MC generators ([71], [86]) were used to simulate $t\bar{t}$ pair production and decay. The value of $m_t = 172.5$ GeV was used for the generation. The samples were processed with the full GEANT4 ATLAS detector simulation and reconstruction code [73], [74]. The CTEQ6M [38] parton density functions were used, which are not identical to the ones used for the cross section estimation. Fragmentation and hadronization was simulated using HERWIG [40] while the underlying event was simulated by the Jimmy MC package [87]. Samples produced with ACERMC [88] using PYTHIA for the hadronization, fragmentation and simulation of the underlying event were used to estimate the uncertainties on the cross section measurement due to initial and final state radiation (ISR and FSR) and MC generator modeling. When K factors are applied, the $t\bar{t}$ production cross sections corresponding to the MC samples are scaled to match the latest theoretical cross-section calculations.

Single top quarks were simulated using the ACERMC matrix element generator together with PYTHIA for hadronization, frag-

mentation and simulation of the underlying event. The CTEQ6M parton density functions were used. The s-channel and Wt-channels are generated at LO accuracy only.

The dominant background process is W boson production with multiple hard gluon radiation, "W plus jets". A leptonic W decay gives the lepton and the missing energy in the event, and with additional jets it mimics $t\bar{t}$ *lepton plus jets* channel signature. Z boson production with multiple hard gluon radiation, "Z plus jets", also can be background for $t\bar{t}$ process. The misreconstructed missing energy in the event and high energetic lepton from Z boson decay with gluon jets can mimic signal signature. The "W plus jets" and "Z plus jets" samples were produced using the ALPGEN generator with HERWIG for the simulation of the fragmentation and hadronization and with Jimmy for the underlying event. The MLM [89] algorithm was used to match parton shower and matrix element calculations.

WW, WZ and ZZ production processes were generated with HERWIG. A filter was applied at generator level to select events with an electron or a muon with $p_T > 10$ GeV.

QCD multi-jet events are a background for the $t\bar{t}$ *lepton plus jets* channel if at least one of the jets in the event is misidentified as an isolated lepton. The ALPGEN program was used to generate these events at LO. The QCD multi-jet background estimation has large uncertainties due to the LO generator tools. Also the estimation of the lepton fake rate depends on full and consistent detector simulation which will be obtained only after an initial period of detector operation. We anticipate deriving the level of the QCD background directly from the data.

Tables 4.1, 4.2, 4.3, 4.4, 4.5 describe all data sets used for the analysis with the corresponding production cross sections and K

Data set	MC generator	K-factor	$K \cdot \sigma(\text{pb})$
<i>di-leptonic</i> and <i>lepton plus jets $t\bar{t}$</i>	MC@NLO	1.07	217.06
All hadronic $t\bar{t}$	MC@NLO	1.07	182.69
<i>di-leptonic</i> and <i>lepton plus jets $t\bar{t}$</i>	ACERMC	2.01	218.37
<i>di-leptonic</i> and <i>lepton plus jets $t\bar{t}$</i> ISR/FSR low top mass	ACERMC	2.01	218.37
<i>di-leptonic</i> and <i>lepton plus jets $t\bar{t}$</i> ISR/FSR high top mass	ACERMC	2.01	218.37
Single top Wt production, semi-leptonic decay	ACERMC	0.99	14.27
Single top t-channel leptonic decay	ACERMC	1.05	43.18

Table 4.1: Top quark samples. See text for details.

factors. For the signal the full detector simulation was applied, but some of the background samples, "W plus jets" and QCD, rely only on a fast simulation of the detector using ATLFAST [90]. The Monte Carlo samples were from the "MC08" production for the ATLAS collaboration [90].

4.2 Reconstruction

The samples used to study the cross section with b-tagging for the various inner detector misalignment scenarios were reconstructed with ATHENA release 14.2.21. At the time of the sample production one of the HEC quadrants was off and the Monte Carlo simulations were designed to reflect this. The samples were reconstructed with various inner detector geometries discussed in chapter 3.4.1. The performance of the b-tagging was affected mostly by the "Curl" misalignment of the inner detector. Therefore the $t\bar{t}$ cross section measurement was performed for this scenario. The inner detector alignment group produced a geometry setting corresponding to the

Data set	$K \cdot \sigma(\text{pb})$
$W \rightarrow e\nu + 0$ parton	12425.334
$W \rightarrow e\nu + 1$ parton	2577.006
$W \rightarrow e\nu + 2$ parton	824.72
$W \rightarrow e\nu + 3$ parton	248.03
$W \rightarrow e\nu + 4$ parton	68.44
$W \rightarrow e\nu + 5$ parton	20.25
$W \rightarrow \mu\nu + 0$ parton	12353.35
$W \rightarrow \mu\nu + 1$ parton	2629.71
$W \rightarrow \mu\nu + 2$ parton	832.41
$W \rightarrow \mu\nu + 3$ parton	246.44
$W \rightarrow \mu\nu + 4$ parton	67.71
$W \rightarrow \mu\nu + 5$ parton	19.89
$W \rightarrow \tau\nu + 0$ parton	12417.53
$W \rightarrow \tau\nu + 1$ parton	2570.42
$W \rightarrow \tau\nu + 2$ parton	820.82
$W \rightarrow \tau\nu + 3$ parton	247.29
$W \rightarrow \tau\nu + 4$ parton	67.47
$W \rightarrow \tau\nu + 5$ parton	20.74
$W + b\bar{b}$	
$W + b\bar{b} + 0$ parton	6.16
$W + b\bar{b} + 1$ parton	6.11
$W + b\bar{b} + 2$ parton	3.53
$W + b\bar{b} + 3$ parton	1.96

Table 4.2: W-boson plus jets samples. The ALPGEN generator version 2.13 and Jimmy were used for the modeling of the underlying event [91]. The generated events were processed through the fast simulation of the detector, except the W plus $b\bar{b}$ samples which were processed with full detector simulation. The K factor is equal to 1.22 for the "W plus jets" samples.

Data set	$K \cdot \sigma$ (pb)
$Z \rightarrow e^+e^- + 0$ parton	1095.78
$Z \rightarrow e^+e^- + 1$ parton	252.01
$Z \rightarrow e^+e^- + 2$ parton	88.45
$Z \rightarrow e^+e^- + 3$ parton	25.72
$Z \rightarrow e^+e^- + 4$ parton	7.32
$Z \rightarrow e^+e^- + 5$ parton	2.11
$Z \rightarrow \mu^+\mu^- + 0$ parton	1098.26
$Z \rightarrow \mu^+\mu^- + 1$ parton	246.25
$Z \rightarrow \mu^+\mu^- + 2$ parton	84.61
$Z \rightarrow \mu^+\mu^- + 3$ parton	26.39
$Z \rightarrow \mu^+\mu^- + 4$ parton	7.42
$Z \rightarrow \mu^+\mu^- + 5$ parton	2.07
$Z \rightarrow \tau^+\tau^- + 0$ parton	1101.31
$Z \rightarrow \tau^+\tau^- + 1$ parton	255.30
$Z \rightarrow \tau^+\tau^- + 2$ parton	85.59
$Z \rightarrow \tau^+\tau^- + 3$ parton	25.70
$Z \rightarrow \tau^+\tau^- + 4$ parton	7.37
$Z \rightarrow \tau^+\tau^- + 5$ parton	2.09

Table 4.3: Z-boson plus jets samples. ALPGEN version 2.13 generator and Jimmy were used for the modeling of the underlying event [91]. The generated events were processed through the full detector simulation. The K factor is equal to 1.22 for the "Z plus jets" samples.

Data set	K-factor	$K \cdot \sigma$ (pb)
WW 1e or $\mu p_T > 10$ GeV	1.69	26.40
ZZ 1e or $\mu p_T > 10$ GeV	1.42	1.94
WZ 1e or $\mu p_T > 10$ GeV	1.81	8.81

Table 4.4: Diboson background samples. The Herwig/Jimmy MC generator was used. The generated events were processed through the full detector simulation.

Data set	$K \cdot \sigma$ (pb)
QCD J2 2 parton	63230.31
QCD J2 3 parton	81822.44
QCD J2 4 parton	137037.51
QCD J2 5 parton	51316.69
QCD J3 2 parton	8841.55
QCD J3 3 parton	122797.54
QCD J3 4 parton	210360.99
QCD J3 5 parton	115115.12
QCD J4 2 parton	31872
QCD J4 3 parton	65508.9
QCD J4 4 parton	49028.2
QCD J4 5 parton	24249.3
QCD J4 6 parton	11571.7
QCD J5 2 parton	750.2
QCD J5 3 parton	1944.8
QCD J5 4 parton	2149.9
QCD J5 5 parton	1392.8
QCD J5 6 parton	972.6

Table 4.5: QCD background samples. The ALPGEN LO MC generator was used for these QCD samples. The generated events were processed through the fast simulation of the ATLAS detector. J2, J3, J4, J5 indicates the p_T slicing strategy which was used at generator level [90]. Each parton multiplicity sample is the sum of multiple Jx slices, in our case from J2 to J5 corresponding to $p_T=35$ GeV to $p_T=560$ GeV

”Day 1” expectation of the alignment precision. This is based on a direct survey of the detector and the results from the alignment procedure with cosmic rays taken during the 2008 detector operation [78]. An additional estimate of the precision of the detector alignment is the so-called ”Day 100” geometry, obtained with track based alignment after sufficient collision data [79]. The cross section measurement was carried out also in the case of this second scenario.

The samples used to estimate the $t\bar{t}$ pair production cross section with and without b-tagging and also several background samples were reproduced with ATHENA release 14.2.25. As the HEC quadrant problem was already solved, the samples were processed with the full ATLAS detector geometry. These samples were used to study the dependence of the cross section measurement on the jet reconstruction algorithms, jet energy scale, initial and final state radiation and MC generator effects.

4.2.1 Trigger

At the start of the LHC running with low luminosity and cms energy, the triggering will be performed with lower thresholds, loose selection requirements and with less pre-scaling. The $t\bar{t}$ *lepton plus jets* channel will be triggered with single lepton triggers. The lepton trigger efficiency will be measured from data using Z events with an expected uncertainty of the order of 1 % for an integrated luminosity of 200 pb^{-1} . The overlap between the trigger and offline object selection is estimated to be 80-90 % [2]. For the estimation of the systematic uncertainties on the $t\bar{t}$ cross section measurements the effect of the lepton trigger selection is negligible. The trigger information was not considered and the selection was based on offline

reconstruction of the objects.

4.2.2 Electron reconstruction

Electron candidates are reconstructed by the ATLAS calorimeters and tracking detector. Electrons are defined by the "eGamma" algorithm [2]. We use the so-called "tight" electrons defined by a likelihood analysis [2]. The electron candidates were required to have pseudo-rapidity in the range $0 \leq |\eta| \leq 2.5$ and $p_T > 20$ GeV. The good electrons were required to be isolated based on calorimeter energy: the additional transverse energy E_T in a cone with radius $\Delta R = 0.2$ around the electron axis was required to be less than 6 GeV.

The error of the electron identification efficiency is expected to be of the order of 1 % [2].

4.2.3 Muon reconstruction

Muons are reconstructed using both the muon spectrometer and inner detector. The muon reconstruction is performed using the Sta-coMuon algorithm [2]. The muons are required to have a minimum transverse momentum $p_T > 20$ GeV and to lie in the pseudorapidity range $|\eta| \leq 2.5$. The isolation criteria are based on the calorimeter energy: the additional transverse energy E_T in a cone with radius $\Delta R = 0.2$ around the muon is required to be less than 6 GeV.

The muon identification efficiency error is expected to be of the order of 1 % [2].

4.2.4 Jet and missing energy reconstruction

The jets were reconstructed with the standard ATLAS cone algorithm in $\eta - \phi$ space with a cone radius of 0.4 based on the energy deposits in calorimeter towers of size $\Delta\eta \times \Delta\phi = 0.1 \times 0.1$. Cross section values for the other jet reconstruction algorithms were also estimated. Topological clusters with local calibration were used to reconstruct the jets with the k_T and anti- k_T ($D = 0.4$ and 0.6) algorithms discussed in chapter 3.1. The jets used in the analyses were required to have a minimum transverse momentum of $p_T > 20$ GeV and a pseudorapidity $|\eta| \leq 2.5$. In ATLAS electron candidates are also reconstructed as jets. We therefore removed the jets which overlap with a good electron within a cone of size $\Delta R < 0.15$.

The missing transverse energy (MET) in the event was calculated as the vector sum of the transverse energy coming from calorimeter cells, muons, and correction factors for energy loss in the material in front of the calorimeter [2].

4.3 Cut and count method

The cut-based counting method is a simple approach to measure the cross-section. The number of events that pass the event selection are counted and all expected backgrounds are subtracted in order to obtain the yield of $t\bar{t}$ events in the sample. The event selection efficiency on signal, ϵ , is computed from Monte Carlo simulation. The background contributions are also estimated purely from the Monte Carlo simulations. From the number of observed events meeting the selection criteria N_{sel} , the expected background N_{bkg} and the

integrated luminosity L , the cross-section is determined as:

$$\sigma = \frac{N_{sel} - N_{bkg}}{L \times \epsilon}, \quad (4.2)$$

The total selection efficiency ϵ includes the geometrical acceptance and the event selection efficiencies.

The "cut and count" method will be used in the commissioning phase of the detector before MC tuning with real data is available for more sophisticated methods. One expects large background estimation uncertainties and also large systematic uncertainties derived from FSR/ISR modeling and JES determination.

4.4 Event selection

As discussed in chapter 1.1.5 the signature of the *lepton plus jets* channel is the following: one high p_T lepton, at least 4 highly energetic jets (two of them originating from b quarks) and missing transverse energy in the event. Event selection relies on the reconstruction and selection of these objects, and is adjusted to obtain the best signal to background separation. Final state object reconstruction was introduced above and the $t\bar{t}$ selection follows in this section.

4.4.1 Pre-Selection(DPD)

Simulated data sets were processed in two steps. The first is the derived physics data (DPD) production chain where a loose selection is applied to reduce the size of the samples. During this stage events were required to have at least one lepton with $p_T > 10$ GeV, at least 3 jets with $p_T > 10$ GeV and at least 2 jets with $p_T > 20$ GeV. The $|\eta|$ acceptance of all objects was set up to 3. There was no

Process	DPD filter efficiency	Nominal+MET	+ b-tagging
<i>di-leptonic</i> and <i>lepton plus jets</i> $t\bar{t}$ MC@NLO	0.721	0.221	0.171
<i>di-leptonic</i> and <i>lepton plus jets</i> $t\bar{t}$ ACERMC	0.727	0.252	0.195
all-hadronic $t\bar{t}$ MC@NLO	0.845	0.0011	0.0008
Single top Wt channel	0.647	0.086	0.058
Single top t-channel	0.526	0.077	0.056

Table 4.6: DPD filter efficiencies for the top quark samples. Nominal plus MET and plus b-tagging selection efficiencies are shown for the complete data sets.

missing transverse energy requirement during the loose selection. DPD selection efficiencies for the signal and for the background data sets are shown in tables 4.6, 4.7, 4.8, 4.9.

4.4.2 Final Selection

The nominal selection of the $t\bar{t}$ system requires at least one good lepton, as described above, at least 4 jets with $p_T > 20$ GeV, and at least 3 jets with $p_T > 40$ GeV. Jet-lepton overlap removal was done as described in section 4.2.4. Isolated muons close to the jet (overlap within a cone of size $\Delta R < 0.15$) were also removed to eliminate muons coming from leptonic decays of B and D mesons. In addition to the nominal selection a missing transverse energy above 20 GeV was required whenever stated. Tagging of jets originating from b quark was examined. Jets were tagged using the combined tagger algorithm discussed in detail in chapter 3.1.1. For our selection at least one jet with a weight above 6 was required which approximately corresponds to 60 % b-tagging efficiency.

Process	DPD filter efficiency	Nominal+MET	+ b-tagging
$W \rightarrow e\nu$ +0 parton	0.015	0.00032	$5 \cdot 10^{-5}$
$W \rightarrow e\nu$ +1 parton	0.153	0	0
$W \rightarrow e\nu$ +2 parton	0.460	0.00034	$2 \cdot 10^{-5}$
$W \rightarrow e\nu$ +3 parton	0.559	0.00677	0.00020
$W \rightarrow e\nu$ +4 parton	0.623	0.07321	0.00428
$W \rightarrow e\nu$ +5 parton	0.690	0.19111	0.01368
$W \rightarrow \mu\nu$ +0 parton	0.006	0	0
$W \rightarrow \mu\nu$ +1 parton	0.025	0	0
$W \rightarrow \mu\nu$ +2 parton	0.242	0.00101	$6 \cdot 10^{-5}$
$W \rightarrow \mu\nu$ +3 parton	0.625	0.00861	0.00050
$W \rightarrow \mu\nu$ +4 parton	0.761	0.08394	0.00506
$W \rightarrow \mu\nu$ +5 parton	0.823	0.22260	0.01697
$W \rightarrow \tau\nu$ +0 parton	0.008	0	0
$W \rightarrow \tau\nu$ +1 parton	0.023	0	0
$W \rightarrow \tau\nu$ +2 parton	0.091	0.00031	$5 \cdot 10^{-5}$
$W \rightarrow \tau\nu$ +3 parton	0.181	0.00352	0.00038
$W \rightarrow \tau\nu$ +4 parton	0.278	0.03042	0.00216
$W \rightarrow \tau\nu$ +5 parton	0.374	0.07091	0.00491
$W+b\bar{b}$ +0 parton	0.25	0.00053	0.00026
$W+b\bar{b}$ +1 parton	0.47	0.00740	0.00672
$W+b\bar{b}$ +2 parton	0.58	0.06841	0.05319
$W+b\bar{b}$ +3 parton	0.65	0.18394	0.12612
WW	0.46	0.012793	0.000964
ZZ	0.58	0.005529	0.000864
WZ	0.49	0.011124	0.001011

Table 4.7: DPD filter and event selection efficiencies for the "W plus jets" and di-boson background samples. Nominal plus MET and plus b-tagging selection efficiencies are shown for the complete data sets. Some of the channels do not survive event selection and the corresponding efficiencies are set to 0.

Process	DPD filter efficiency	Nominal+MET	+b-tagging
$Z \rightarrow e^+e^- +0$ parton	0.18	0	0
$Z \rightarrow e^+e^- +1$ parton	0.6	0	0
$Z \rightarrow e^+e^- +2$ parton	0.75	0.00060	$3.69 * 10^{-5}$
$Z \rightarrow e^+e^- +3$ parton	0.83	0.00926	0.00065
$Z \rightarrow e^+e^- +4$ parton	0.9	0.03362	0.00254
$Z \rightarrow e^+e^- +5$ parton	0.97	0.09750	0.00678
$Z \rightarrow \mu^+\mu^- +0$ parton	0.01	0	0
$Z \rightarrow \mu^+\mu^- +1$ parton	0.04	0	0
$Z \rightarrow \mu^+\mu^- +2$ parton	0.32	0.00062	$3*10^{-5}$
$Z \rightarrow \mu^+\mu^- +3$ parton	0.75	0.00620	0.00031
$Z \rightarrow \mu^+\mu^- +4$ parton	0.9	0.04798	0.00422
$Z \rightarrow \mu^+\mu^- +5$ parton	0.95	0.14181	0.00945
$Z \rightarrow \tau^+\tau^- +0$ parton	0.02	0	0
$Z \rightarrow \tau^+\tau^- +1$ parton	0.1	0	0
$Z \rightarrow \tau^+\tau^- +2$ parton	0.24	0.00131	$4*10^{-5}$
$Z \rightarrow \tau^+\tau^- +3$ parton	0.4	0.01619	0.00108
$Z \rightarrow \tau^+\tau^- +4$ parton	0.56	0.04969	0.00427
$Z \rightarrow \tau^+\tau^- +5$ parton	0.65	0.09617	0.01006

Table 4.8: DPD filter, nominal plus MET and plus b-tagging selection efficiencies for the "Z plus jets" background samples. Some of the channels do not survive event selection and the corresponding efficiencies are set to 0.

Process	DPD filter efficiency	Nominal+MET	+ b-tagging
QCD J2 2 parton	0.56	$3 \cdot 10^{-5}$	$2 \cdot 10^{-5}$
QCD J2 4 parton	0.28	$6 \cdot 10^{-6}$	$3 \cdot 10^{-6}$
QCD J2 5 parton	0.52	$8 \cdot 10^{-6}$	$4 \cdot 10^{-6}$
QCD J3 2 parton	0.45	$7.6 \cdot 10^{-5}$	$7.6 \cdot 10^{-5}$
QCD J3 3 parton	0.31	$2.2 \cdot 10^{-5}$	$1.6 \cdot 10^{-5}$
QCD J3 4 parton	0.29	$1.2 \cdot 10^{-5}$	$1.6 \cdot 10^{-6}$
QCD J3 5 parton	0.59	$2.7 \cdot 10^{-5}$	$10.0 \cdot 10^{-6}$
QCD J4 2 parton	0.06	0.000164	0.000109
QCD J4 3 parton	0.14	$4.3 \cdot 10^{-5}$	$1.1 \cdot 10^{-5}$
QCD J4 4 parton	0.31	$7.1 \cdot 10^{-5}$	$3.6 \cdot 10^{-5}$
QCD J4 5 parton	0.57	$4.6 \cdot 10^{-5}$	$3.0 \cdot 10^{-5}$
QCD J5 2 parton	0.07	0.000534	0.000467
QCD J5 3 parton	0.17	0.000360	0.000275
QCD J5 4 parton	0.32	0.000198	0.000131
QCD J5 5 parton	0.56	0.000171	$8.3 \cdot 10^{-5}$

Table 4.9: DPD filter, nominal plus MET and plus b-tagging selection efficiencies for the QCD multi-jet background samples.

4.4.3 Selection efficiencies with and without heavy flavour tagging

Simulated data sets corresponding to an integrated luminosity of 200 pb^{-1} were used. The size of the data samples needed was estimated from the knowledge of the $t\bar{t}$ MC production cross section. The selection efficiency was calculated with and without b-tagging. As a cross-check it has also been estimated using a full MC statistics. The corresponding selection efficiencies are shown in table 4.10 and are in good agreement within the statistical error for both selection scenarios.

After the final selection, the efficiency for the signal events is around 16 % for the nominal selection plus MET requirement, while for most of the background contributions drop dramatically. The "W plus 5 partons" and "W plus $b\bar{b}$ " samples, followed by "Z plus 5 partons", remain as the main background of the $t\bar{t}$ *lepton plus jets* channel.

4.4.4 Selection efficiencies for the ACERMC and MC@NLO samples

The next step was to calculate the selection efficiency based on the ACERMC [88] samples to estimate the effect of the different underlying models used for the MC generators. Signal events were produced with two different Monte Carlo programs interfaced to the full ATLAS detector simulation (MC@NLO and ACERMC). The number of $t\bar{t}$ events obtained with the default simulation (MC@NLO) can then be compared to the one obtained from various generators, to estimate the difference in efficiency. The maximum resulting value is then taken as the uncertainty on the modeling of signal with MC

generator. The corresponding selection efficiencies are shown in table 4.10. The selection efficiencies for MC@NLO and ACERMC $t\bar{t}$ data sets differ by 15 % after the nominal event selection plus MET requirements. The difference remains about the same after the b-tagging requirements.

Studies at the MC truth level showed that ACERMC has a lower proportion of *di-leptonic* events than MC@NLO. The difference can be explained by the inclusion of QCD corrections to the W decay in ACERMC that increases the branching ratio of *lepton plus jets* events compared to the *di-leptonic* ones. These corrections are not included in MC@NLO [90]. Moreover ACERMC on average generates t quarks with harder p_T resulting in a shift of the mean of the p_T distribution of about 8 GeV together with a fall-off at high p_T . This leads to a slightly harder lepton spectrum with a shift of the mean of the p_T distribution by $\sim 1 - 2$ GeV [90]. In figure 4.1 the selected lepton and jet p_T distributions for MC@NLO and ACERMC samples corresponding to 40000 $t\bar{t}$ events are shown. For MC@NLO there are more leptons in the same number of events, as explained above. ACERMC has a smaller branching ratio for leptonic W boson decays, but if we take the same number of selected leptons, ACERMC gives a slightly harder lepton p_T spectrum as is shown in figure 4.2.

4.4.5 Selection efficiencies for various misalignment scenarios

During early data taking the alignment precision of the ID will play an important role for many physics measurements. As shown in chapter 3.4.1 the b-tagging performance depends on the ID align-

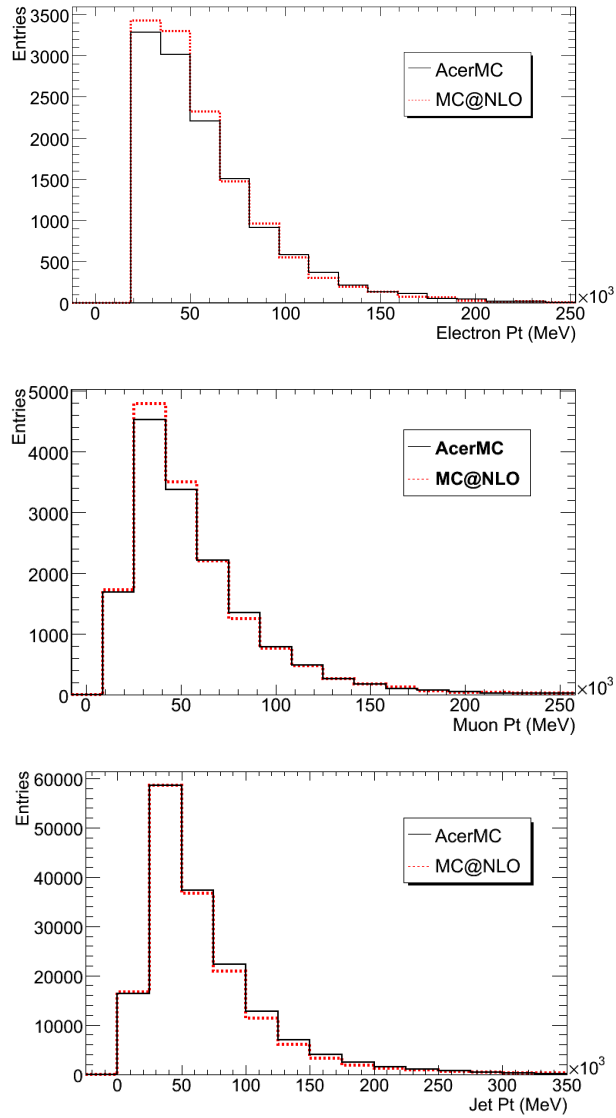


Figure 4.1: Selected top decay object p_T distributions for electrons, muons and jets from top to bottom. MC@NLO and ACERMC data samples corresponding to 40000 $t\bar{t}$ events were used.

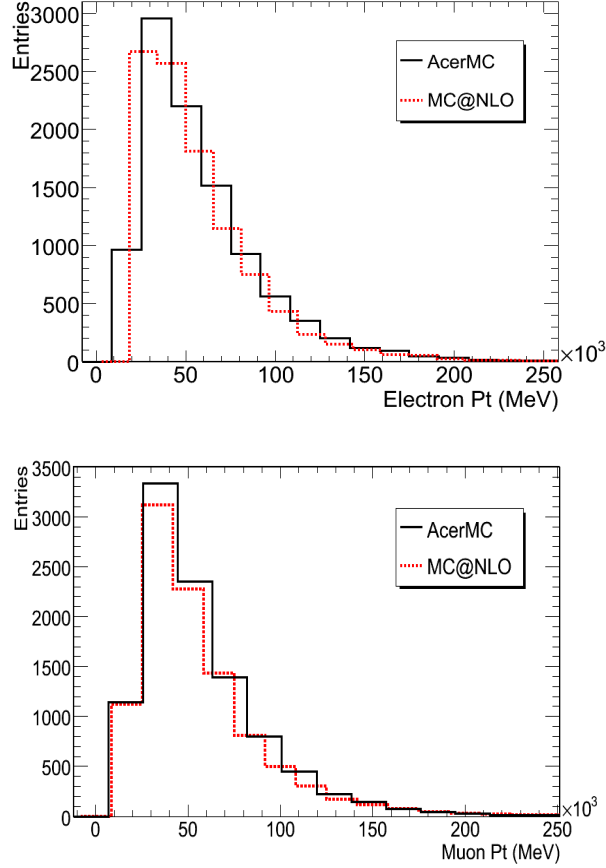


Figure 4.2: The p_T distributions of 10000 selected leptons from top decays for electrons (top) and muons (bottom). MC@NLO and ACERMC data samples were used.

Data sample	Nominal selection+MET	+b-tagging
$t\bar{t}$ MC@NLO high stat.	0.159 ± 0.002	0.123 ± 0.002
$t\bar{t}$ MC@NLO 200 pb^{-1}	0.159 ± 0.005	0.123 ± 0.005
$t\bar{t}$ ACERMC 200 pb^{-1}	0.183 ± 0.004	0.142 ± 0.004

Table 4.10: Selection efficiencies ($\epsilon_{DPD} \times \epsilon_{sel}$) for the MC@NLO and ACERMC $t\bar{t}$ data samples. The final efficiency is the product of the corresponding DPD filter efficiencies multiplied to the final event selection efficiencies for the given data sets.

ment precision. Therefore we have estimated the $t\bar{t}$ selection efficiencies for various ID geometries.

As shown in chapter 3.4.1 the flavour tagging performance does not change for most of the systematic ID misalignment scenarios which have been investigated. The most significant changes appear when a random misalignment of ID elements is used or for the "Curl" systematic misalignment.

We study the geometry with a random misalignment of ID modules which was simulated using the knowledge from the cosmic data alignment in 2008. It corresponds to the alignment accuracy for first day collision data taking ("Day 1" scenario). The second geometry was produced using MC studies to estimate the accuracy of the alignment after one hundred days ("Day 100" scenario) of collision data taking. More details are given in chapter 3.4.1. The "Curl" systematic misalignment was used as a third variation. The corresponding $t\bar{t}$ selection efficiencies are shown in table 4.11. The samples used for these studies were processed with ATLAS geometry in which one HEC quadrant is off. The selection efficiency is therefore lower for the perfect geometry than in the case of the previous MC studies shown in table 4.10.

The "Curl" misalignment of the ID does not cause a significant change in the $t\bar{t}$ selection efficiency before the b-tagging requirement. If at least one b-tagged jet is required the difference between the selection efficiencies w.r.t. the perfect knowledge of the geometry is significant and it corresponds to a 5 % change for the cross section. For the "Day 1" and "Day 100" geometries we do not observe significant differences between the selection efficiencies. The maximum difference is 1.3 % for the efficiencies after the b-tagging requirement. The random misalignments were introduced only for

Geometry	Nominal selection	Nominal +btagging
Perfect	0.1505 ± 0.0033	0.1139 ± 0.0034
"Curl"	0.1483 ± 0.0046	0.1195 ± 0.0047
"Day 1"	0.1499 ± 0.0045	0.1154 ± 0.0046
"Day 100"	0.1499 ± 0.0045	0.1148 ± 0.0046

Table 4.11: The $t\bar{t}$ selection efficiencies for the various ID misalignment scenarios. MC@NLO generated $t\bar{t}$ data samples were used.

the x and y directions. No shift in the z direction and no rotations of the ID modules were considered. The b-tagging performance was rather stable in case of the "Day 1" and "Day 100" geometries shown in chapter 3.4.1. Therefore also the cross section estimation with b-tagging also is stable against random misalignment scenarios.

4.4.6 Selection efficiencies for various jet algorithms

As discussed in chapter 3.1 there are several jet reconstruction algorithms used within ATLAS. The selection efficiencies for various jet reconstruction algorithms were calculated. We reconstructed the jets with fixed cone size ($\Delta R = 0.4$), k_T ($D = 0.4$) and anti- k_T ($D = 0.4$) reconstruction algorithms and then the corresponding $t\bar{t}$ selection efficiencies were calculated for a MC sample with high statistics and for data sets corresponding to a luminosity of 200 pb^{-1} . The results are shown in table 4.12. The selection efficiencies are in good agreement within the statistical error for both MC@NLO and ACERMC simulated data sets for all the jet reconstruction algorithms. If we compare the results corresponding to the various jet reconstruction algorithms for the two different MCs we see that the differences between the jet algorithms are the same for both MC generators within less than 1 %.

Data Set	Jet algorithm	Nominal selection+MET	+btagging
MC@NLO high stat.	Cone4	0.159±0.002	0.123±0.002
MC@NLO 200 pb ⁻¹	Cone4	0.159±0.005	0.123±0.005
ACERMC 200 pb ⁻¹	Cone4	0.183±0.004	0.142±0.004
MC@NLO high stat.	anti- k_T 4	0.150±0.002	0.118±0.002
MC@NLO 200 pb ⁻¹	anti- k_T 4	0.148±0.004	0.117±0.004
ACERMC 200 pb ⁻¹	anti- k_T 4	0.173±0.004	0.137±0.004
MC@NLO high stat.	k_T 4	0.156±0.002	0.122±0.002
MC@NLO 200 pb ⁻¹	k_T 4	0.154±0.004	0.121±0.004
ACERMC 200 pb ⁻¹	k_T 4	0.180±0.004	0.141±0.004

Table 4.12: Selection efficiencies ($\epsilon_{DPD} \times \epsilon_{sel}$) for MC@NLO $t\bar{t}$ and ACERMC data samples with full detector simulation. Two sets for each jet reconstruction algorithms are considered. Once it is estimated for the high statistics and second set for the lower statistics corresponding to the luminosity of 200 pb⁻¹. The selection with and without b-tagging was examined.

4.4.7 Selection efficiencies for various jet energy scales

The determination of the absolute JES will be performed during detector operation. There are several methods utilized by ATLAS. For example γ +jet events can be used to propagate the electromagnetic scale to the hadronic scale. The JES depends on a variety of detector and physics effects: non-linearities in the calorimeter response due to non-compensation of the calorimeter or due to energy losses in dead material such as the cryostat [2]. The underlying event leads to additional energy sources. Energy lost outside the jet cone has an impact on the measured jet energy. To estimate the sensitivity of the analyses to the uncertainty on the JES in early data we scale the energy requirement of the jets by a fixed amount. Values of 5 % and 10 % were used to scale the jet energy requirement for the event selection. The resulting variation in the efficiency measurement gives

JES[%]	Nominal selection	+ b-tagging
-10	0.202±0.004	0.158±0.004
-5	0.223±0.004	0.174±0.004
0	0.245±0.004	0.190±0.004
+5	0.267±0.004	0.207±0.004
+10	0.29±0.004	0.225±0.004

Table 4.13: Event selection efficiencies for $t\bar{t}$ MC@NLO data samples with full detector simulation corresponding to 200 pb^{-1} of luminosity. The efficiencies for the various absolute JES assumptions were calculated.

a good measure of the systematic uncertainty due to the jet energy scale. We did not scale the missing transverse energy which would be also affected due to the variation of the JES. Therefore for the JES studies there was no MET requirement for the event selection. Table 4.13 displays the selection efficiencies for various JES cases. Under-estimated jet energy scales cause a relative drop of the selection efficiencies and conversely over-estimated jet energy scale leads to higher selection efficiencies. Figures 4.3 and 4.4 show the selection efficiency dependence on the JES variation for the nominal selection and the nominal plus b-tagging requirement. From these plots the variation of the selection efficiency corresponding to a 1 % JES variation is about $(1.8 \pm 0.1) \%$ and $(1.75 \pm 0.13 \%)$ for the nominal selection and the nominal plus b-tagging selections. The efficiency variations corresponding to 5-10 % JES variations are given in table 4.14.

4.4.8 Initial and Final State Radiation systematics

The modeling of Initial and Final State Radiation (ISR and FSR) in the MC affects the number of jets in the final state and the

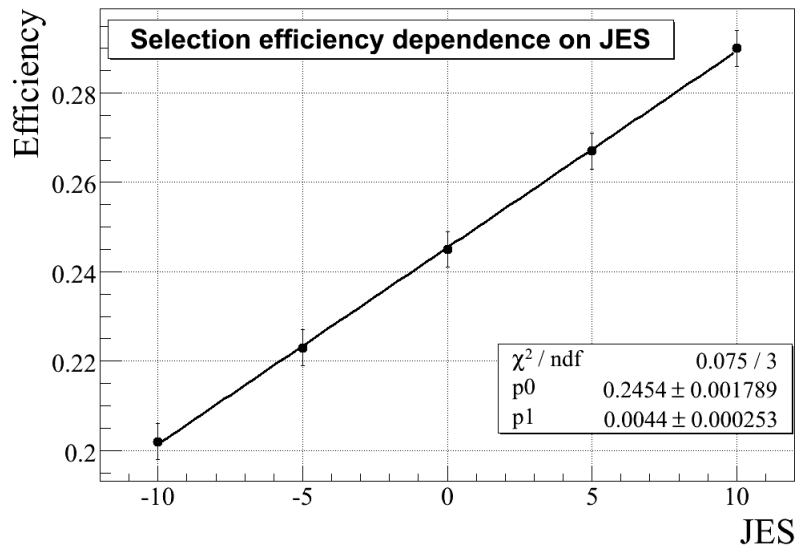


Figure 4.3: Selection efficiency dependence on JES.

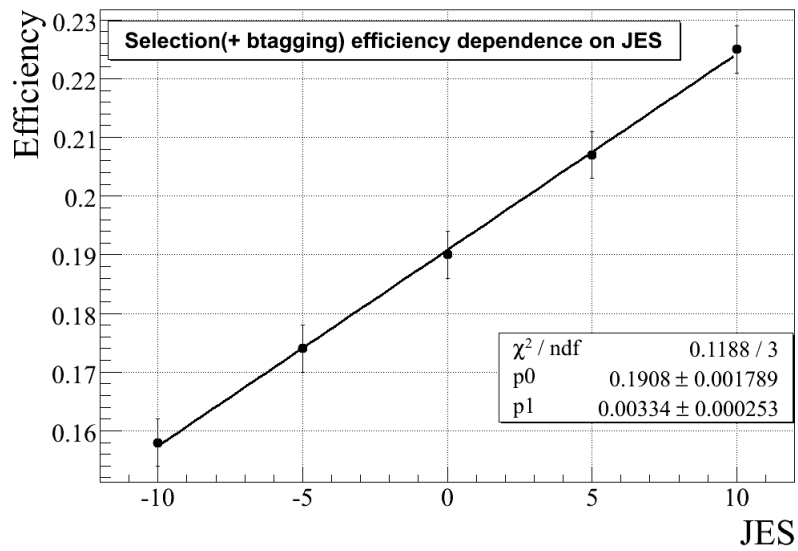


Figure 4.4: Selection with b-tagging efficiency dependence on JES.

JES	$\Delta\epsilon/\epsilon$
$\pm 10\%$ JES	$\pm 18\%$
$\pm 5\%$ JES	$\pm 9\%$

Table 4.14: The variation of the $t\bar{t}$ selection efficiencies corresponding to $\pm 10\%$ and $\pm 5\%$ JES. They are estimated using MC@NLO generated data samples corresponding to 200 pb^{-1} luminosity.

transverse momentum distribution of the particles. Therefore the $t\bar{t}$ selection efficiency will depend on the choice of the parameters used to model these processes. To estimate the systematic error coming from the ISR/FSR modeling, two different MC data sets were produced within ATLAS, using the same MC generator (ACERMC interfaced with PYTHIA for the parton showering) with the most significant variation of the FSR/ISR modeling parameters [69]. These two data sets give the maximum positive and negative deviations of the reconstructed top mass w.r.t the central value obtained with a reference sample which has the default PYTHIA parameters for showering [90]. The latter one was also used for the estimation of the MC generator uncertainties in section 4.4.4.

Table 4.15 shows the selection efficiency for the three data sets discussed above. The selection efficiencies varies from 9-10 % in the case of nominal selection plus MET requirement to 10-11 % when b-tagging is required in addition. The maximum deviation of the selection efficiency is considered to be the systematic error coming from the ISR/FSR modeling.

4.4.9 PDF uncertainties

The uncertainties due to the parton distribution functions (PDF) were studied within ATLAS [84], [92], [93] exploiting the hard parton

Data sample	Nominal selection+MET	+b-tagging
$t\bar{t}$ ACERMC FSR/ISR lower top mass	0.168±0.001	0.128±0.002
$t\bar{t}$ ACERMC nominal	0.183±0.003	0.142±0.003
$t\bar{t}$ ACERMC FSR/ISR higher top mass	0.202±0.001	0.158±0.001

Table 4.15: Selection efficiencies for the ACERMC $t\bar{t}$ data samples corresponding to 200 pb^{-1} luminosity. FSR/ISR studies using most significant variations of the FSR/ISR parameters during the MC modeling.

re-weighting scheme already used at Tevatron which is based on MC truth information. The corresponding systematic uncertainties on $t\bar{t}$ cross section measurements coming from the choice of a particular PDF set is estimated to be less than 2 % for the "cut and count" method. These studies considered only signal data samples [2].

4.4.10 Estimation of the background fraction

The "cut and count" method relies on MC background (BG) estimation. The MC samples discussed in paragraph 4.1 were used to estimate the BG contribution after the selection presented above. Table 4.16 shows the initial number of events, event numbers after nominal selection, after nominal selection plus MET requirement and finally after nominal selection plus MET and the b-tagging requirements as discussed in section 4.4.2.

To estimate the systematic uncertainties coming from the jet reconstruction algorithms associated to the BG contribution the jets in the BG samples were reconstructed with Cone4, k_T4 and anti- k_T4 algorithms. The corresponding results are shown in tables 4.16, 4.17, 4.18. Table 4.19 summarizes all the BG contributions for the various jet reconstruction algorithms. The maximum difference between the selected events is 11 % after the nominal selection and

Data sample	Initial events	Nominal selection	+MET	+MET +btagging
All-hadronic $t\bar{t}$	30862	76	34	25
Single Top (Wt and t)	6124	537	489	345
W plus jets	405856	4241	3722	239
W plus $b\bar{b}$	1548	91	79	58
"Z plus jets"	115120	941	327	24
di-boson	3504	53	42	3
QCD 2J	19965635	458	206	82
QCD 3J	34178467	1938	502	156
QCD 4J	7980370	606	354	125
QCD 5J	2968499	1150	764	750

Table 4.16: The BG contribution before and after the selection corresponding to 200 pb^{-1} of luminosity. The second column shows the nominal selection, the third the nominal plus MET requirement, and the final column shows the nominal selection plus MET and b-tagging. The selection was done using jets reconstructed with the fixed Cone algorithm $\Delta R = 0.4$.

the nominal selection plus MET requirement, where as it decreases to 7 % after the b-tagging requirement. The estimation of the MC background contribution will be performed with the same jet reconstruction algorithm for the data analysis. There were no different MC generators available to investigate the jet reconstruction algorithm systematics in the same way as for the signal data sets. During the early phase of data taking we can assume the same order of systematic uncertainty on the BG fraction estimation due to the jet reconstruction algorithm as for the signal, shown to be $<1 \%$ in section 4.4.6.

The main background for the $t\bar{t}$ *lepton plus jets* channel are the "W plus jets" processes. No events pass the selection in the "W $\rightarrow l\nu_l$ plus 0, 1 and 2 partons" samples and therefore only data sets with more than 3 extra partons were considered for these studies.

Data sample	Initial events	Nominal selection	+MET	+MET +btagging
All-hadronic $t\bar{t}$	30862	75	34	25
Single Top (Wt and t)	6124	517	473	338
W plus jets	405856	4350	3824	247
W plus $b\bar{b}$	1548	87	76	56
"Z plus jets"	115120	907	319	24
di-boson	3504	51	41	3
QCD 2J	19965635	354	186	102
QCD 3J	34178467	1893	492	156
QCD 4J	7980370	604	356	145
QCD 5J	2968499	1340	950	568

Table 4.17: The BG contribution before and after the selection corresponding to 200 pb^{-1} of luminosity. The second column shows the nominal selection, the third the nominal plus MET requirement, and the final column shows the nominal selection plus MET and b-tagging. The selection was done using jets reconstructed with the k_T algorithm with $D = 0.4$.

Data sample	Initial events	Nominal selection	+MET	+MET +btagging
All-hadronic $t\bar{t}$	30862	73	33	25
Single Top (Wt and t)	6124	485	444	317
W plus jets	405856	3901	3424	230
W plus $b\bar{b}$	1548	82	72	53
"Z plus jets"	115120	832	292	22
di-boson	3504	45	36	3
QCD 2J	19965635	289	141	101
QCD 3J	34178467	1350	256	45
QCD 4J	7980370	605	335	124
QCD 5J	2968499	1336	948	751

Table 4.18: The BG contribution before and after the selection corresponding to 200 pb^{-1} of luminosity. The second column shows the nominal selection, the third the nominal plus MET requirement, and the final column shows the nominal selection plus MET and b-tagging. The selection was done using jets reconstructed with the anti- k_T algorithm with $D = 0.4$.

Data Sets	Nominal selection	+MET	+ b-tagging
Sum of all BG Cone4 jets	10091	6519	1807
Sum of all BG anti- k_T jets	10178	6751	1664
Sum of all BG k_T jets	8998	5981	1671

Table 4.19: The BG contributions for the different jet reconstruction algorithms corresponding to 200 pb^{-1} of luminosity.

To estimate the systematic uncertainties coming from the ID alignment precision, we had to reconstruct the events for the BG samples as it was done for the $t\bar{t}$ samples. In order to perform the tracking we require the basic detector information, i. e. the hits. Most of the background samples were processed via fast detector simulation (ATLFAST samples) and the corresponding detector information was not stored. The last production of "W plus jets" was generated with the full detector simulation which allowed us to study the misalignment affects on the BG estimation. The most significant changes in the b-tagging performance were observed for the "Curl" misalignment discussed in chapter 3.4.1. In table 4.20 the selection efficiencies corresponding to the "Perfect" and "Curl" ID geometries are shown for "W plus jets" samples. The effect of ID misalignment is more pronounced for the BG estimation. The number of "W plus jets" events surviving the nominal plus MET and b-tagging selection is 150 % more for "Curl" misalignment than for the Perfect ID geometry.

The estimation of BG contribution depends on the absolute JES. To study this dependence the BG contributions for four different scenarios were estimated, i. e. for the under- and over-estimated JES (5 and 10 %). From figure 4.5 the error on N_{BKG} depending on the JES can be estimated such that a 1 % variation of the JES

Geometry	Nominal+MET	+ b-tagging
Perfect	1627	113±11
"Curl"	1627	282±17

Table 4.20: The “ $W \rightarrow \mu\nu$ plus 3, 4, 5 jets” sample contributions after nominal plus MET and nominal plus MET, b-tagging requirements. Two geometries are considered, namely Perfect and "Curl" misalignment of the ID.

Data Sets	Nominal selection	+ b-tagging
Sum of all BG -10 % JES	10541 ±195	2107±67
Sum of all BG -5 % JES	12069 ±207	2332±70
Sum of all BG ±0 % JES	13092±211	2690± 71
Sum of all BG +5 % JES	15775±233	3270±76
Sum of all BG +10 % JES	16513 ±236	3369±77

Table 4.21: The BG contribution dependence on an absolute JES measurement corresponding to 200 pb^{-1} luminosity, for 5 %, 10 % under- and over-estimated absolute JES. The errors on the BG estimation correspond to the available generated data sample sizes.

corresponds to (2.29 ± 0.10) % variation of the background. In figure 4.6 the same distribution after nominal plus b-tagging selection is plotted leading to almost the same dependence (2.25 ± 0.17) % of the background estimation on JES variation, but with a larger error due to the smaller event rates after the b-tagging requirement. In table 4.22 the BG contribution variation corresponding to 5-10 % JES variation is summarized.

JES	$\Delta N_{BKG}/N_{BKG}$
±10 % JES	±23 %
±5 % JES	±11.5 %

Table 4.22: The variation of the BG contribution estimation corresponding to the ±10 % and ±5 % JES estimated using the MC@NLO generated data samples corresponding to 200 pb^{-1} luminosity.

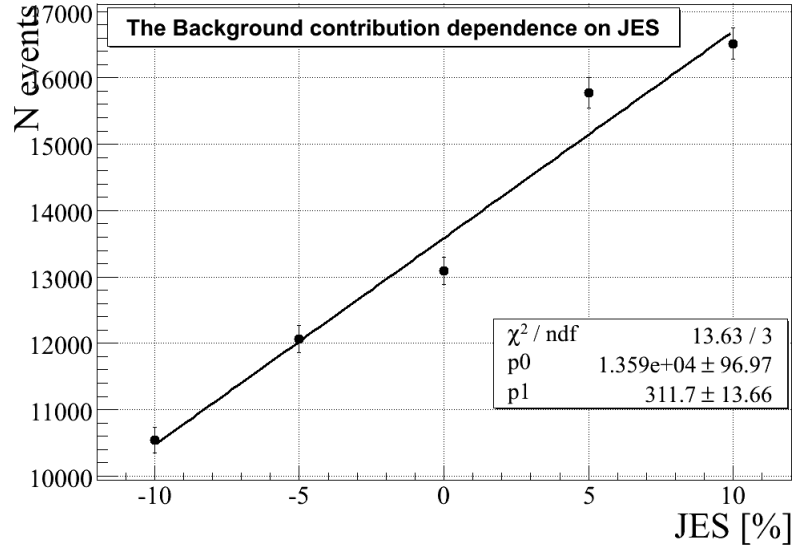


Figure 4.5: Background estimation dependence on JES.

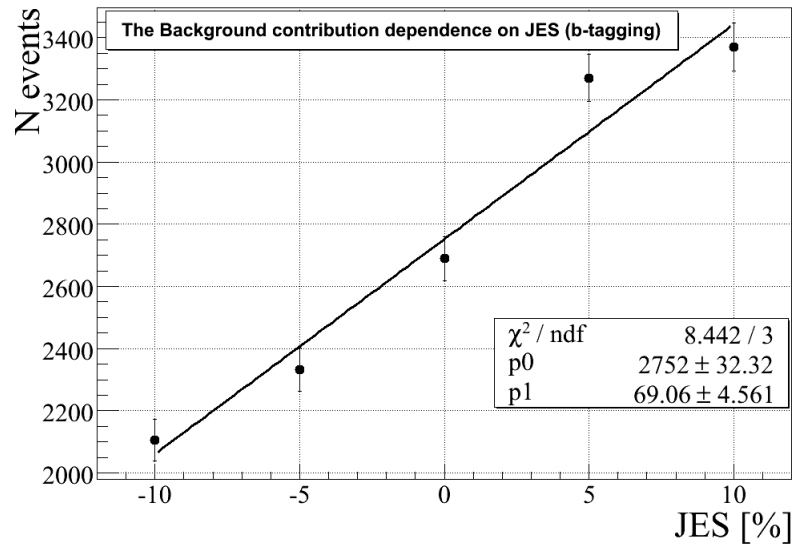


Figure 4.6: Background estimation dependence on JES after nominal selection plus b-tagging requirement.

4.5 Systematic Uncertainties on the cross section measurement

During the early LHC data taking period, only a rough measurement of the machine parameters will be available. The expected uncertainty on the luminosity during the first phase is estimated to be of the order of 20 %. This uncertainty will be reduced to 10 % after the first 200 pb⁻¹ have been collected [2].

One of the biggest contributions to the systematic uncertainty of the cross section measurement (max. 15 %) is coming from the modeling the signal within MC generator. An additional 10 % of the systematic error comes from FSR/ISR parametrization. These modeling errors can be reduced only after real data is used to check and tune the Monte Carlo generators.

The systematic error coming from the JES considering the BG fraction variation and the error on the signal selection efficiency determination will sum up for the cross section estimation. The two contributions are highly correlated and therefore the linear sum of the contributions was used to estimate the uncertainty on the cross section measurement coming from the JES variation:

$$\left| \frac{\Delta\sigma}{\Delta E} \right| = \left| \frac{\delta\sigma}{\delta N_B} \right| \delta N_{bkg} + \left| \frac{\delta\sigma}{\delta \epsilon_{sig}} \right| \delta \epsilon_{sig}. \quad (4.3)$$

The resulting systematic uncertainty on the cross section measurement for a 1 % JES variation is 5.8 % for the nominal selection. And for nominal selection plus b-tagging it goes down to 3 %.

One of the most important backgrounds is the W boson production in association with jets, where the W-boson decays leptonically. The uncertainty on the normalization of this process could be as large as 50 % because of the uncertainties in determining correctly

the number of the associated jets [94]. It can be reduced using data driven methods during running of the experiment. To estimate the systematic error coming from the BG modeling variations of the "W plus jet" contribution by 50 % and 20 % were considered. For other BG modeling (top quark BG not included) a 10 % variation was examined and the corresponding errors of the cross section were evaluated for the nominal plus MET requirement and nominal plus MET and b-tagging requirements shown in table 4.23.

The systematic uncertainties due to the jet reconstruction algorithm for signal and BG contributions were estimated to be less than 1 %. The systematic uncertainty due to the ID misalignment were estimated for the signal and the BG. The largest contribution was found to be 12 % in the case of the "Curl" misalignment.

In table 4.23 we summarize all the errors considered in this analysis for the $t\bar{t}$ cross section measurement with early data taking.

4.6 Conclusion

The simple and robust "cut and count" method was considered for the $t\bar{t}$ production cross section estimation with early data taking corresponding to 200 pb^{-1} of luminosity. It was shown that the statistics will be sufficient to observe top quark production via the strong interaction. The corresponding error on the cross section estimation, not including the uncertainty on the luminosity, and assuming 5 % JES and 20 % uncertainties on "W plus jet" production modeling, can be written in the following way: $\frac{\Delta\sigma}{\sigma} = \pm 3.2\%(\text{stat}) \pm 27.4\%(\text{syst})$.

The contributing errors were added in quadrature. The cross sec-

Source	Nominal	+ b-tagging
Statistical	± 2.8 %	± 3.2 %
lepton ID efficiency	± 1 %	± 1 %
5 % JES sig. + BG	± 29 %	± 15 %
Signal MC	± 15 %	± 15 %
Jet rec. algorithm sig. plus BG	< 1 %	< 1 %
ID alignment sig.	± 0 %	± 5 %
ID alignment "W plus jets"	± 0 %	± 12 %
ISR/FSR	9-10 %	10-11 %
PDFs	1.6-1.9 %	1.6-1.9 %
"W plus jet" modeling 20(50) %	11(28) %	1(3) %
other BG modeling 10 %	3.2 %	2.1 %
Sum of all systematic uncertainties	36.1 %	27.4 %

Table 4.23: Systematic uncertainties on the cross section measurement with "cut and count" method for the nominal and nominal plus b-tagging selection for 200 pb^{-1} of data at $\sqrt{s} = 10 \text{ TeV}$.

tion measurement with b-tagging gives less systematic error on the BG estimation, but due to the detector condition uncertainties it has additional systematic errors related to the alignment and calibration of the detector. This additional systematic error will decrease after a short period of data acquisition.

Chapter 5

Conclusions

The LHC is planned to start in late Autumn 2009. In the scope of this thesis we studied the performance of the software alignment of the ID. The local χ^2 alignment procedure was investigated using Monte Carlo datasets simulated with a misalignment of the detector. New constraints were implemented to improve the performance and robustness of the track based alignment procedure. The interaction vertex was added as an additional measurement to the track fit and an external beam constraint was applied afterwards. Improved tracking and vertex reconstruction was observed in the misaligned detector environment after the alignment procedure with these additional constraints. Nevertheless, we could not recover the misalignment completely. The χ^2 minimization of the residuals is less sensitive to global systematic distortions and only various track topologies can constrain systematic misalignments of the detector. To improve the final alignment various additional constraints on track reconstruction are planned; including calorimetry measurements, TRT momentum measurements, and decay particle invariant mass constraints.

We also investigated the b-tagging performance at an early stage of the detector operation. We found that the b-tagging performance can be affected by the ID misalignment and the effect is greatest when the innermost Pixel layer is misaligned in both random and systematic ID misalignment scenarios. The b-tagging performance dependence on the jet reconstruction algorithm was studied. The anti- k_T and k_T algorithms provided better performance than the fixed cone algorithm. This can be explained by noting differences in the number of the reconstructed jets and some of their properties, as the transverse energy of the jets. It was shown that the b-tagging performance does not depend on the jet calibration scenario. The robustness of the b-tagging performance with different calibrations was studied. The performance was stable for a given jet reconstruction algorithm when the calibration of the b-tagging was derived for another jet reconstruction algorithm. The p_T weighted cone association implemented for jets reconstructed with k_T algorithms showed similar performance compared to the fixed cone association. The b-tagging performance studies utilized $t\bar{t}$ data sets enriched with heavy flavour jets. It would be desirable to cross check the systematics associated to the analysis using the data sets with more partons in the final state and with more light jet contamination.

Finally the $t\bar{t}$ cross section measurement with early data corresponding to 200 pb^{-1} of ATLAS data was examined. We have seen that the statistics is sufficient to re-discover top quark pair production via the strong interaction. The largest contribution to the systematic error on the early cross section estimation in ATLAS is coming from the Monte Carlo modeling: 15 % for the signal modeling with different MC, 10 % for FSR/ISR modeling and upto 30 % for the BG modeling. The systematic error can be reduced as soon

as MC are tuned using real data. We found that the systematic uncertainty due to the jet reconstruction algorithm is less than 1 %. The misalignment of the ID contributes at most 17 % to the systematic uncertainties on the cross section measurement in case of a systematic misalignment of ID (Curl) before alignment procedure.

Assuming 5 % JES and 20 % uncertainties on W plus jet production modeling, and not including the uncertainty on the luminosity measurement the following uncertainty on the $t\bar{t}$ cross-section for the nominal selection with MET requirement is found:

$$\frac{\Delta\sigma}{\sigma} = 2.8 \%(stat.) + 36.1 \%(syst.) \quad (5.1)$$

For the nominal selection with MET and b-tagging requirements:

$$\frac{\Delta\sigma}{\sigma} = 3.2 \%(stat.) + 27.4 \%(syst.) \quad (5.2)$$

We applied a simple and robust cut and count method. It yields an early $t\bar{t}$ cross-section measurement with a systematic error of less than 30 %. The systematic error can be improved using more sophisticated methods relying on MC modeling when real data is available and MC tuning is done. Most of the BG samples were generated with sufficient statistics corresponding to 200 pb⁻¹ luminosity, but QCD samples were generated with moderate statistics. The QCD BG contribution estimation in ATLAS can be improved when data driven methods of QCD estimation are utilized. The MC tuning with real data will also improve the systematic error on the modeling of the signal and “W plus jets” processes.

Finally the systematic error on the $t\bar{t}$ cross-section measurement with b-tagging in ATLAS will benefit most when the detector alignment and calibration is performed with sufficient precision.

Bibliography

- [1] D. H. Perkins, *Introduction to High Energy Physics*, Cambridge University Press, 2000, 4th ed.
- [2] G. The ATLAS Collaboration, Aad et al., *The ATLAS Experiment at the CERN Large Hadron Collider*, JINST **S08003** (2008).
- [3] (The CMS Collab.), *CMS Physics Technical Design Report*, CERN/LHCC 2006-001 (2006).
- [4] F. Abe et al. (The CDF Collab.), Phys. Rev. Lett. **74** (1995) 2626.
- [5] S. Abachi et al. (The DØ Collab.), Phys. Rev. Lett. **74** (1995) 2632.
- [6] J. R. Incandela et al., *Status and Prospects of Top-Quark Physics*, (2009), 0904.2499.
- [7] M. E. Peskin and D. Schroeder, *Introduction to Quantum Field Theory*, Addison-Wesley, Reading, Mass., 1995.
- [8] R. Douglas, Large Hadron Collider Phenomenology, 2004.
- [9] S. Glashow, *Partial Symmetries of Weak Interaction*, Nuclear Physics **22:579** (1961).

-
- [10] S. Weinberg, *A Model of Leptons*, Physics Review Letters **19:1264-1266** (1967).
- [11] A. Salam, *Elementary Particle Theory*, 1967.
- [12] G. Arnison et al. (The UA1 Collab.), Phys. Lett. **122B** (1983) 103.
- [13] M. Banner et al. (The UA2 Collab.), Phys. Lett. **122B** (1983) 476.
- [14] G. Arnison et al. (The UA1 Collab.), Phys. Lett. **126B** (1983) 398.
- [15] P. Bagnaia et al. (The UA2 Collab.), Phys. Lett. **129B** (1983) 130.
- [16] P. Higgs, Phys. Rev. Lett. **13** (1964) 508.
- [17] P. Higgs, Phys. Rev. **145** (1966) 1156.
- [18] (ALEPH, DELPHI, L3 and OPAL collaborations, The LEP working group for Higgs Boson Searches Collab.), *Search for the Standard Model Higgs Boson at LEP*, (2003), CERN-EP/2003-011.
- [19] (CDF collaboration and DZero collaboration Collab.), *Combined CDF and DZero Upper Limits on Standard Model Higgs-Boson Production with up to 4.2 fb⁻¹ of Data*, (2009), 0903.4001.
- [20] H. Fritzsch, M. Gell-Mann, and H. H. Leutwyler, Phys. Lett. **47B** (1973) 365.
- [21] D. J. Gross and F. Wilczek, Phys. Rev. **D8** (1973) 3633.

-
- [22] C. Amsler et al., *Particle Data Group*, Physics Letters **1** (2008) B667.
- [23] M. Kobayashi and K. Maskawa, Prog. Theor. Phys. **49** (1973) 652.
- [24] J. H. Christenson et al., Phys. Rev. Lett. **13** (1964) 138.
- [25] R. K. Ellis, W. J. Stirling, and B. R. Webber, *QCD and collider physics*, Camb. Monogr. Part. Phys. Nucl. Phys. Cosmol. **8** (1996) 12.
- [26] J. N. Bahcall, P. I. Krastev, and A. Y. Smirnov, Phys. Rev. **D60** (1999) 093001.
- [27] R. Davis et al., Phys. Rev. Lett. **20** (1968) 1205.
- [28] R. K. Ellis, W. J. Stirling, and B. R. Webber, *QCD and collider physics*, Camb. Monogr. Part. Phys. Nucl. Phys. Cosmol. **8** (1996) 12.
- [29] S. Bethke, *The 2009 World Average of $\alpha_s(M_Z)$* , (2009), 0908.1135.
- [30] R. P. Feynman, Phys. Rev. **74** (1948) 1430.
- [31] R. P. Feynman, Phys. Rev. **76** (1949) 749.
- [32] R. P. Feynman, Phys. Rev. **76** (1949) 769.
- [33] R. P. Feynman, Phys. Rev. **80** (1950) 440.
- [34] J. C. Collins and D. E. Soper, Ann. Rev. Nucl. Part. Sci. **37** (1987) 383.
- [35] A. D. Martin et al., Phys. Lett. **B604** (2004) 61.

-
- [36] S. Chekanov et al. (ZEUS Collab.), *High- Q^2 neutral current cross sections in $e+p$ deep inelastic scattering at $s^{1/2} = 318\text{-GeV}$* , Phys. Rev. **D70** (2004) 052001, hep-ex/0401003.
- [37] C. Adloff et al. (H1 Collab.), *Measurement and QCD analysis of neutral and charged current cross sections at HERA*, Eur. Phys. J. **C30** (2003) 1, hep-ex/0304003.
- [38] J. Pumplin et al., *New generation of parton distributions with uncertainties from global QCD analysis*, JHEP **07** (2002) 012, hep-ph/0201195.
- [39] T. Sjostrand et al., *High-energy physics event generation with PYTHIA 6.1*, Comput. Phys. Commun. **135** (2001) 238, hep-ph/0010017.
- [40] G. Corcella et al., *HERWIG 6.5: an event generator for Hadron Emission Reactions With Interfering Gluons (including supersymmetric processes)*, JHEP **01** (2001) 010, hep-ph/0011363.
- [41] M. Perl et al., Phys. Rev. Lett. **35** (1975) 1489.
- [42] M. A. Shifman, A. I. Vainshtein, and Z. V. I., Nucl. Phys. **B147** (1979) 385, 448, 519.
- [43] R. K. Ellis, W. J. Stirling, and B. R. Webber, *QCD and collider physics*, Camb. Monogr. Part. Phys. Nucl. Phys. Cosmol. **8** (1996) 281.
- [44] S. Herb et al., Phys. Rev. Lett. **39** (1977) 252.
- [45] (LEP Collaborations and ALEPH Collaboration and DELPHI Collaboration and L3 Collaboration and LEP Electroweak Working Group and SLD Electroweak Group and SLD Heavy

- Flavour Group and OPAL Collaboration Collab.), *A Combination of preliminary electroweak measurements and constraints on the standard model*, (2004), hep-ex/0412015.
- [46] V. M. Abazov et al. (The D0 Collab.), *Observation of Single Top Quark Production*, (2009), 0903.0850.
- [47] T. Aaltonen et al. (The CDF Collab.), *First Observation of Electroweak Single Top Quark Production*, (2009), 0903.0885.
- [48] A. Quadt, *Top quark physics at hadron colliders*, Eur. Phys. J. **C48** (2006) 835.
- [49] R. Bonciani et al., *NLL resummation of the heavy-quark hadroproduction cross-section*, Nucl. Phys. **B529** (1998) 424, hep-ph/9801375.
- [50] E. Brubaker et al. (Tevatron Electroweak Working Group Collab.), *Combination of CDF and D0 Results on the Mass of the Top Quark*, (2006), hep-ex/0608032.
- [51] J. Ellis, *Large Hadron Collider Phenomenology*, 2004.
- [52] J. Wess and B. Sumino, Phys. Lett. **49B** (1974) 52.
- [53] A. Ahmad, *Effect of CSC misalignment on $Z \rightarrow \mu\mu$ mass reconstruction*, <http://indico.cern.ch/materialDisplay.py?contribId=0&sessionId=6&materialId=slides&confId=a0626>, Presentation given at ATLAS ID week from Monday 25 September 2006 to Friday 29 September 2006, Geneva.
- [54] A. Salzburger, *ATLAS coordinate frames*, <https://twiki.cern.ch/twiki/bin/view/Atlas/CoordinateFrames>.

-
- [55] T. Golling, *Alignment of the Silicon Tracking Detector using Survey Constraints*, ATLAS Note (2006), ATL-INDET-PUB-2006-001.
- [56] K. Sedlak, *Frequency Scanning Interferometry System for SCT Alignment*, <https://twiki.cern.ch/twiki/bin/view/Atlas/FSIforSCT>, ATLAS Twiki.
- [57] T. Cornelissen et al., *Updates of the ATLAS Tracking Event Data Model*, 2007.
- [58] T. Goettfert, *Iterative local χ^2 alignment algorithm for the ATLAS Pixel detector*, 2006, Diploma thesis.
- [59] R. Haertel, *Iterative local χ^2 alignment approach for the ATLAS SCT detector*, 2005, Diploma thesis.
- [60] S. González-Sevilla, *Multimuon samples*, <http://ific.uv.es/~segonzal/multimuons/multimu.html>.
- [61] *The Computing System Commissioning data challenge*, <https://twiki.cern.ch/twiki/bin/view/Atlas/CSCAlignmentChallenge>, ATLAS Twiki.
- [62] *Silicon misalignments for the Computing System Commissioning data challenge*, <https://twiki.cern.ch/twiki/bin/view/Atlas/SiliconMisaCSC>, ATLAS Twiki.
- [63] *ID Hit Error Scaling*, <https://twiki.cern.ch/twiki/bin/view/Atlas/InDetErrorScalingRel12>, ATLAS Twiki.
- [64] P. Brückman, A. Hicheur, and S. J. Haywood, *Global χ^2 approach to the Alignment of the ATLAS Silicon Tracking Detectors*, (2005), ATL-INDET-PUB-2005-002.

- [65] *location of the VertexOnTrack package in the CVS repository*, <http://atlas-sw.cern.ch/cgi-bin/viewcvs-atlas.cgi/offline/Tracking/TrkEvent/TrkVertexOnTrack/>, ATLAS CVS repository.
- [66] *location of the primary vertex finder tool in the CVS repository*, <http://atlas-sw.cern.ch/cgi-bin/viewcvs-atlas.cgi/offline/InnerDetector/InDetRecTools/InDetPriVxFinderTool/>, ATLAS CVS repository.
- [67] Ellis, S. D. and Soper, D. E., *Successive combination jet algorithm for hadron collisions*, Phys. Rev. **D 48** ((1993)) 3160.
- [68] Cacciari, M. and Salam G. P. and Soyez, G., *The anti-kt jet clustering algorithm*, JHEP **063** ((2008)) 0804.
- [69] G. Aad et al. (The ATLAS Collab.), *Performance of the ATLAS b-tagging Algorithms*, (2009), 0901.0512.
- [70] G. Aad et al. (The ATLAS Collab.), *Expected Performance of the ATLAS Experiment - Detector, Trigger and Physics*, (2009), ATL-PHYS-PUB-2009-018.
- [71] S. Frixione and B. Webber, JHEP **06** (2002) 029.
- [72] R. Bonciani et al., Nucl. Phys. **B529** (1998) 424.
- [73] S. Agostinelli et al., Nucl. Instrum. Meth. **A 506** (2003) 250.
- [74] A. Rimoldi et al., *The simulation of the ATLAS experiment: Present status and outlook*, ATLAS Notes (2004), ATLASOFT(004).
- [75] J. Pumplin et al., JHEP **02** (2006) 032.

- [76] D. N. Brown et al., *Local Alignment of the BABAR Silicon Vertex Tracking Detector*, 0809.3823.
- [77] *The Impact of Inner Detector Misalignments on Selected Physics Processes*, ATLAS Notes (2009), ATL-PHYS-PUB-2009-080.
- [78] R. Haertel, Studies on an initial top quark mass measurement at ATLAS in the lepton+jets $t\bar{t}$ decay channel and alignment of the Pixel and SCT subdetectors, 2009, PhD thesis.
- [79] *Information about Inner Detector alignment with cosmic data taken in the ATLAS cavern*, https://twiki.cern.ch/twiki/bin/view/Atlas/InDetAlignCosmicCavern#InDetAlignCosmicNote2008_note_fo/, ATLAS Twiki.
- [80] J. Alison, B. Cooper, and T. Goettfert, *Production of Residual Systematically Misaligned Geometries for the ATLAS Inner Detector*, CERN, Geneva, 2009.
- [81] P. Nason, S. Dawson, and R. K. Ellis, Nucl. Phys. **B303** (1988) 607.
- [82] W. Beenakker et al., Phys. Rev. **D40** (1989) 54.
- [83] M. Cacciari et al., *Updated predictions for the total production cross sections of top and of heavier quark pairs at the Tevatron and at the LHC*, JHEP **09** (2008) 127, 0804.2800.
- [84] P. M. Nadolsky et al., Phys. Rev. **D 78** (2008) 013004.
- [85] S. Moch and P. Uwer, *Theoretical status and prospects for top-quark pair production at hadron colliders*, Phys. Rev. **D78** (2008) 034003, 0804.1476.

-
- [86] S. Frixione et al., *JHEP* **0308** (2003) 007.
- [87] J. Butterworth et al., *Zeit. fuer Phys.* **C72** (1996) 637.
- [88] B. P. Kersevan and E. Richter-Was, *The Monte Carlo event generator AcerMC version 2.0 with 24 interfaces to PYTHIA 6.2 and HERWIG 6.5*, hep-ph/0405247 (2004).
- [89] J. Alwall et al., *Eur. Phys. J.* **C53** (2008) 473.
- [90] *Understanding Monte Carlo Generators for Top Physics*, ATLAS Notes (2009), ATL-COM-PHYS-2009-xxx.
- [91] M. L. Mangano et al., *Alpgen, a generator for hard multiparton processes in hadronic collisions*, *JHEP* **07** (2003) 001.
- [92] A. D. Martin et al., *Uncertainties of predictions from parton distributions. 1: Experimental errors*, *Eur. Phys. J.* **C28** (2003) 455, hep-ph/0211080.
- [93] J. Pumplin et al., *Uncertainties of predictions from parton distribution functions. 2. The Hessian method*, *Phys. Rev.* **D65** (2001) 014013, hep-ph/0101032.
- [94] M. L. Mangano, *Understanding the Standard Model, as a bridge to the discovery of new phenomena at the LHC*, *Int. J. Mod. Phys.* **A23** (2008) 3833, 0802.0026.